MITIGATION OF COLLAPSE RISK IN VULNERABLE CONCRETE BUILDINGS

BY

Lisa Matchulat

Submitted to the graduate degree program in Civil Engineering
and to the Graduate Faculty of the University of Kansas
in partial fulfillment of the requirements for the degree of
Master of Science.

_____
Dr. Adolfo Matamoros, Chairman

Committee Members: _____
Dr. JoAnn Browning

_____
Dr. Stanley Rolfe

Date Defended: _____

The Thesis Committee for Lisa Matchulat certifies
that this is the approved Version of the following thesis:

MITIGATION OF COLLAPSE RISK IN VULNERABLE CONCRETE BUILDINGS

_____
Dr. Adolfo Matamoros, Chairman

Committee Members: _____
Dr. JoAnn Browning

_____
Dr. Stanley Rolfe

Date Approved: _____

ABSTRACT

The goal of this study is to investigate the collapse risk of reinforced concrete building columns constructed prior to the mid-1970's, subjected to cyclic lateral loading. These columns have reinforcement details deemed inadequate by modern seismic design standards, and as such are vulnerable to collapse. Testing of two full-scale, shear-critical column specimens was carried out at the NEES-MAST facility at the University of Minnesota. The test specimens had nominally identical material and reinforcement properties. The primary test variable was the applied axial load, which was held constant at 500 kips and 340 kips for the first and second specimens, respectively. The specimens were subjected to increasing lateral displacement cycles until axial load carrying capacity was lost. The thesis discusses the observed lateral and axial load resisting behavior, and analyzes the measured responses of the columns up to and beyond the lateral drift at which they were able to sustain axial load. Test results indicate that column behavior was significantly influenced by the magnitude of the applied axial load, and that the ratio of axial load to gross axial capacity of the longitudinal reinforcement is a key parameter in identifying columns in which axial failure occurs simultaneously with shear failure.

ACKNOWLEDGEMENTS

Primary financial support for this project was provided by the National Science Foundation under award number 0618804 through the Pacific Earthquake Engineering Research Center. This support is gratefully acknowledged.

Many individuals deserve thanks for their help and advice throughout the course of this project. I would like to thank Dr. Adolfo Matamoros for taking me on as a research assistant, and for his guidance and support throughout the project.

The staff at the NEES-MAST facility at the University of Minnesota were an invaluable asset to the project's success. I would especially like to thank Paul Bergson, Angela Kingsley, Carol Shield, Jonathan Messier, and Drew Daugherty for their wealth of knowledge, their ingenuity, and their patience throughout the testing process. In addition, the involvement of Kurt Henkhaus and Julio Ramirez from Purdue University during the planning, instrumentation, and testing phases of the project is greatly appreciated.

I would like to thank everyone at the University of Kansas who helped contribute to the successful fabrication of the test specimens. Travis Malone provided a great deal of instruction and advice in the early construction phases of the project. Our student hourly workers, Emily Reimer and Vinur Kaul, were extremely valuable and I owe much of the success of our strain gages to their diligent work. Jim Weaver also provided much-needed support and expertise throughout the construction process. The addition of Charlie Woods to the project team midway through the testing phase was more helpful than I can express. Thank you for your

teamwork, your dedication, and your friendship. I would like to extend a special thanks to Mike Briggs for his help and guidance throughout the writing process. I can't express how much your editing assistance and emotional support has meant to me. In addition, the help from all the other graduate students with formwork construction, specimen casting, and general morale boosting on a daily basis is gratefully acknowledged and has made this experience one I will remember fondly.

Finally, I would like to thank my family for their continued love and support throughout my graduate studies. You have always been there to provide advice, understanding, and emotional support whenever I've needed it. I truly could not have finished this without your love and encouragement and for that I am eternally grateful to each of you.

TABLE OF CONTENTS

LIST OF FIGURES

LIST OF TABLES

CHAPTER 1: BACKGROUND AND PREVIOUS RESEARCH

1.1 Introduction

Poor seismic performance of some reinforced concrete building columns designed and constructed prior to the mid-1970s has raised concern and interest in identifying those most vulnerable to collapse. Post-earthquake damage investigation and research have led to modifications in design codes in an effort to achieve ductile column behavior. This is essential to limit the loss of life in buildings during earthquakes. The most noteworthy update in seismic design procedures followed the 1971 San Fernando Earthquake. While a great deal of effort has been dedicated to improving design provisions, much remains unknown regarding the loss of axial capacity of existing reinforced concrete columns, constructed prior to the mid-1970s. The majority of these columns have widely spaced transverse reinforcement, which provides little lateral restraint to the longitudinal reinforcement and negligible confinement to the core concrete during seismic loading. As such, many of these columns would be deemed inadequate by modern design standards. Thus, engineers and government entities are in dire need of identifying those that have the greatest risk of collapse and pose the biggest threat in terms of potential loss of life. Characterizing not only the shear capacity, but the ability of these columns to sustain axial load carrying capacity beyond the point of shear failure, is of paramount interest. This Chapter discusses the previous experimental and analytical research into the failure behavior and drift capacity of reinforced concrete columns with

similar detailing to those constructed prior to the mid-1970s, when subjected to cyclic lateral loading.

1.2 Background

1.2.1 General Load-Deflection Response

Much of the current research into the axial capacity of concrete columns under cyclic lateral loading is based on tests of full-length columns loaded in double curvature to examine the deformation response. The typical deformed shape of the columns is as shown in Figure 1.1. This double curvature shape is similar to that of many columns in reinforced concrete moment-resisting frames subjected to lateral loading. A representative load-deflection response curve for these columns is shown in Figure 1.2.

In typical test loading protocols, a column is subjected to cyclic lateral loading, with peak deflection increasing in successive load cycles, as depicted in Figure 1.2. After the column reaches its maximum lateral load carrying capacity, the combination of crack propagation in the column along with increased column displacement, leads to the deterioration of both lateral and axial load carrying capacity and eventually results in axial failure (Elwood 2004). Comparison of columns with differing heights is accommodated by dividing the lateral displacement by the height of the column as shown in Figure 1.1, yielding a drift ratio δ. The drift ratios at axial failure for various test specimens can then be examined to determine the effects different parameters have on column strength and ductility.

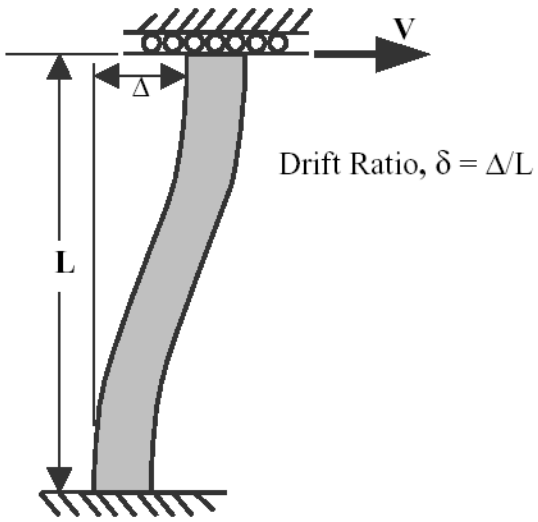

Figure 1.1: Deformation of columns loaded in double curvature

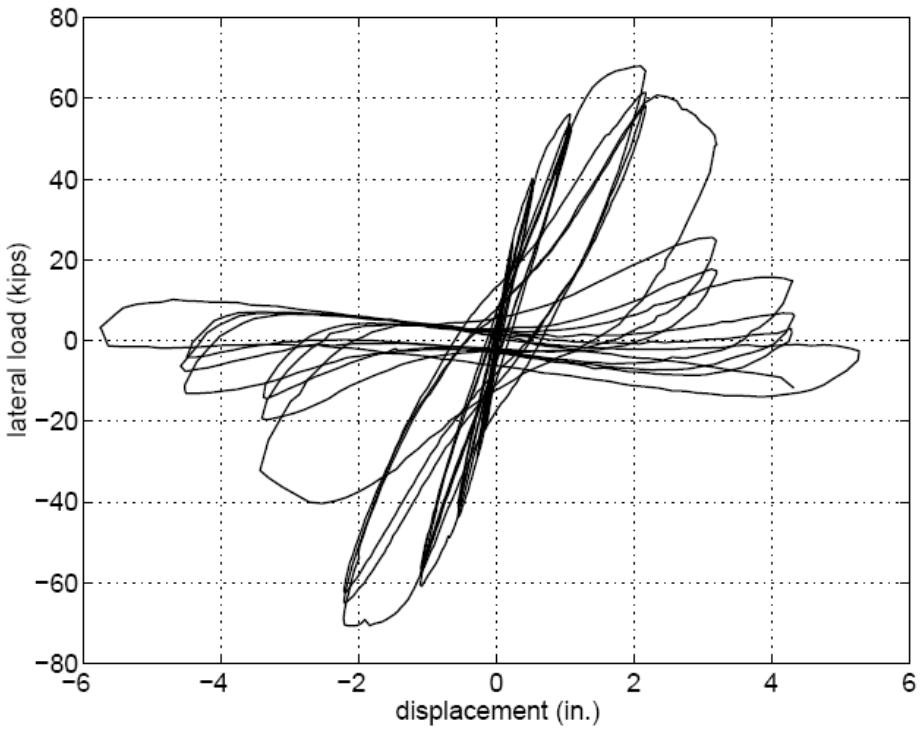

Figure 1.2: Typical load-deflection response (Specimen 2CLD12 – Sezen 2000)

In terms of lateral load, the mode of axial failure for columns can be classified as one of three types: shear failure, flexural failure, or flexural-shear failure (Matamoros 2006). As Figure 1.3 shows, the mode of axial failure for a given specimen can be determined by the relationship between the envelope for shear strength and the envelope for flexural strength, which are both functions of column geometry, material properties, reinforcement, and loading. More important than the strength envelopes, however, is the difference between the nominal shear capacity V_n and the plastic shear demand V_p. The plastic shear demand refers to the shear force at which flexural yielding occurs in the longitudinal reinforcement, forming plastic hinges in the maximum moment regions of the specimen (which form at the top and bottom of columns subjected to double curvature). The difference between the two strength envelopes plays a key role in predicting the failure mode of a given specimen.

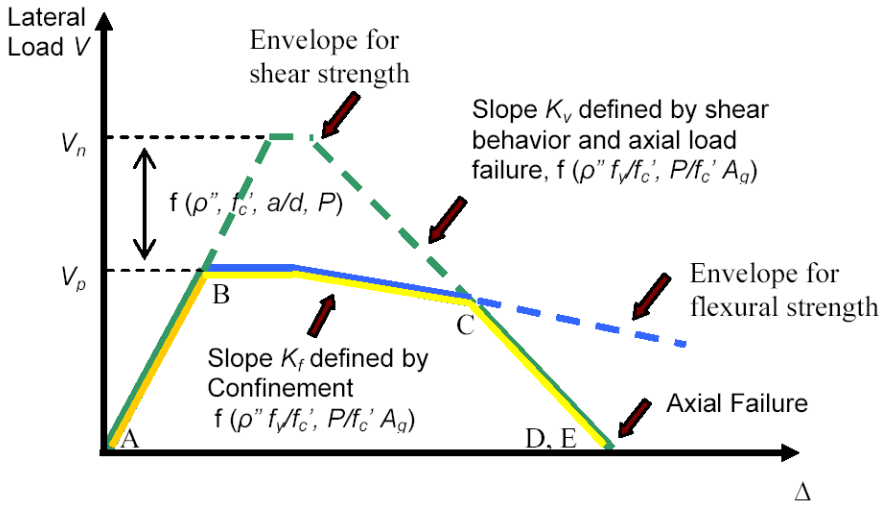

Figure 1.3: Failure envelopes for reinforced concrete columns

Curves depicting the shear-controlled failure mode are shown in Figure 1.4. For a column to undergo this type of failure, V_p must exceed V_n, resulting in a V_p / V_n ratio greater than 1.0 (Elwood 2007). These types of columns have minimal transverse reinforcement that often yields soon after the development of inclined cracks, rendering the reinforcement unable to contain the growth of these cracks. As a result, specimens that experience shear-controlled failure develop inclined cracks that grow very rapidly. Axial failure may occur soon after, or simultaneously with the loss of lateral load carrying capacity, prior to yielding of the longitudinal reinforcement (Matamoros 2006). This failure mode is typical of columns with a large percentage of longitudinal reinforcement or insufficient transverse reinforcement. Due to the minimal warning prior to a shear-controlled axial failure and the small deformation capacity these types of columns possess, it is the least desirable of the three modes of failure from a structural performance standpoint.

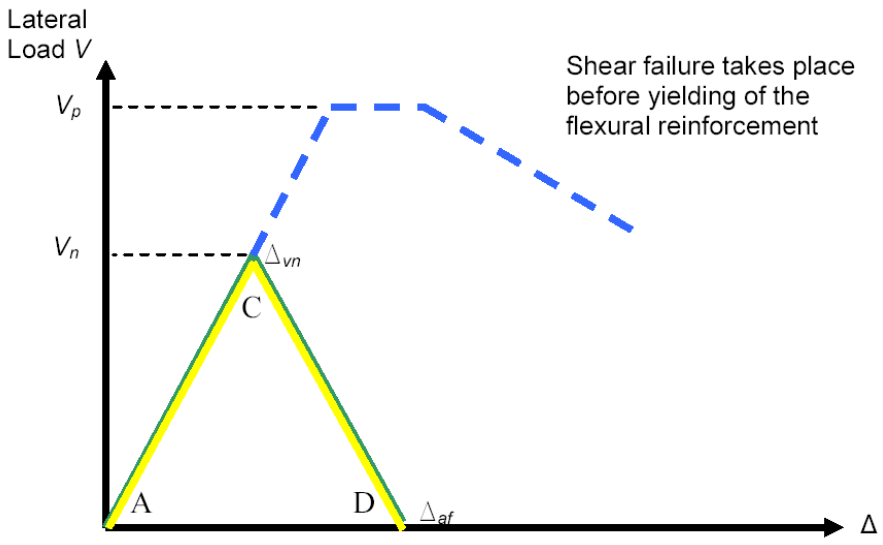

Figure 1.4: Shear-controlled axial failure envelopes

Curves depicting the flexure-controlled failure mode are illustrated in Figure 1.5. This type of failure occurs when the applied lateral load causes yielding in the longitudinal reinforcing steel. Yielding can be identified by an increase in the lateral displacement of the specimen while the lateral load remains nearly constant. Yielding is also evidenced by the gradual formation of horizontal flexural cracks on the column faces subjected to flexural tension. These cracks grow at a much slower rate than those formed during shear failure, and as a result, they provide greater warning prior to axial failure. Furthermore, yielding of the longitudinal reinforcement allows for much greater lateral deformation, and the column is generally able to maintain axial capacity up to a much higher lateral displacement than a column controlled by shear failure. At displacements beyond yielding of the longitudinal reinforcement, spalling of the concrete cover often occurs in the maximum moment regions of the specimen, leading to a reduction in axial capacity. During flexure-controlled failure, V_n significantly exceeds V_p, and yields a V_p / V_n ratio less than 0.6 (Elwood 2007). As a result, the envelope for flexural strength controls and the column ultimately fails due to P-Δ effects before the two envelopes intersect.

The third and final failure mode, flexural-shear failure, is a combination of the previous two. As shown in Figure 1.6, this failure mode results when V_n is slightly higher than V_p, yielding a V_p / V_n ratio between 0.6 and 1.0 (Elwood 2007). During this type of failure, the specimen is taken through three major phases of damage: flexural yielding, shear failure, and ultimately axial failure. The first of these phases,

flexural yielding, occurs just as it does in the flexure-controlled failure mode, with the formation of horizontal flexural cracks and large increases in lateral displacement. As lateral loading continues, the horizontal flexural cracks continue to grow deeper into the specimen along an incline, developing into shear cracks. This results in a significant reduction in lateral load carrying capacity. Researchers often assume that shear failure has taken place when the lateral load decreases to 80% of its maximum value (Elwood 2005). As the column is subjected to further lateral displacement cycles, the loss in lateral load carrying capacity translates into a loss of axial load carrying capacity. Ultimate axial failure occurs when the lateral load resistance of the specimen deteriorates to approximately zero.

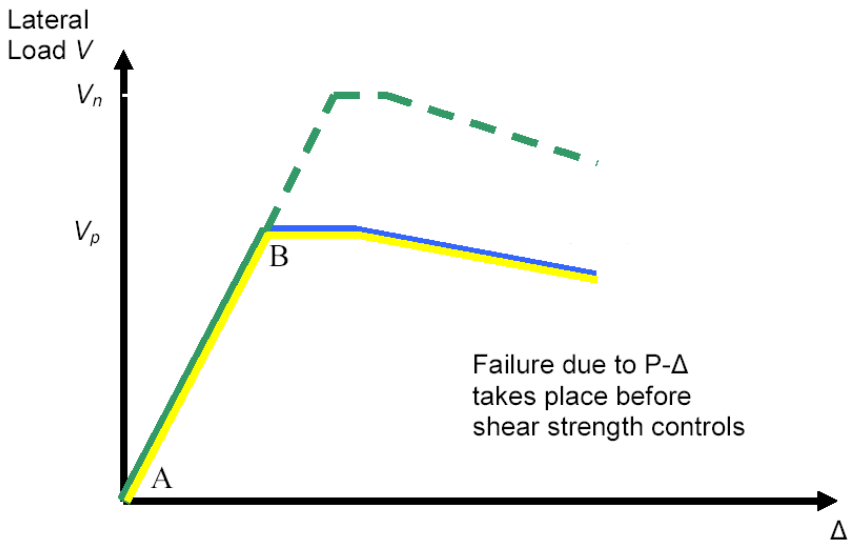

Figure 1.5: Flexure-controlled axial failure envelopes

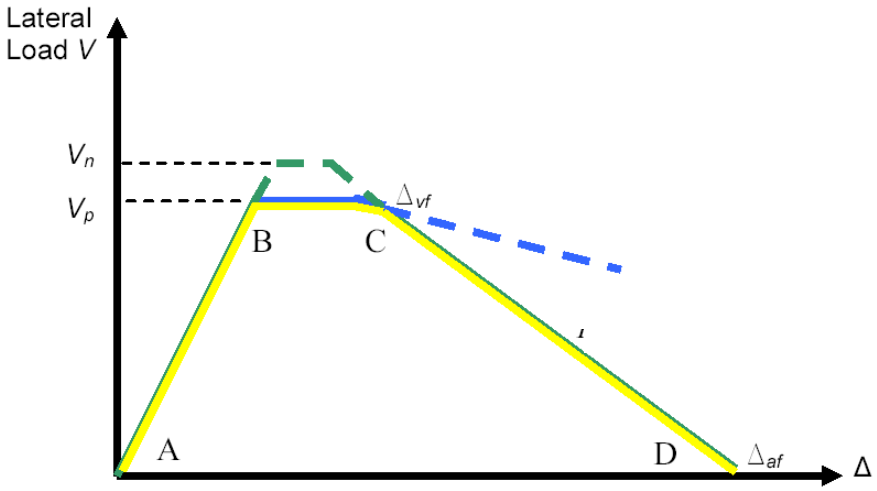

Figure 1.6: Flexural-shear axial failure envelopes

1.2.2 Effect of Axial Load on Drift Capacity

The magnitude of the axial load applied to a column undergoing cyclic lateral loading has a significant effect on both the drift capacity and the behavior of the column near axial failure. In general, large axial loads result in low drift ratios at failure, while low axial loads correspond to larger drift ratios. This relationship can clearly be seen in Figure 1.7 from tests performed by Nakamura and Yoshimura (2002). The first and second graphs show the lateral load-deflection responses of two specimens with axial load ratios of 0.18 and 0.27 $A_g f_c'$, respectively. The lower axial load specimen was able to maintain axial capacity up to a drift ratio of 20.6%, while the specimen with the high axial load experienced axial failure at a drift ratio of only 3.0%. Studies by Saatcioglu (1989), Lynn (2001), and Sezen (2000) also report similar findings.

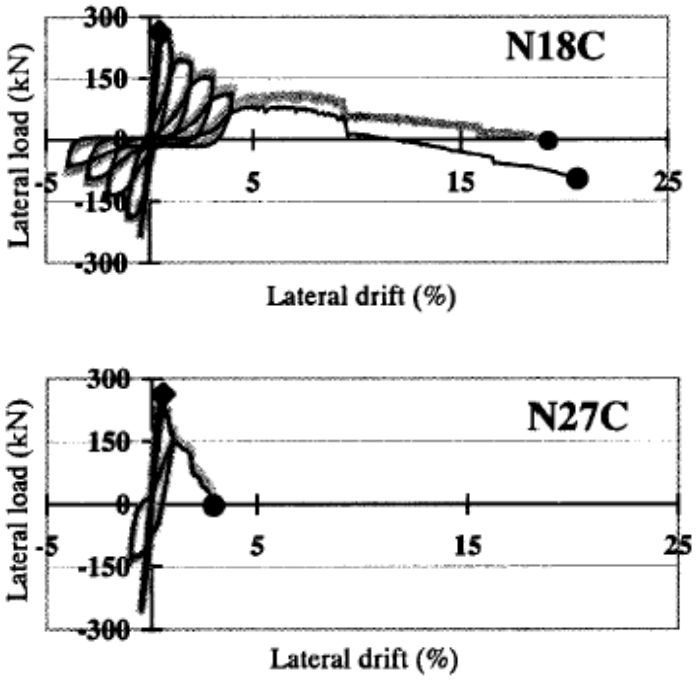

Figure 1.7: Lateral load-deflection responses for different axial load levels

(a) 0.18 $A_g f_c'$, (b) 0.27 $A_g f_c'$

Nakamura and Yoshimura (2002) also note that large axial loads correspond to greater axial shortening in columns for a given lateral displacement. This relationship is displayed in Figure 1.8 for the same two specimens discussed previously. While the specimen with the lower axial load exhibited greater ultimate axial deformation, the specimen with the higher axial load exhibited a larger axial deformation at any given lateral displacement. For instance, the axial strain in the low axial load specimen at a 3% lateral drift ratio was 0.2%, while the axial strain for the high axial load specimen at this point was 0.8%.

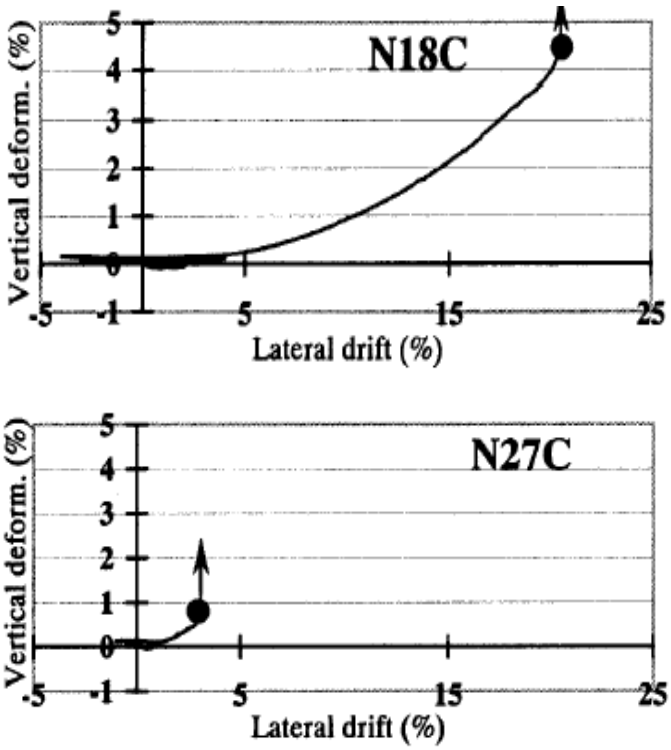

Figure 1.8: Vertical deformation-lateral drift responses for different axial load levels (a) 0.18 $A_g f_c'$, (b) 0.27 $A_g f_c'$

The level of axial load has also been shown to exert significant influence on the ultimate failure mode. In general, a large axial load increases the likelihood of a brittle shear failure, while lower axial loads tend to result in flexural or flexural-shear failures. In research performed by Sezen (2000), two columns with identical properties, designed to have the same lateral force at yield, were tested under different axial load levels. The column subjected to the lighter load reached flexural yielding prior to failing in shear. Continued lateral cycling resulted in additional loss of lateral load carrying capacity. At the end of testing, the lateral resistance had

degraded to effectively zero, but the column was still able to maintain axial load carrying capacity. The column with the higher load, however, experienced sudden, simultaneous shear and axial failure following the formation of a large inclined crack. The drastic difference in failure modes emphasizes the importance of differentiating between columns based on axial load level when performing seismic evaluations.

1.3 Previous Research

1.3.1 Lynn (2001) and Sezen (2000) Experimental Research

Concern regarding the vulnerability of reinforced concrete columns designed and constructed prior to the mid-1970s, and the lack of experimental data related to their behavior has lead to studies performed at the University of California, Berkeley by Lynn (2001) and Sezen (2000). In both studies, full-scale reinforced concrete building columns were tested under cyclic lateral loading until the columns could no longer sustain axial load carrying capacity. The loading, boundary conditions, and detailing of the test specimens were very similar to those tested in the present study. Table 1.1 lists specimen details, material properties, and axial failure data for tests performed by Lynn and Sezen; Figure 1.9 illustrates typical specimen configuration.

The displacement protocol for the specimens applied a series of lateral displacement cycles of increasing amplitudes, with three cycles at each displacement value. After axial failure was observed, the tests were concluded. The specimens of particular interest to the present study were those that experienced shear-controlled axial failure, as well as those that provided a comparison of column behavior on the

basis of axial load. Trends in the drift capacity and mode of axial failure observed were consistent with background information provided in Section 1.2. The results from the Lynn and Sezen tests indicate that the lateral drift ratio at which axial failure occurs is primarily dependent on the axial load applied to the column, and the spacing and amount of transverse reinforcement (Elwood 2003).

Table 1.1: Properties of column specimens (Lynn 2001 and Sezen 2000)

Specimen	b **(in.)**	ρ_{long}	A_{st} **(in^2)**	s **(in.)**	f'_c **(ksi)**	f_{yl} **(ksi)**	f_{yt} **(ksi)**	P **(kips)**	V_{test} **(kips)**	$\Delta_{failure}$ **(in.)**
Lynn (2001)										
3CLH18	18	0.030	0.22	18	3.71	48	58	113	61	2.4
2CLH18	18	0.020	0.22	18	4.80	48	58	113	54	3.6
3SLH18	18	0.030	0.22	18	3.71	48	58	113	60	3.6
2SLH18	18	0.020	0.22	18	4.80	48	58	113	52	4.2
2CMH18	18	0.020	0.22	18	3.73	48	58	340	71	1.2
3CMH18	18	0.030	0.22	18	4.01	48	58	340	76	2.4
3CMD12	18	0.030	0.38	12	4.01	48	58	340	80	2.4
3SMD12	18	0.030	0.38	12	3.73	48	58	340	85	2.4
Sezen (2000)										
2CLD12	18	0.025	0.38	12	3.06	64	68	150	73	5.8
2CHD12	18	0.025	0.38	12	3.06	64	68	600	78	2.2
2CVD12	18	0.025	0.38	12	3.03	64	68	Var.	70	3.4
2CLD12M	18	0.025	0.38	12	3.16	64	68	150	67	5.9

Notation: b = square column width; ρ_{long} = longitudinal reinforcement ratio; A_{st} = area of transverse reinforcement; s = hoop spacing; f'_c = concrete compressive strength; f_{yl} = longitudinal steel yield strength; f_{yt} = transverse steel yield strength; P = axial load; V_{test} = peak recorded shear; $\Delta_{failure}$ = displacement at axial failure

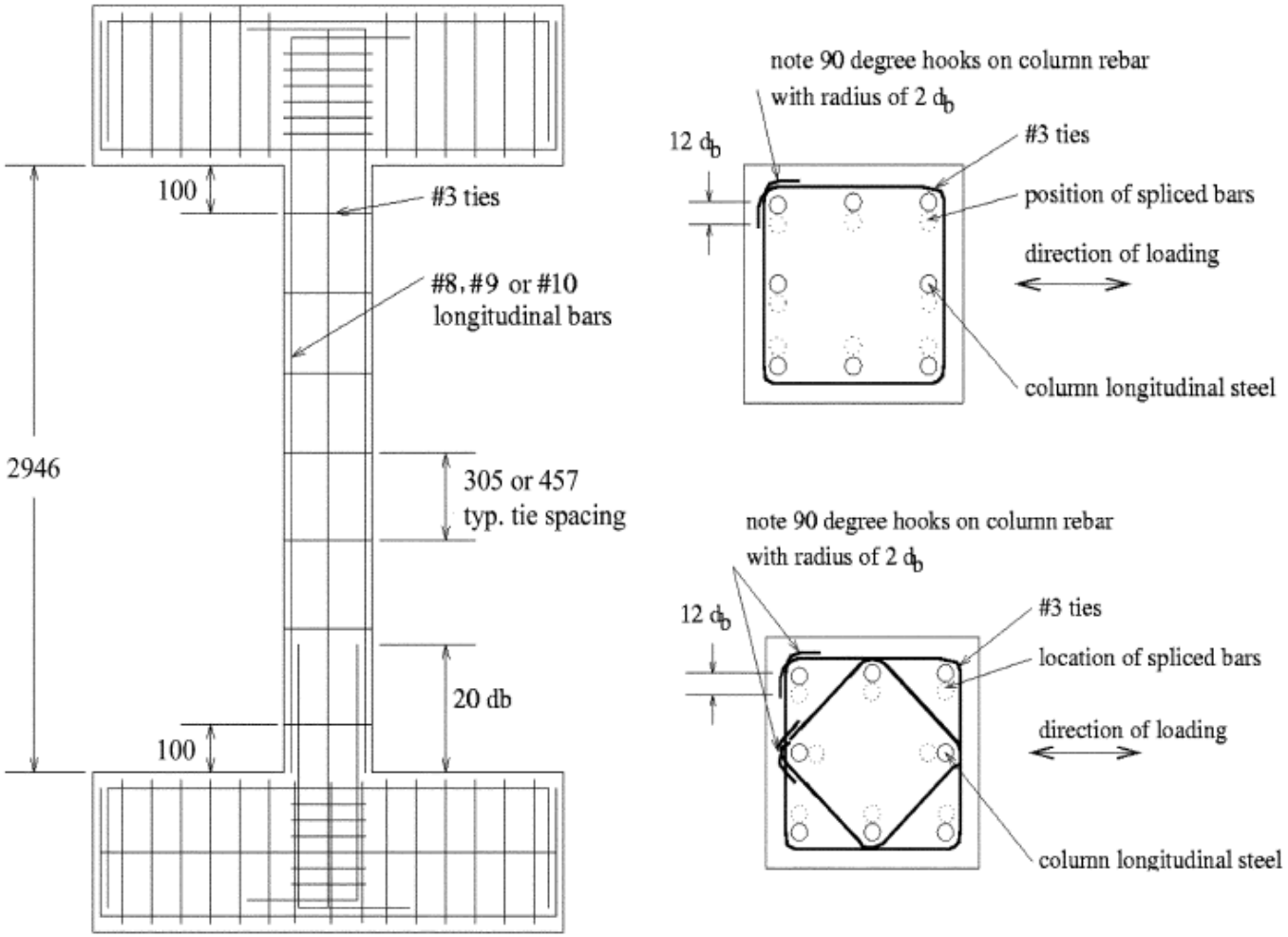

Figure 1.9: Typical column specimen configuration (Lynn 2001 and Sezen 2000)

1.3.2 Elwood-Moehle (2003) Axial Capacity Model

In order to calculate the axial capacity of a given column after shear failure has occurred, Elwood and Moehle (2003) proposed a model based on the shear friction developed along a critical inclined crack in the column. Figure 1.10 shows the free body diagram of the various forces involved in this analysis.

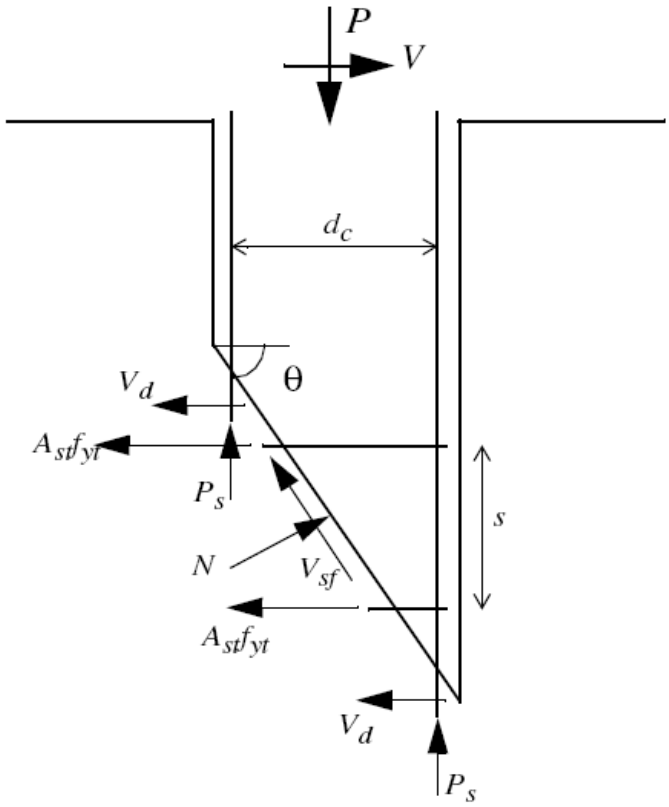

Figure 1.10: Free body diagram of column forces after shear failure

Based on this free body diagram, forces can be summed in the *x* and *y* directions as follows in Eq. (1.1) and (1.2).

$$\Sigma F_x \rightarrow N \sin\theta + V = V_{sf} \cos\theta + \frac{A_{st} f_{yt} d_c}{s} \tan\theta + n_{bars} V_d \quad (1.1)$$

$$\Sigma F_y \rightarrow P = N \cos\theta + V_{sf} \sin\theta + n_{bars} P_s \quad (1.2)$$

Where:

N = normal force on inclined shear-failure plane (kips)

θ = angle from horizontal of critical shear-failure plane (degrees)

V = shear force (kips)

V_{sf} = shear friction force along inclined shear-failure plane (kips)

A_{st} = area of transverse reinforcement (in^2)

f_{yt} = yield strength of transverse reinforcement (ksi)

d_c = depth of core (centerline to centerline of hoops, in.)

s = spacing of transverse reinforcement (in.)

n_{bars} = number of longitudinal reinforcing bars

V_d = shear resistance due to dowel action of longitudinal steel (kips)

P = axial load (kips)

P_s = axial load supported by longitudinal reinforcement (kips)

The final term in Eq. (1.1) is the shear resistance provided by dowel action in the longitudinal reinforcement, which has decreasing effectiveness as the spacing of the transverse reinforcement increases. In buildings most vulnerable to collapse, columns have a large hoop spacing and thus $n_{bars}V_d$ goes to zero, so this component is neglected in the final model. Also, the V term on the left side of this equation can be

ignored, as the shear force drops to effectively zero at the point of axial failure. As a result, Eq. (1.1) can be rewritten as follows in Eq. (1.3).

$$N \sin\theta = V_{sf} \cos\theta + \frac{A_{st} f_{yt} d_c}{s} \tan\theta \tag{1.3}$$

Equilibrium Eq. (1.2) and (1.3) can be combined into Eq. (1.4) to solve for the axial capacity of the column.

$$P = \frac{A_{st} f_{yt} d_c}{s} \tan\theta \left(\frac{1 + \mu \tan\theta}{\tan\theta - \mu} \right) + n_{bars} P_s \tag{1.4}$$

Elwood recommends using a value of 65° for the critical crack angle, based on empirical results from tests performed by Lynn (2001) and Sezen (2000). In addition, the effective shear friction coefficient μ is approximated using Eq. (1.5).

$$\mu = \tan\theta - \frac{100}{4}\delta \geq 0 \tag{1.5}$$

Where:

μ = effective shear friction coefficient

δ = lateral drift ratio at axial failure

Equation (1.6) incorporates Eq. (1.5) into the Eq. (1.4), creating the axial capacity model that predicts the lateral drift ratio at axial failure.

$$\delta = \frac{4}{100} \frac{1 + \tan^2 \theta}{\tan \theta + P\left(\frac{s}{A_{st} f_{yt} d_c \tan \theta} \right)} \tag{1.6}$$

Thus, the model suggests that lateral drift ratio δ at axial failure is inversely proportional to both the applied axial load P and the spacing of the transverse reinforcement s, and directly related to the amount of transverse reinforcement A_{st}. This behavior is consistent with the experimental results obtained by Lynn (2001) and Sezen (2000). Figure 1.11 shows a graphical representation of the relationship between axial load and drift ratio at axial failure predicted by the Elwood-Moehle failure model for Specimen 3CLH18, tested by Lynn (2001).

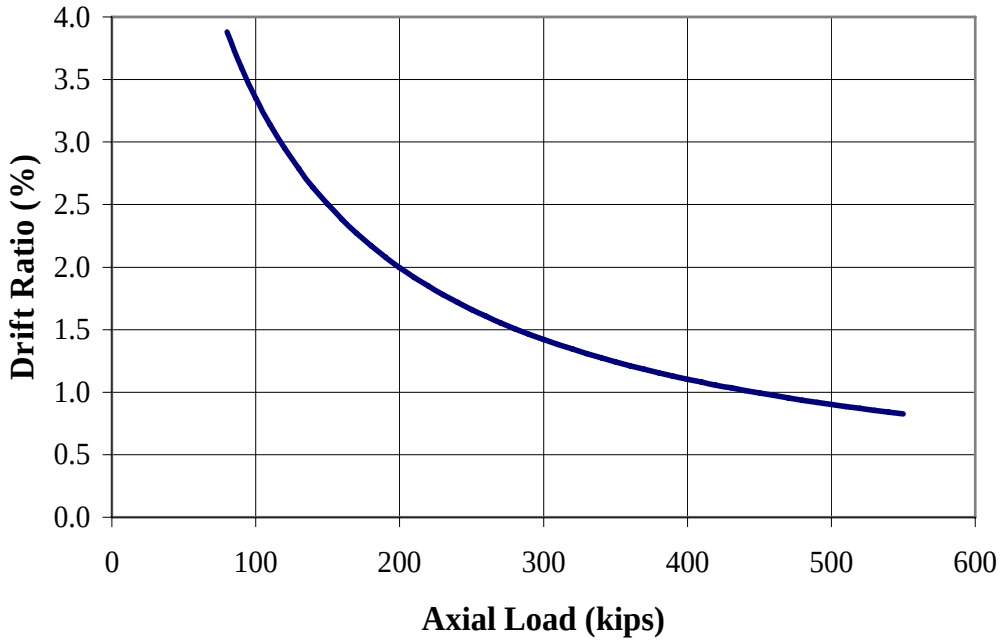

Figure 1.11: Elwood-Moehle model for drift ratio at axial failure

(Specimen 3CLH18 – Lynn 2001)

1.4 Objectives and Scope

The purpose of this study was to obtain additional information on the behavior of columns subjected to cyclic lateral loading that are vulnerable to shear and axial failure. The main objective of experimental investigation was to examine the effect of axial load level on the drift capacity and axial failure mode of the columns. The experimental program was comprised of two columns, with identical dimensions and detailing, subjected to two different levels of axial load. Testing was performed up to and beyond the point of initial axial failure. The information provided by this study is intended to be used to evaluate the ability of existing methods to calculate the drift capacity of reinforced concrete columns vulnerable to collapse, and to investigate their load resisting behavior near axial failure. The two experiments were designed so that the lateral load capacity of the columns would be controlled by shear, to focus on columns most vulnerable to axial failure during earthquakes.

CHAPTER 2: EXPERIMENTAL PROGRAM

2.1 Introduction

Two full-scale concrete columns were tested as part of a research program to study the collapse risk of reinforced concrete building columns designed and constructed prior to the mid-1970's. The columns were subjected to high levels of axial load and the lateral load capacity was limited by shear strength. The intent of the two tests was to provide information that would help identify columns in which simultaneous shear and axial failure take place. Both specimens were cast in the Structural Testing Laboratory at the University of Kansas and were tested at the NEES-MAST facility at the University of Minnesota (http://nees.umn.edu). The columns were loaded in double curvature, to simulate the boundary conditions and response of a typical moment-resisting frame in an actual reinforced concrete building. The primary test variable was the axial load level, while the quantity and distribution of reinforcement, column geometry, and target concrete compressive strength remained constant. The general specimen dimensions and test configuration were selected to be similar to specimens tested by Lynn (2001), to allow for comparison of results.

2.2 Specimen Description

The column element in both specimens had a clear height of 9-ft, 8-in. and an 18-in. by 18-in. square cross-section. At the top and bottom of each column, beam elements were cast to allow for connection to the reaction floor of the laboratory and

the crosshead of the multi-axial loading system. Each beam element was 7-ft long by 2-ft, 4-in. wide by 2-ft, 6-in. deep. To limit the contribution of beam deformations to the overall lateral deformation of the column, the beams were conservatively reinforced so that their flexural stiffness would be much greater than that of the column. In addition to limiting the deformation of the beams during testing, the use of a strong-beam, weak-column configuration ensured that damage would occur within the column section. Figures 2.1 through 2.10 show the column and beam dimensions and reinforcement details.

The longitudinal reinforcement consisted of eight No. 9 bars, which corresponds to a reinforcement ratio of 0.025. Longitudinal bars were placed uniformly around the perimeter of the cross-section, with 2½ in. of cover to the center of the bars. All bars were continuous and contained no lap splices. The column bars extended into the top and bottom beams, where a 90° bend was placed as shown in Figure 2.1. Transverse reinforcement consisted of No. 3 closed hoops. All column hoops had hooks with 90º bends and a $5d_b$ extension beyond the hook. Hoops were spaced at 18 in. center-to-center along the full height of the columns.

During testing, the specimens were fixed to an 8-ft, 6-in. long by 3-ft wide by 3-ft, 8-in. tall concrete base block to adjust for the height of the loading system. The procedure used to fix the specimens to the base block and the reaction floor is described in detail in Section 2.5. The block was cast with twelve 2½-in. diameter vertical holes and six 2-in. diameter vertical holes used to secure the block to the floor with threaded steel rods. Four additional 2-in. diameter horizontal holes were cast to

lift the block into place. All holes were through thickness shafts. Dimensions and reinforcement details of the base block are shown in Figures 2.11 and 2.12.

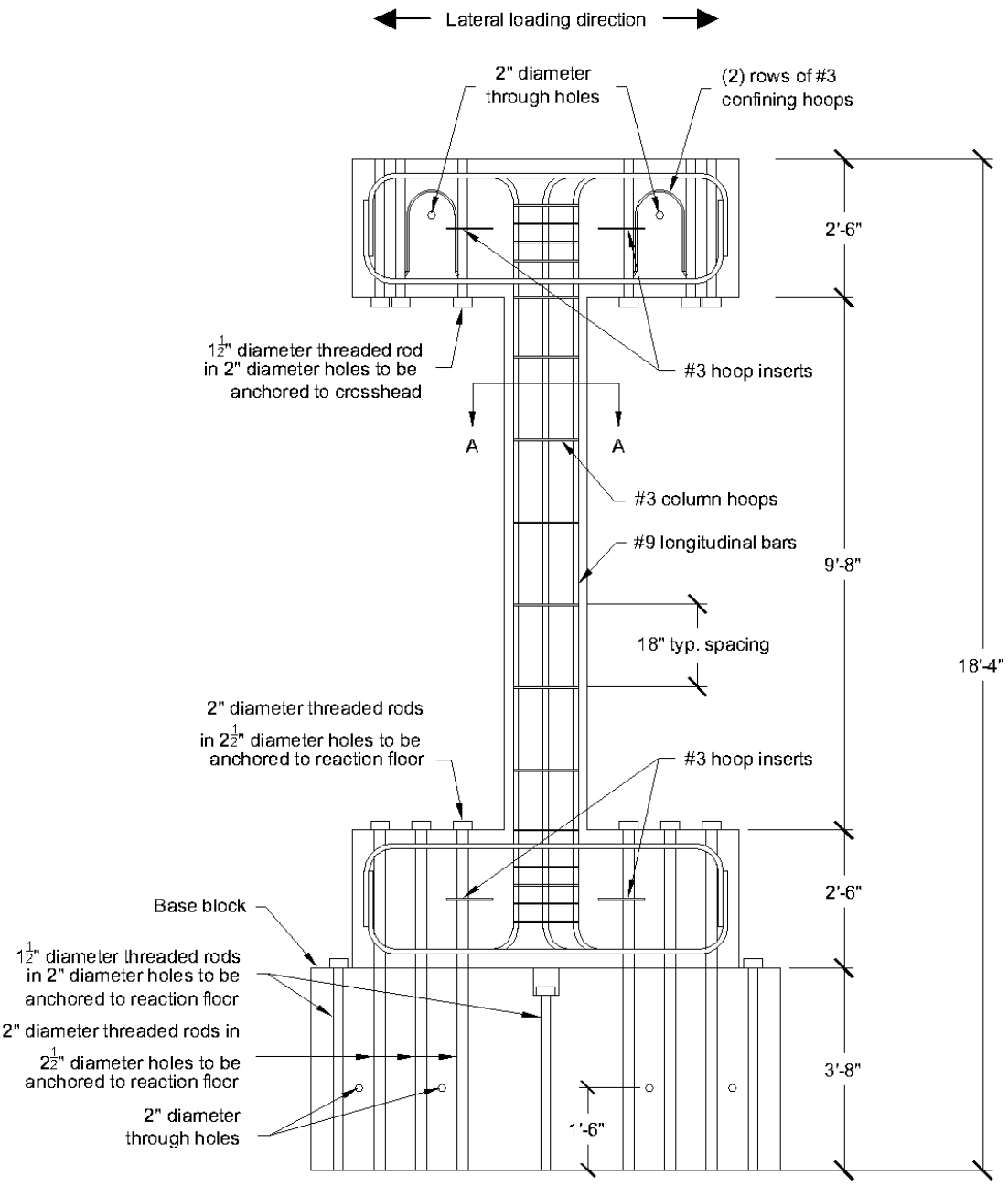

Figure 2.1: Specimen elevation

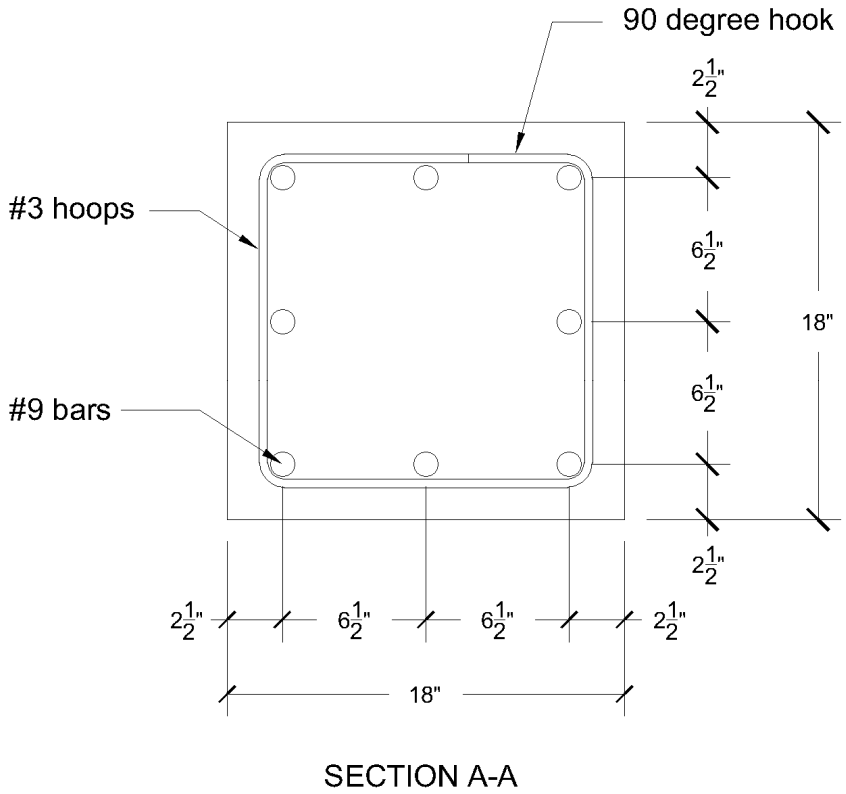

Figure 2.2: Column cross-section

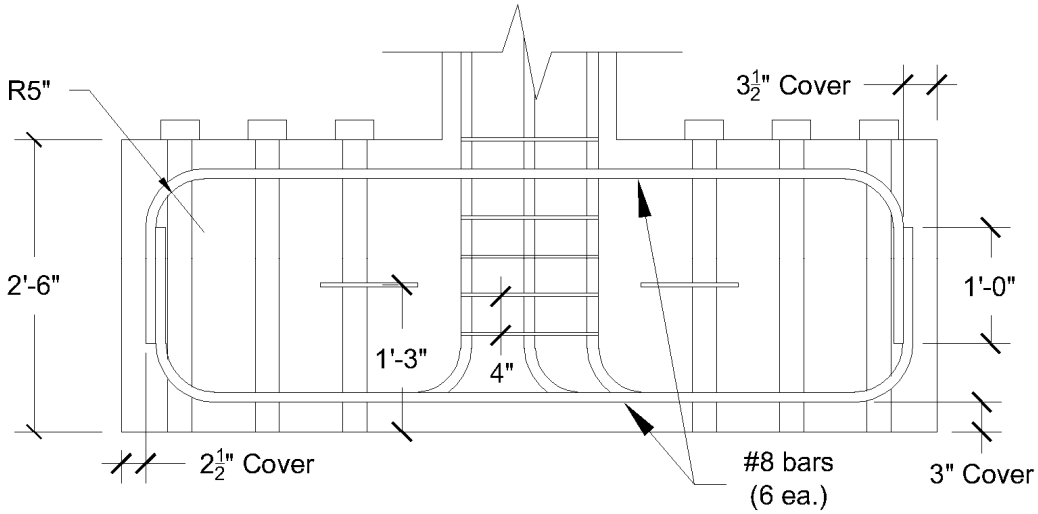

Figure 2.3: Bottom beam elevation

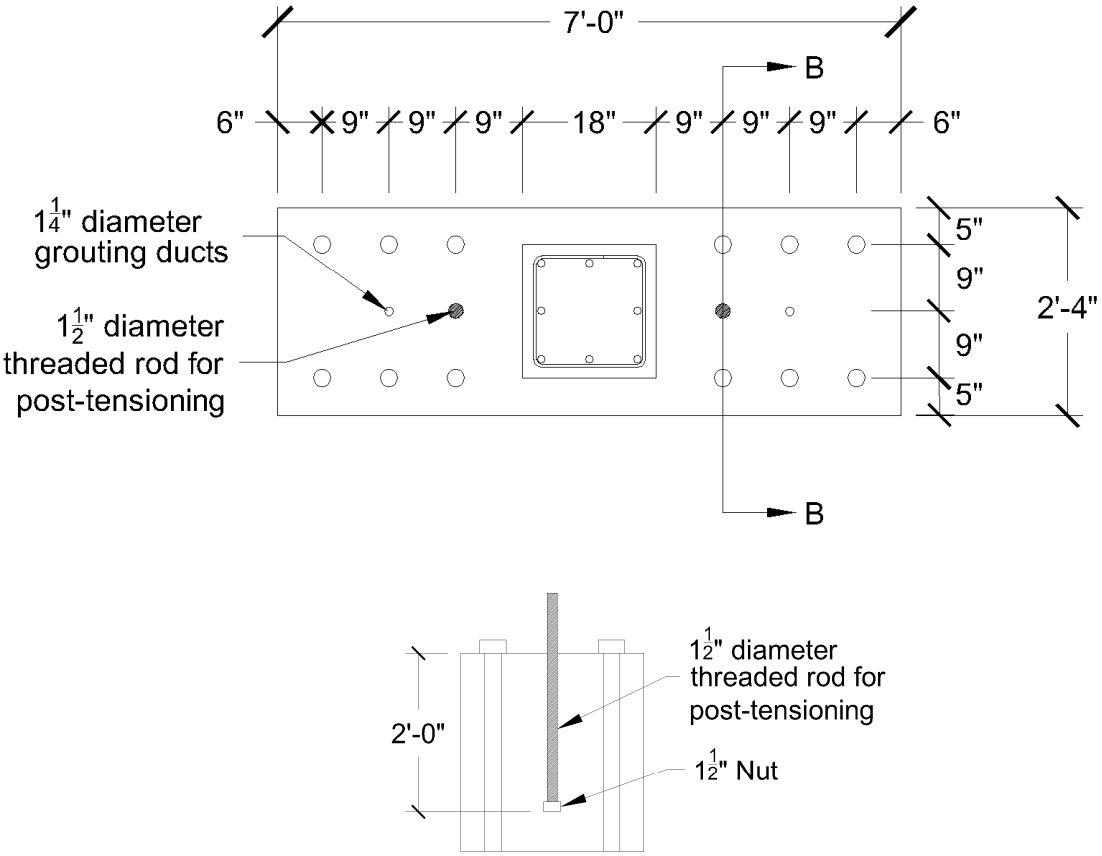

Figure 2.4: Bottom beam hole layout

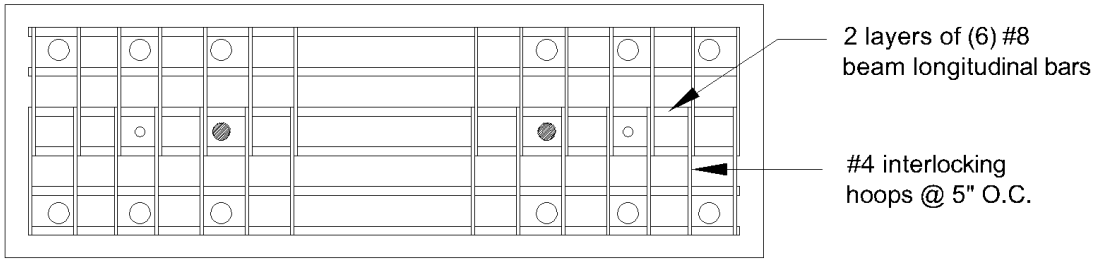

Figure 2.5: Bottom beam reinforcement layout

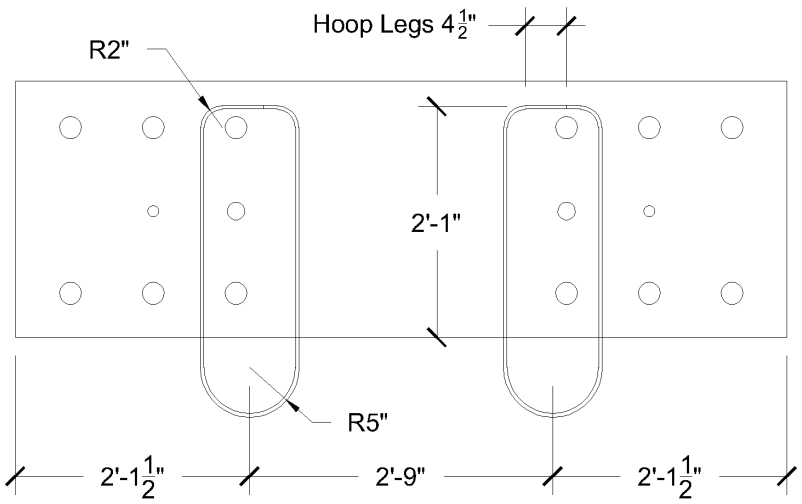

Figure 2.6: Bottom beam hoop insert layout

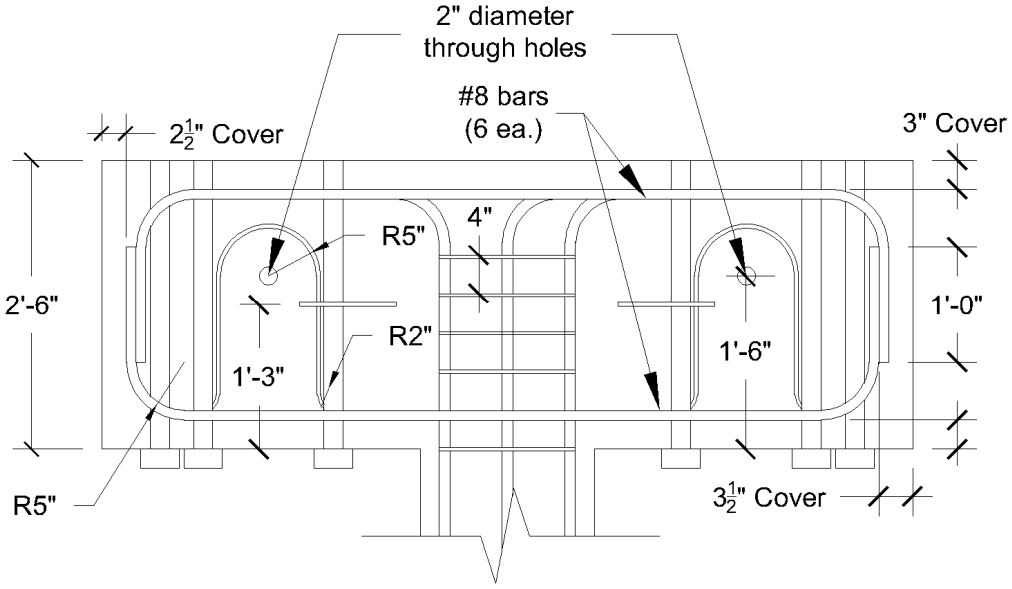

Figure 2.7: Top beam elevation

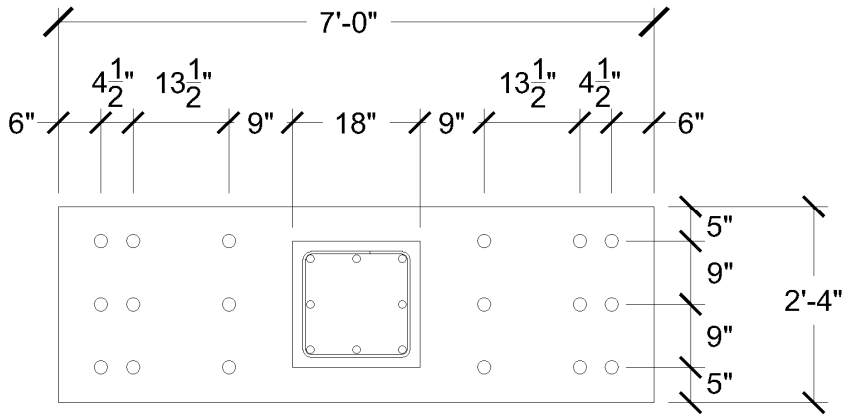

Figure 2.8: Top beam hole layout

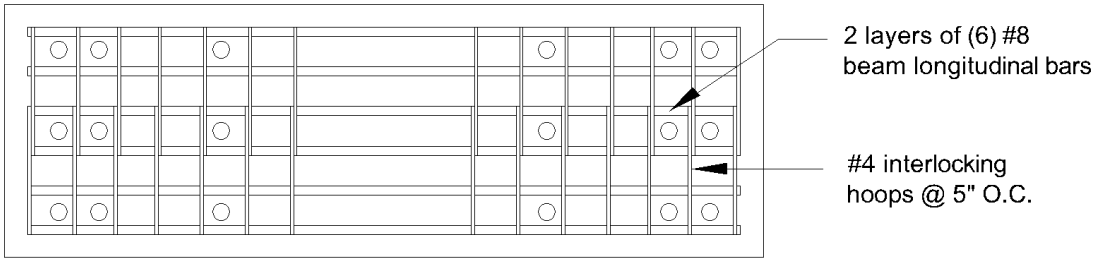

Figure 2.9: Top beam reinforcement layout

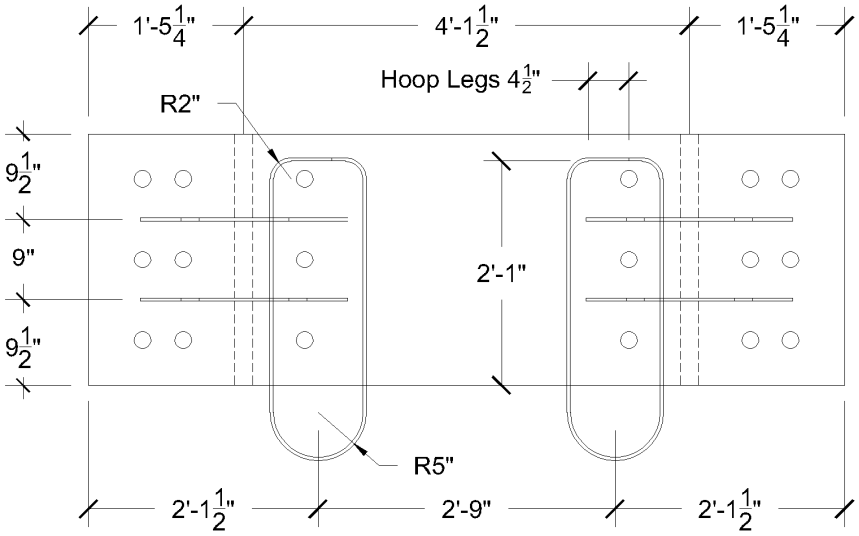

Figure 2.10: Top beam hoop insert layout

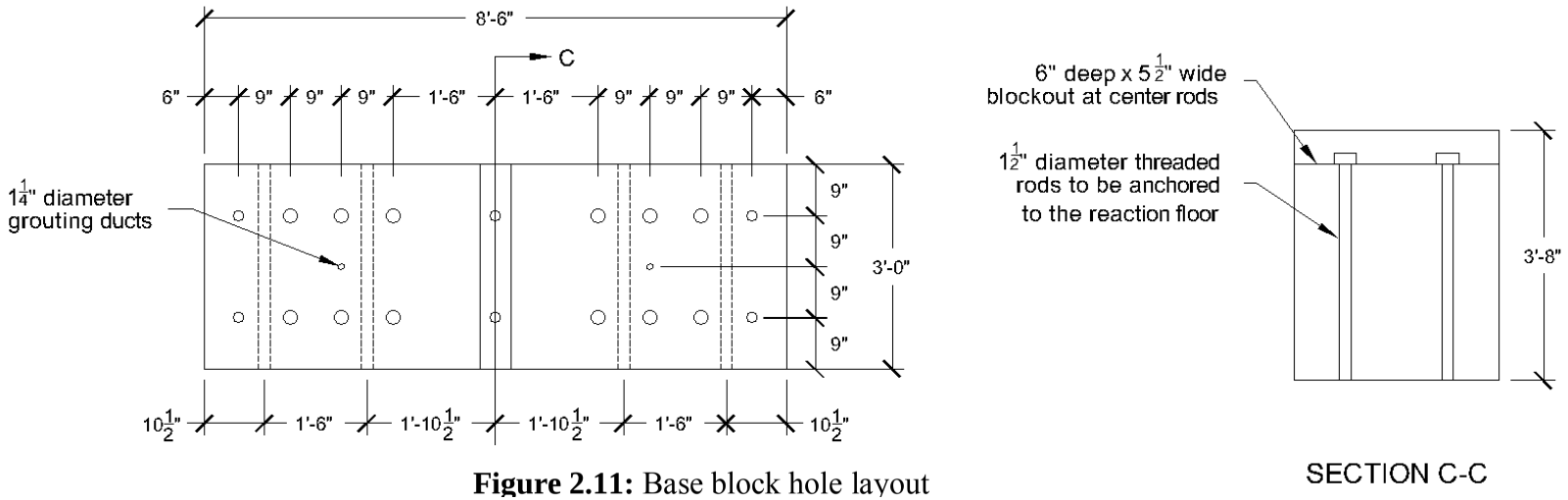

Figure 2.11: Base block hole layout

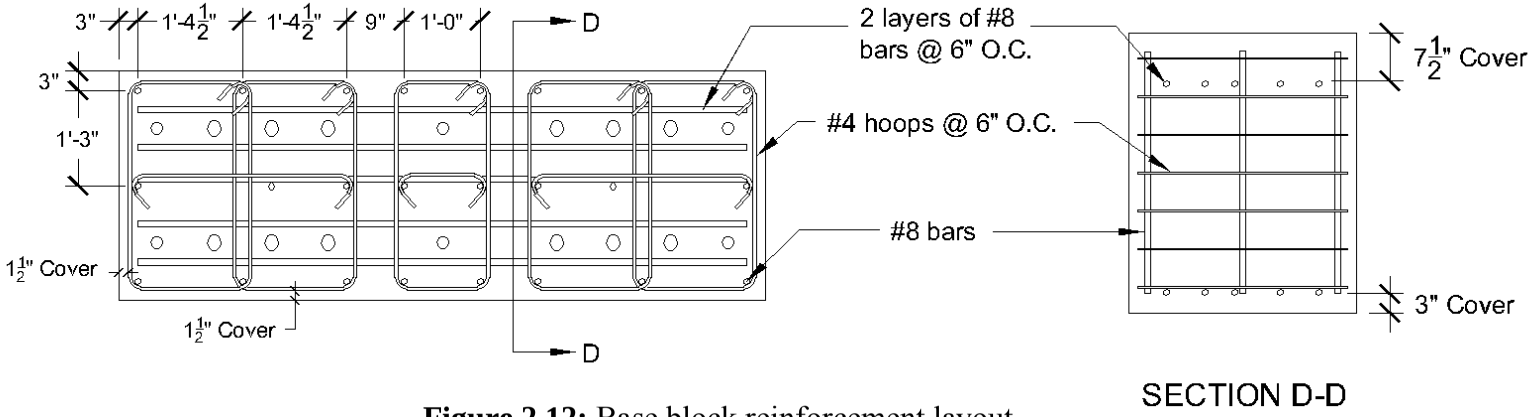

Figure 2.12: Base block reinforcement layout

2.3 Material Properties

2.3.1 Concrete

The target compressive strength of the concrete f_c' was 3000 psi. The concrete mix had normal-weight aggregate with a maximum aggregate size of ¾ in. Mix specifications and design quantities for the concrete are shown in Tables 2.1 and 2.2. The concrete was supplied by LRM Industries, a local ready-mix supplier. Twenty-four 6-in. diameter by 12-in. tall standard cylindrical compressive strength specimens and two 6-in. by 6-in. by 22-in. flexural strength specimens were cast from the middle third of each batch. Compressive and flexural strength specimens were cured and stored with the column specimens to match the concrete properties of the columns as accurately as possible.

Compressive strength tests were performed at 7, 14, 21, and 28 days after casting, as well as on the final day of column testing, in accordance with ASTM C 39. The compressive strengths listed in Table 2.3 represent the average strength determined using two cylinders for the 7, 14, and 21-day tests, and three cylinders for the 28-day and test day strengths. Two flexural strength tests and one modulus of elasticity test were also conducted on the final day of column testing, in accordance with ASTM C 78 and ASTM C 469, respectively. The average flexural strength f_r and modulus of elasticity E_c for each of the two specimens are also listed in Table 2.3.

Table 2.1: Concrete mix specifications

Type I/II Cement	ASTM C 150
Class C Fly Ash	ASTM C 618
Coarse Aggregate	ASTM C 33
Fine Aggregate	ASTM C 33
Water Reducer	ASTM C 94 – Type A
28-Day Design Strength, f'_c	3000 psi
Maximum Size Aggregate	¾ in.
Slump	4 in.
Water/Cement Ratio	0.49

Table 2.2: Concrete mix design quantities

Material	**Weight**
Type I/II Cement	300 lb
Class C Fly Ash	125 lb
Coarse Aggregate	1852 lb
Fine Aggregate	1566 lb
Water	210 lb
Water Reducer	12.8 oz

Table 2.3: Measured concrete material properties

Concrete Property	**Specimen 1**	**Specimen 2**
Measured Slump	1.75 in.	1.75 in.
7-Day strength	3420 psi	3340 psi
14-Day strength	4180 psi	4540 psi
21-Day strength	4600 psi	4670 psi
28-Day strength	5010 psi	4700 psi
Test Day strength	4800 psi	4880 psi
Flexural strength, f_r	740 psi	870 psi
Modulus of elasticity, E_c	3770 ksi	3610 ksi

2.3.2 Reinforcing Steel

ASTM A706 steel reinforcement was used for all longitudinal bars in the column. Column hoops and all beam reinforcement consisted of ASTM A615 steel. Tensile tests were performed on both the No. 9 longitudinal bars and No. 3 transverse hoops, from which the average yield stresses f_{yl} and f_{yt} were determined to be 64 ksi and 54 ksi, respectively. The measured stress-strain relationships for the reinforcing steel bars are shown in Figures 2.13 and 2.14.

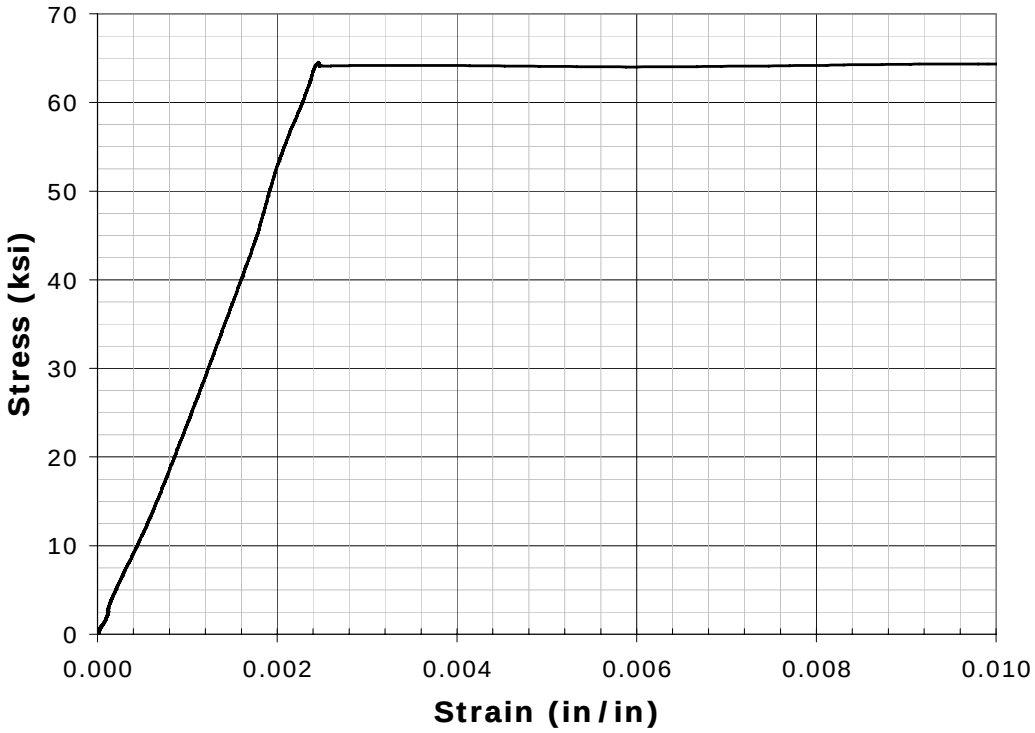

Figure 2.13: Stress-strain relationship for No. 9 ASTM A706 reinforcing steel

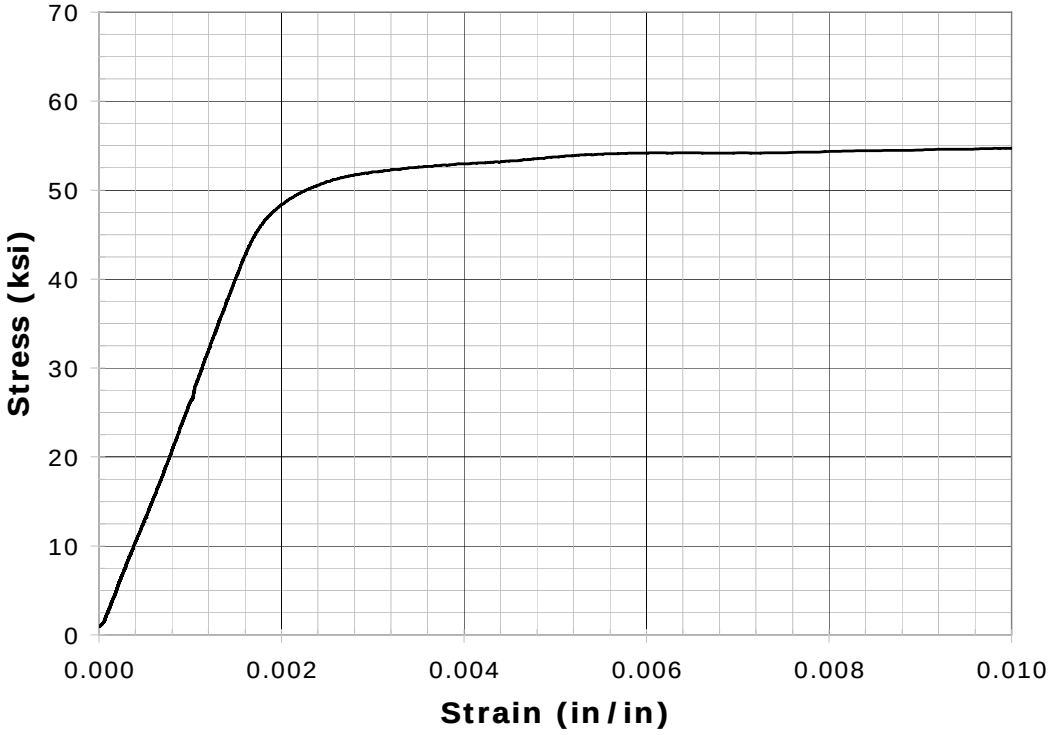

Figure 2.14: Stress-strain relationship for No. 3 ASTM A615 reinforcing steel

2.4 Specimen Construction

Wood formwork and reinforcing steel cages were constructed in the Structural Testing Laboratory at the University of Kansas. Specimens were cast in forms constructed using 2x4 in. studs and ¾-in. medium density overlay plywood. Forms were protected using baby oil as a release agent for all surfaces exposed to concrete. Reinforcing bars were cut and bent by Gerdau Ameristeel, a local supplier. Prior to tying the cages, deformations were removed from the reinforcing steel bars at the locations where strain gages were to be attached. Cages were assembled using standard 4-in., 8-in., and 10-in. wire ties. Standard steel reinforcement chairs were

attached to reinforcing bars in both the beam and column regions as necessary, to achieve cover tolerances. Formwork and typical reinforcing cages are shown in Figures 2.15 through 2.17.

Strain gages were obtained from Vishay Micro-Measurements. A total of 60 CEA-06, ¼-in. long, 120-Ω gages were attached to the longitudinal reinforcing bars, and 16 CEA-06, ⅛-in. long, 120-Ω gages were attached to the column hoops. Prior to attaching the strain gages, the surface of the reinforcement was cleaned and prepared according to specifications provided by the manufacturer. After the gages were attached, they were sealed with wax and covered with M-Coat J, a protective coating used to shield the gages from damage during casting.

The specimens were cast in the horizontal position, using a single batch of five cubic yards of concrete per specimen. The concrete was placed in two lifts, with samples taken for strength specimens between the two lifts. The concrete was consolidated by internal vibration to minimize the presence of voids, as shown in Figure 2.18. Following placement and vibration of the second lift, the top surface of the specimen was struck off and finished using hand trowels. Figure 2.19 shows a photograph of a specimen immediately following finishing procedures. Afterward, the specimen was covered with wet burlap and plastic sheeting. Wood formwork was stripped after four days of moist curing and the specimens were air-dried as they were stored inside the Structural Testing Laboratory until they were ready to be transported to the MAST Laboratory.

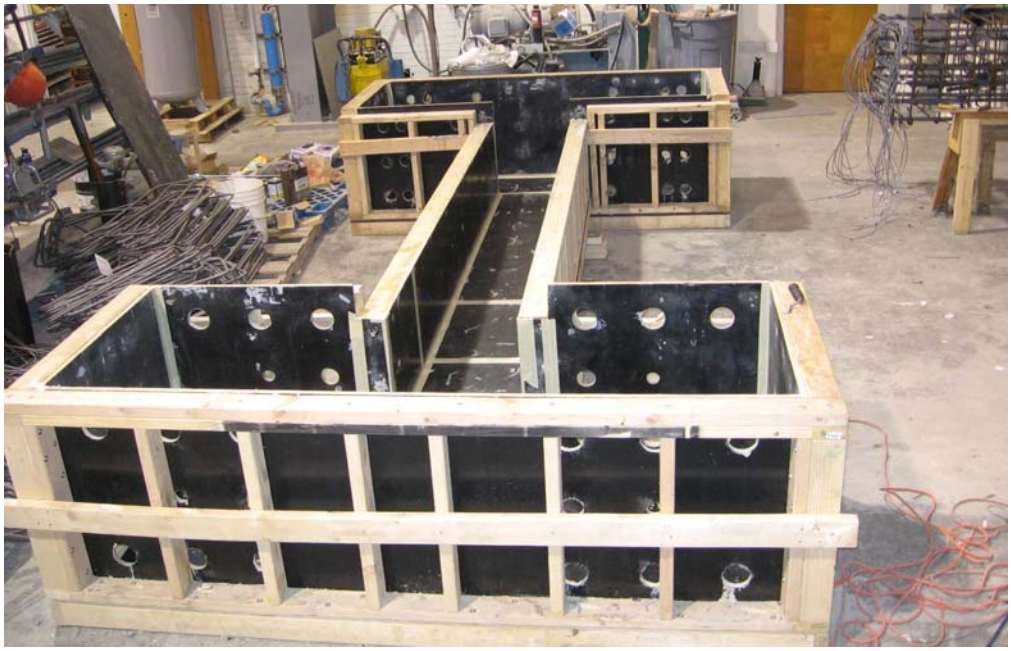

Figure 2.15: Specimen formwork

Figure 2.16: Typical specimen reinforcing cage

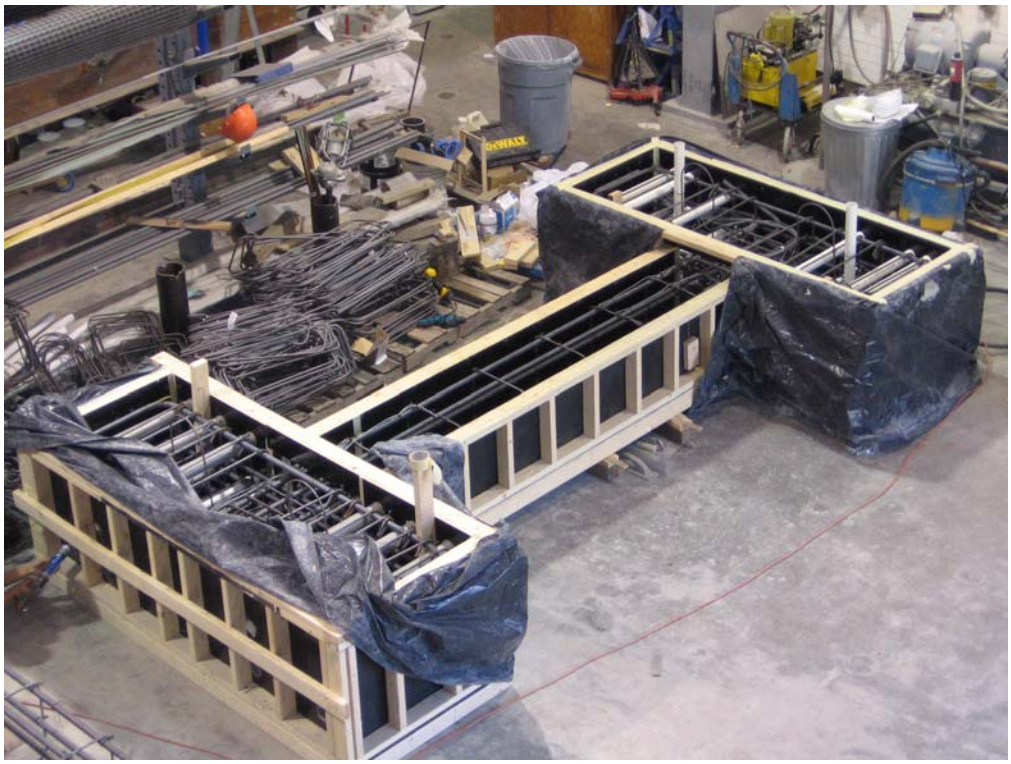

Figure 2.17: Reinforcing cage in form, prior to casting

Figure 2.18: Internal vibration during concrete placement

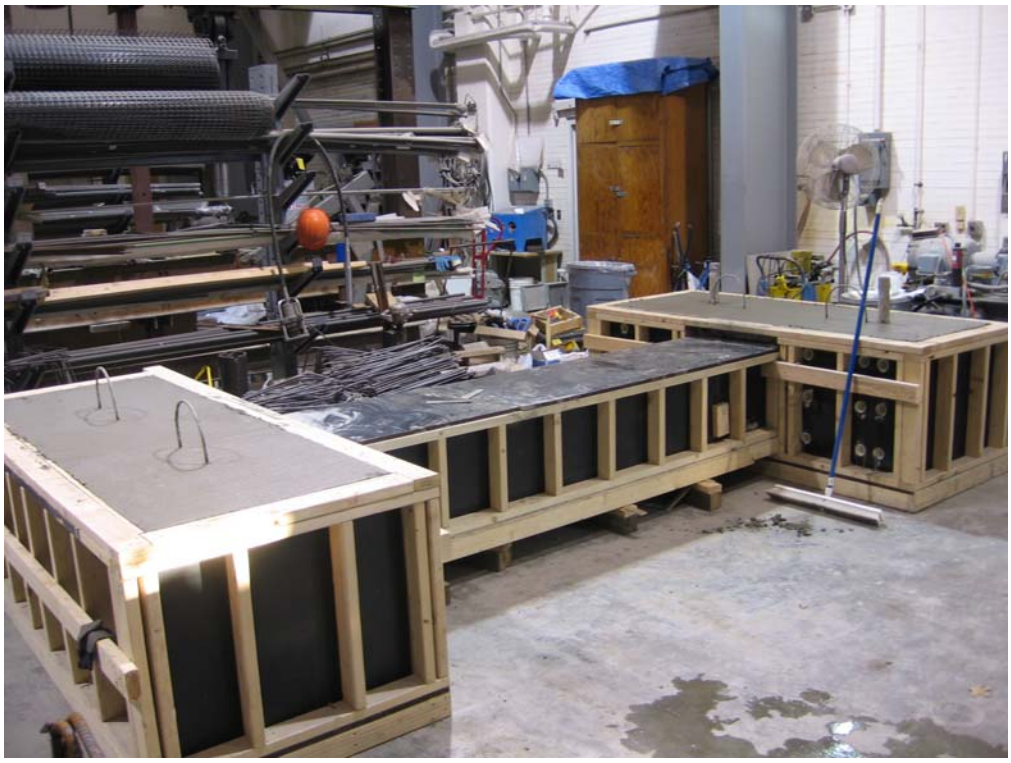

Figure 2.19: Finished column test specimen

In order to prevent cracking during handling and transport, two 1½-in. diameter threaded rods were cast into the bottom beam, and placed through openings in the top beam, 9 in. from either side of the column. Each rod was instrumented with strain gages assembled into a full Wheatstone bridge configuration to form a load cell, which was used to monitor the force in the rod. Each rod was tensioned to 30 kips (approximately $0.02\, A_g\, f_c'$ per rod) using 1½-in. diameter torque nuts over 8-in. by 8-in. by 1½-in. thick plate washers.

2.5 Test Setup

Testing was performed at the MAST (Multi-Axial Subassembly Testing) Laboratory at the University of Minnesota. Following construction and curing, the specimens and base block were shipped to the laboratory on a flatbed truck and unloaded by the laboratory staff. After arrival at the MAST Laboratory, the specimens were tilted up into the vertical position using the frame shown in Figure 2.20. The base block and specimens were then moved from the staging area of the laboratory to the reaction floor using the crane. Final positioning was performed using the crosshead of the multi-axial loading system.

Figure 2.20: Tilt-up frame used to rotate specimens into the vertical position

The base block was post-tensioned to the reaction floor using six 1½-in. diameter ASTM A193 Grade B7 threaded rods, 1½-in. standard nuts, and 1½-in. thick A36 steel plate washers. UltraCal 30 grout was poured through two 1¼-in. diameter holes in either side of the base block to ensure uniform contact and load distribution to the reaction floor. Following final positioning of the base block, the column specimen was placed on top of the base block. After placement, the specimen was post-tensioned to the reaction floor using twelve 2-in. diameter ASTM A193 Grade B7 threaded rods, passing through ducts in the base block. The rods were fastened to the specimen using 2-in. torque nuts, and 1½-in. thick A36 steel plate washers. UltraCal 30 grout was used again to fill all voids at the base block-column specimen interface to obtain uniform load distribution. After the instrumentation was attached to the specimen, as discussed in Section 2.7, the top beam was post-tensioned to the crosshead, as shown in Figure 2.21, using eighteen 1½-in. diameter ASTM A193 Grade B7 threaded rods, 1½-in. torque nuts, and 1½-in. thick A36 steel plate washers. Grout was then poured through holes in the crosshead to achieve uniform load distribution to the top beam.

Figure 2.22 shows the testing assembly that was used to induce axial and lateral loads. Specimens were loaded axially using four 330-kip hydraulic actuators attached to each of the four arms of the crosshead. Lateral loading was applied by two 440-kip hydraulic actuators, attached horizontally to the side of the crosshead. All actuators were capable of operating in either force or displacement control mode, allowing for independent control of all degrees of freedom.

Figure 2.21: Top beam connection to the crosshead

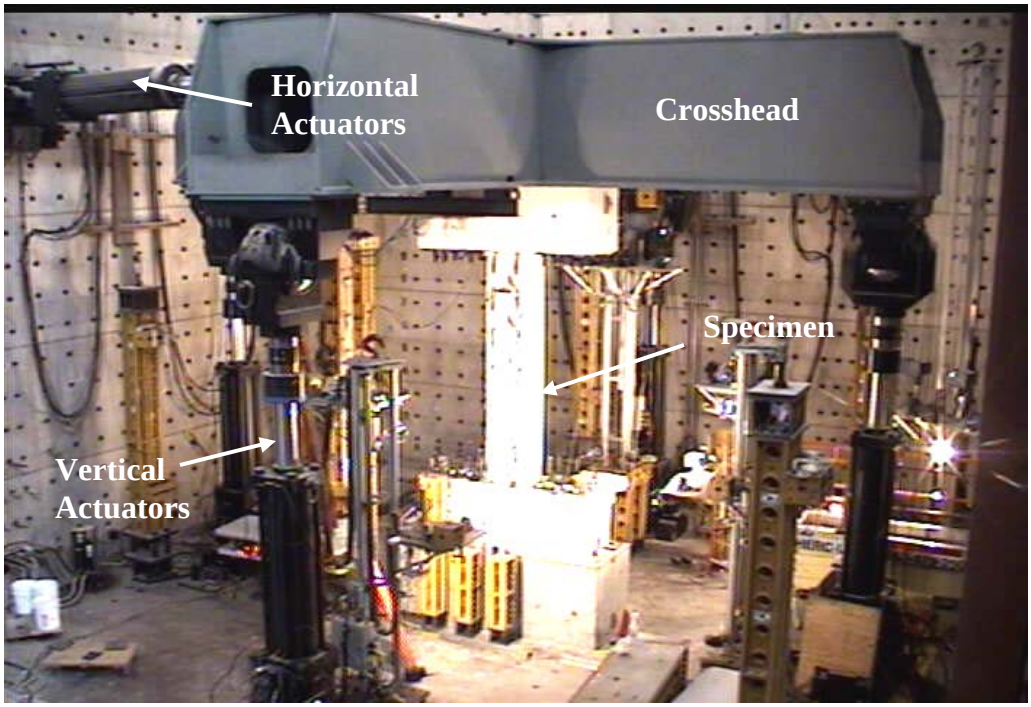

Figure 2.22: Test configuration

2.6 Loading and Displacement History

The axial load applied to each specimen was maintained at a constant value throughout the first phase of both tests to simulate the behavior of an interior building column. For the first test, axial load remained constant at a load of 500 kips. This corresponded to approximately $0.50\,A_g\,f_c'$ using the target concrete compressive strength of 3000 psi and $0.32\,A_g\,f_c'$ using the measured compressive strength of 4800 psi. The axial load for the second test was maintained constant at 340 kips, which corresponded to $0.35\,A_g\,f_c'$ and $0.22\,A_g\,f_c'$ based on the target and measured compressive strengths, respectively.

The maximum lateral displacement was maintained constant for sets of three cycles and was increased after each set of three cycles was completed. The peak displacement for each set of three cycles was established on the basis of drift ratio. Peak drift ratios used for each set of cycles began at 0.125% and were subsequently set at 0.25% increments, up to a drift ratio of 1.50%. Beyond a drift ratio of 1.50%, the magnitude of each increment was changed to 0.50%, up to axial failure. The applied displacement history is shown in Figure 2.23.

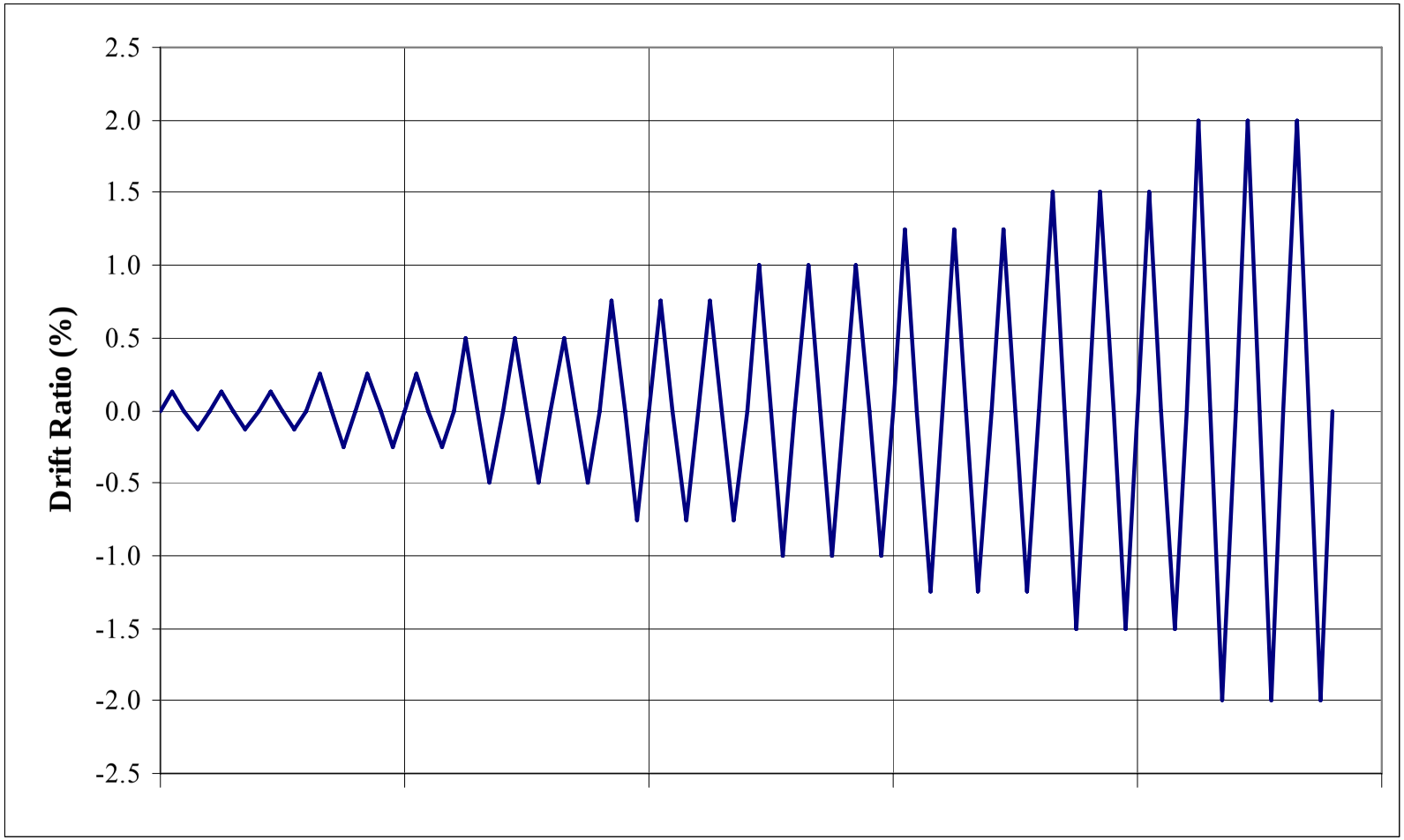

Figure 2.23: Displacement history used for both specimens

During testing, the vertical actuators were programmed to run simultaneously in force-control mode to maintain a constant axial load, and in displacement-control mode to prevent rotation of the top beam. Horizontal actuators were programmed to operate in displacement-control mode, according to the displacement history shown in Figure 2.23. Lateral loading was applied in the east-west direction, defined such that east was considered positive displacement. The horizontal actuators were also used to restrain motion in the north-south direction. During testing, the maximum north-south displacement that was measured was approximately 0.004 in. for both tests. The maximum measured east-west rotation of the top beam for both tests was 0.001 degrees. The maximum recorded slip of the bottom beam with respect to the floor was 0.005 in. for the first test and 0.01 in. for the second test.

An axial failure event was defined as a loss of 10% of the axial load carrying capacity. At this point, the vertical actuators were programmed to shift from force-control mode to displacement-control mode, such that the actuators would retain the vertical displacement of the column at the time of axial failure. Following an axial failure event, the system was transitioned back to force-control mode in the vertical direction, under a reduced axial load, and the standard displacement protocol was continued. When the damage in the columns was deemed too severe, the displacement protocol was modified such that the vertical deformation was increased uniformly, while maintaining a constant level of maximum lateral displacement. This modification to the displacement protocol was intended to measure the residual axial capacity of the columns.

2.7 Instrumentation

During each test, 124 channels of data were recorded. This included 76 strain gages, 23 Linear Variable Differential Transformers (LVDTs), 11 string potentiometers, and 14 load and displacement channels set up to monitor the motion of the crosshead. Additional derived channels were also set up to calculate various parameters such as column shortening and uplift at the base of the column, for reference during testing. All data was acquired and stored using the data acquisition system at the MAST Laboratory. The recording frequency for the data acquisition system was set at 1.0 Hz. for testing and 0.10 Hz. for overnight monitoring purposes. Data acquisition began prior to applying axial load. After loading, all instrumentation channels were reset to zero before initiating the lateral loading protocol. Because all recorded strain gage channels were reset to zero after application of the axial load, additional derived channels were created to correct the readings by adding back in the strain induced during axial loading.

Placement and labeling of strain gages for both the longitudinal and transverse reinforcement are shown in Figures 2.24 and 2.25. Sixty of the 76 total strain gages were placed at ten different heights along the column longitudinal reinforcement. This included two locations within the top beam, one at each of the top and bottom beam-column interfaces, four within the column, and two within the bottom beam. At each location, six strain gages were placed on the surface of the bar, parallel to the longitudinal axis of the bar. The remaining 16 strain gages were attached to column

hoops 1, 2, 5, and 6. On each hoop, two gages were attached to each of the faces of the hoop parallel to the lateral loading direction, as shown in Figure 2.25.

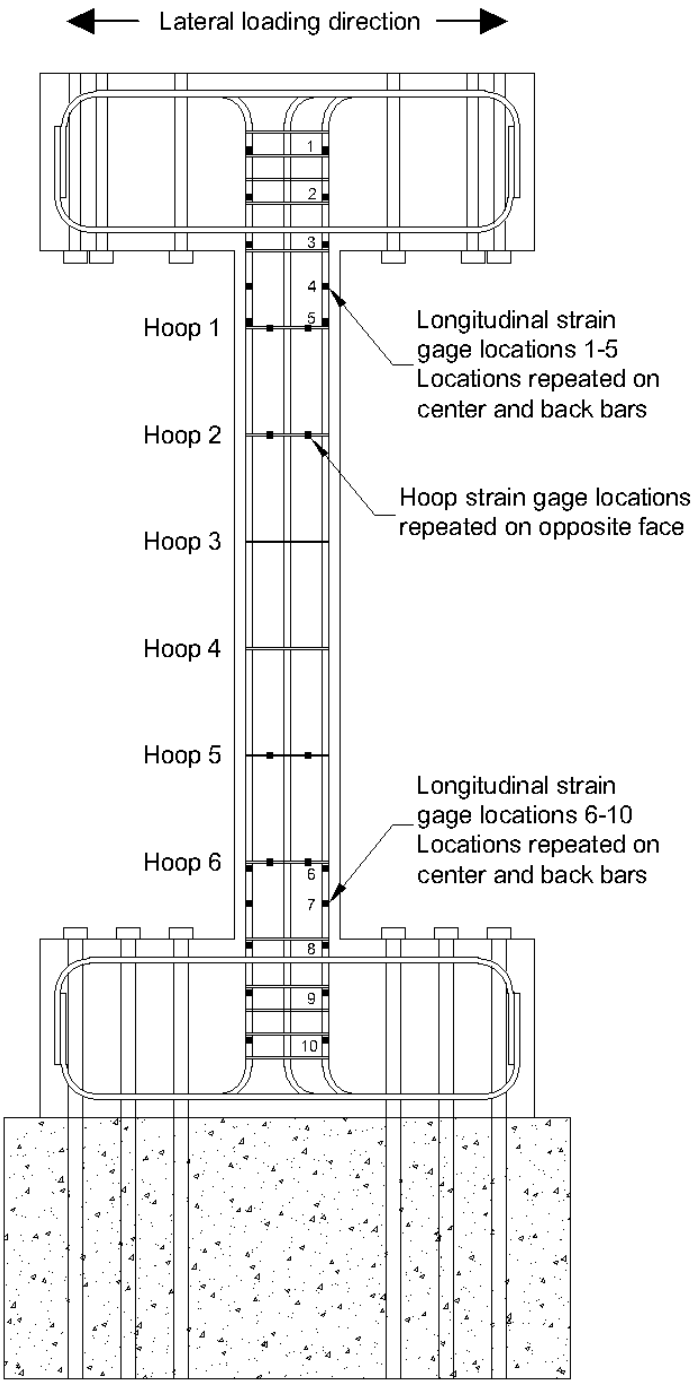

Figure 2.24: Strain gage placement

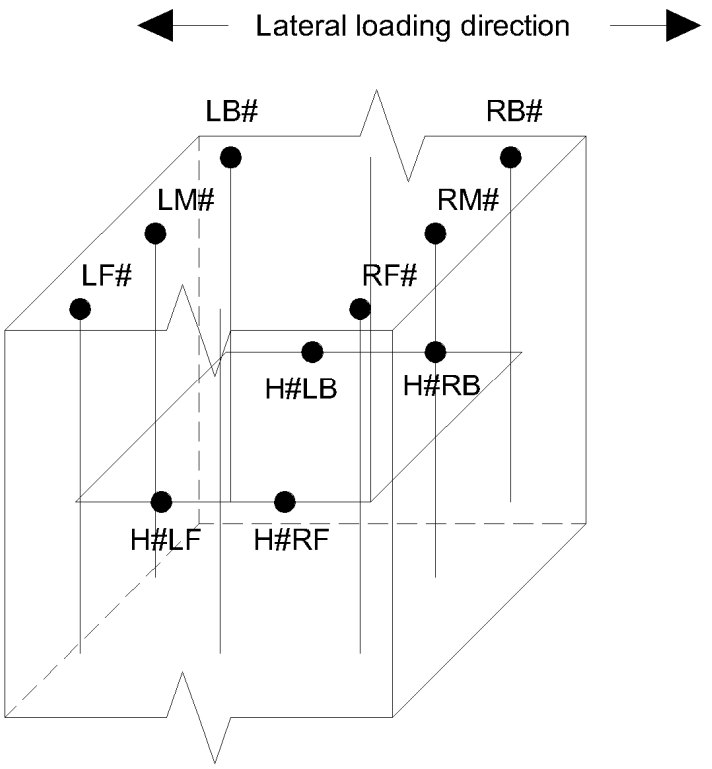

Figure 2.25: Strain gage locations and labeling

LVDTs were attached along the height of the column, as shown in Figure 2.26, to measure relative vertical, diagonal, and horizontal displacements within the column. Attachments were made to the column using aluminum brackets that were connected to threaded rods embedded at 19-in. intervals along the surface of the column, as shown in Figure 2.27. Depending on the anticipated displacement at a particular location, LVDTs with a total range of either 2.0 or 1.0 in. were used. Additional LVDTs with a range of 1.0 in. were attached from the bottom beam to reference frames connected to the reaction floor to measure slip and uplift at the base of the specimen.

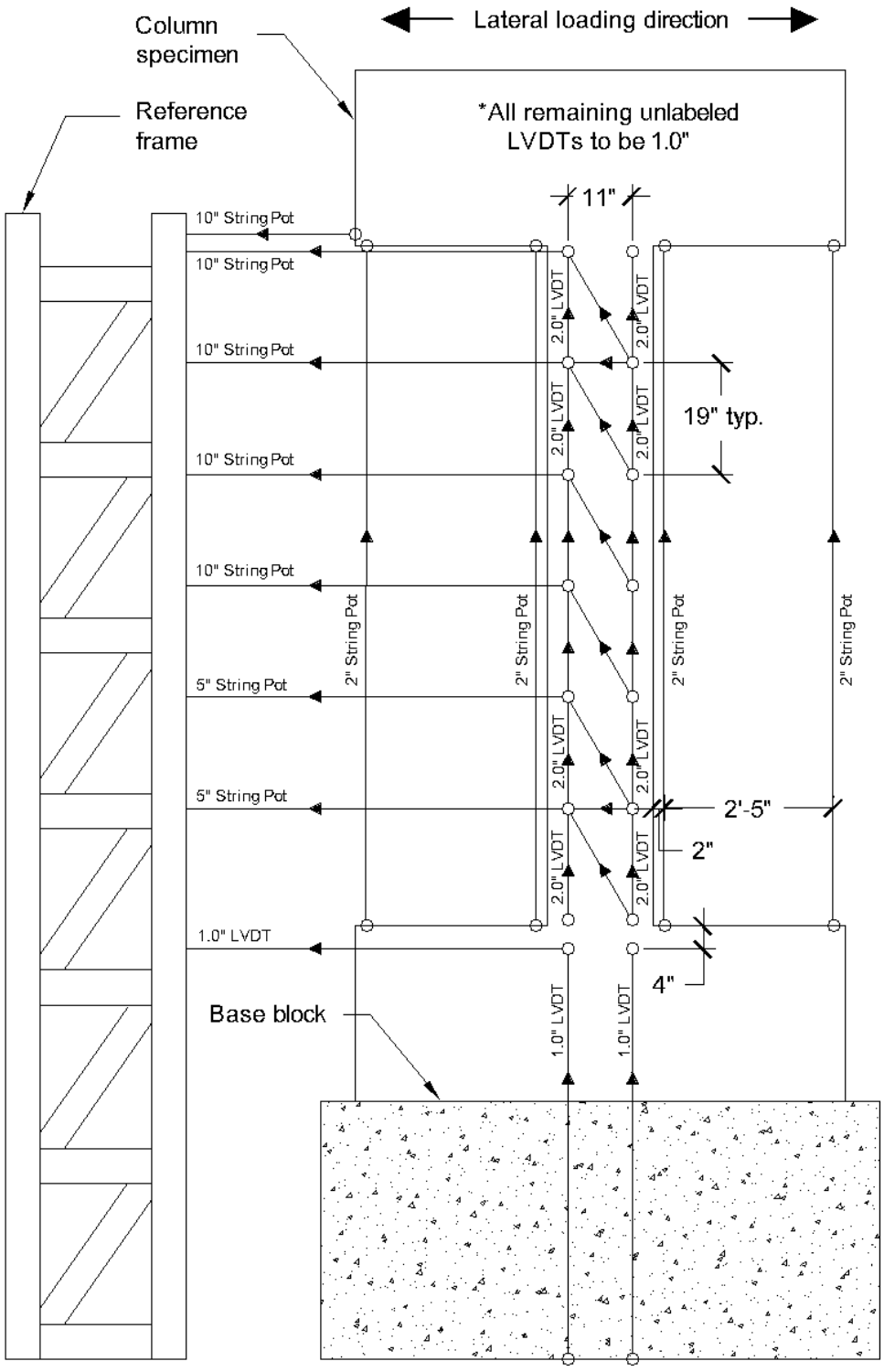

Figure 2.26: LVDT and string potentiometer placement

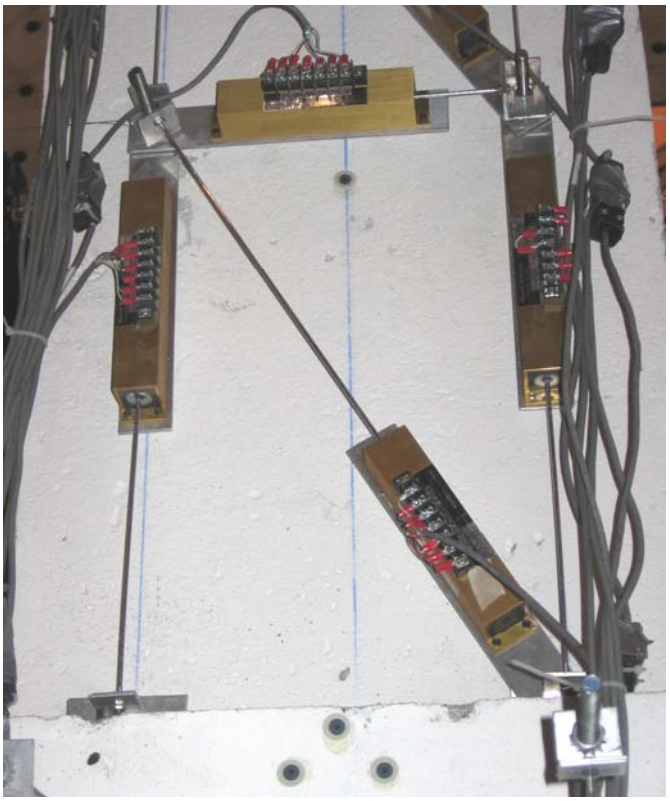

Figure 2.27: LVDT attachment to the column

The lateral displacement of the specimen was measured using string potentiometers. String potentiometers were attached to a steel reference frame that was bolted to the reaction floor approximately five feet away from the specimen, as shown in Figure 2.28. Wires were attached from the reference frame to the threaded rods on the column face where the LVDTs were connected. A string potentiometer attached from the reference frame to the bottom surface of the center of the top beam was used to control the lateral displacement history, as it measured the maximum displacement at the top of the column. Four additional string potentiometers were attached vertically from the top beam to the bottom beam. Two of these

potentiometers were placed at the ends of the beams, to measure rotation of the top beam, and two others were located along the sides of the column, to measure column shortening. Placement of all string potentiometers is shown in Figure 2.26.

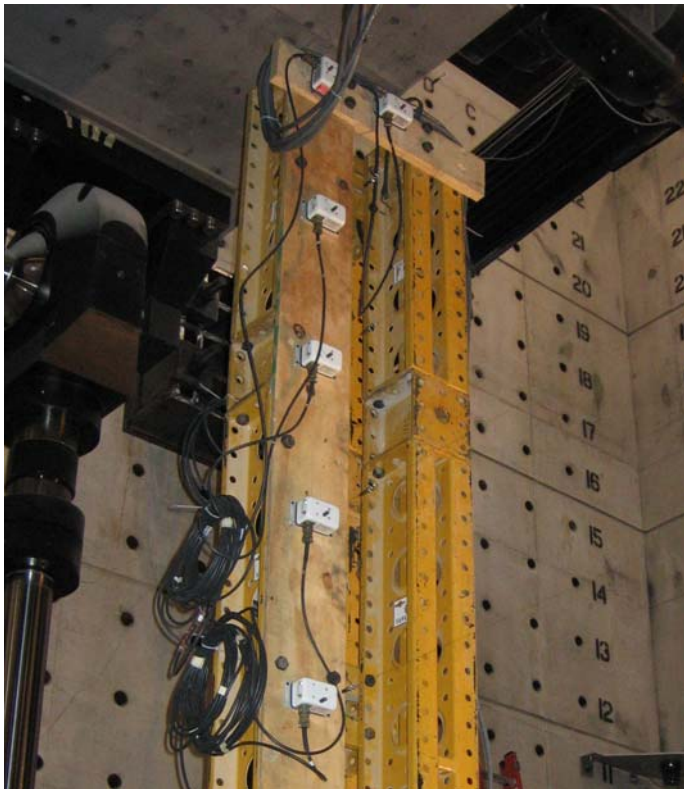

Figure 2.28: String potentiometer attachment to the reference frame

2.8 Telepresence

Four camera towers were used to obtain a photographic record of each test. Each tower had two shelves, each with one still and one video camera, as shown in Figure 2.29. The layout of the camera towers is shown in Figure 2.30. A set of photographs was taken with all cameras at the peak lateral drift ratio for each cycle. Two additional data collection methods were used to achieve a greater degree of detail and accuracy in the monitoring of deformations in the maximum moment regions of the columns.

Figure 2.29: Telepresence camera tower

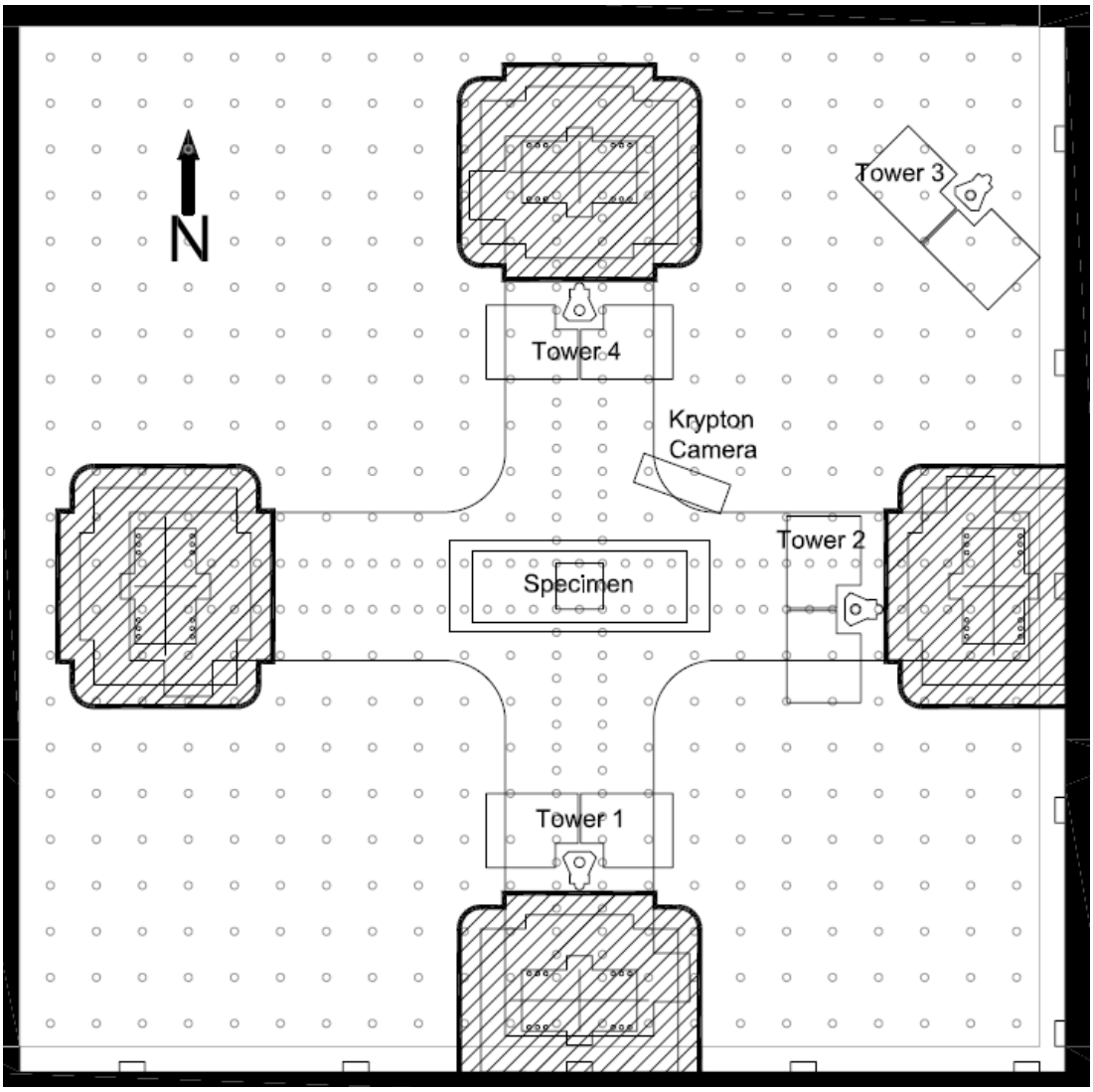

Figure 2.30: Telepresence camera tower layout

2.8.1 Photogrammetry

Deformations in the maximum moment region at the top of the column were monitored using a 5x5 array of photo taggers placed on the north face of the column, as shown in Figure 2.31. The photo taggers consisted of 1 1/16-in. diameter circle stickers with a ⅛-in. diameter black dot in the center and concentric rings of lighter shades of gray around the center dot. The motion of these taggers was captured by taking photographs of this region at set displacement intervals during testing. Loading was paused to take sets of photographs at zero and maximum displacement values, and at three even displacement intervals between the two, for a total of sixteen sets of photographs for each displacement cycle.

2.8.2 Krypton System

Deformations in the maximum moment region at the bottom of the column were monitored using a Metris K600 (Krypton) system. This system consisted of a camera, a set of infrared LEDs, and control software. For data acquisition during testing, the Krypton camera was mounted on a reference frame approximately eight feet away from the specimen. A 5x5 array of LEDs was hot-glued to the bottom of the north face of the specimen, laid out as shown in Figure 2.31. Along with the 25 LEDs on the specimen, three additional LEDs were mounted to a reference frame next to the specimen which acted as a fixed reference coordinate system. Using the reference LEDs, the Krypton system was able to triangulate the 3-dimensional position of the specimen LEDs.

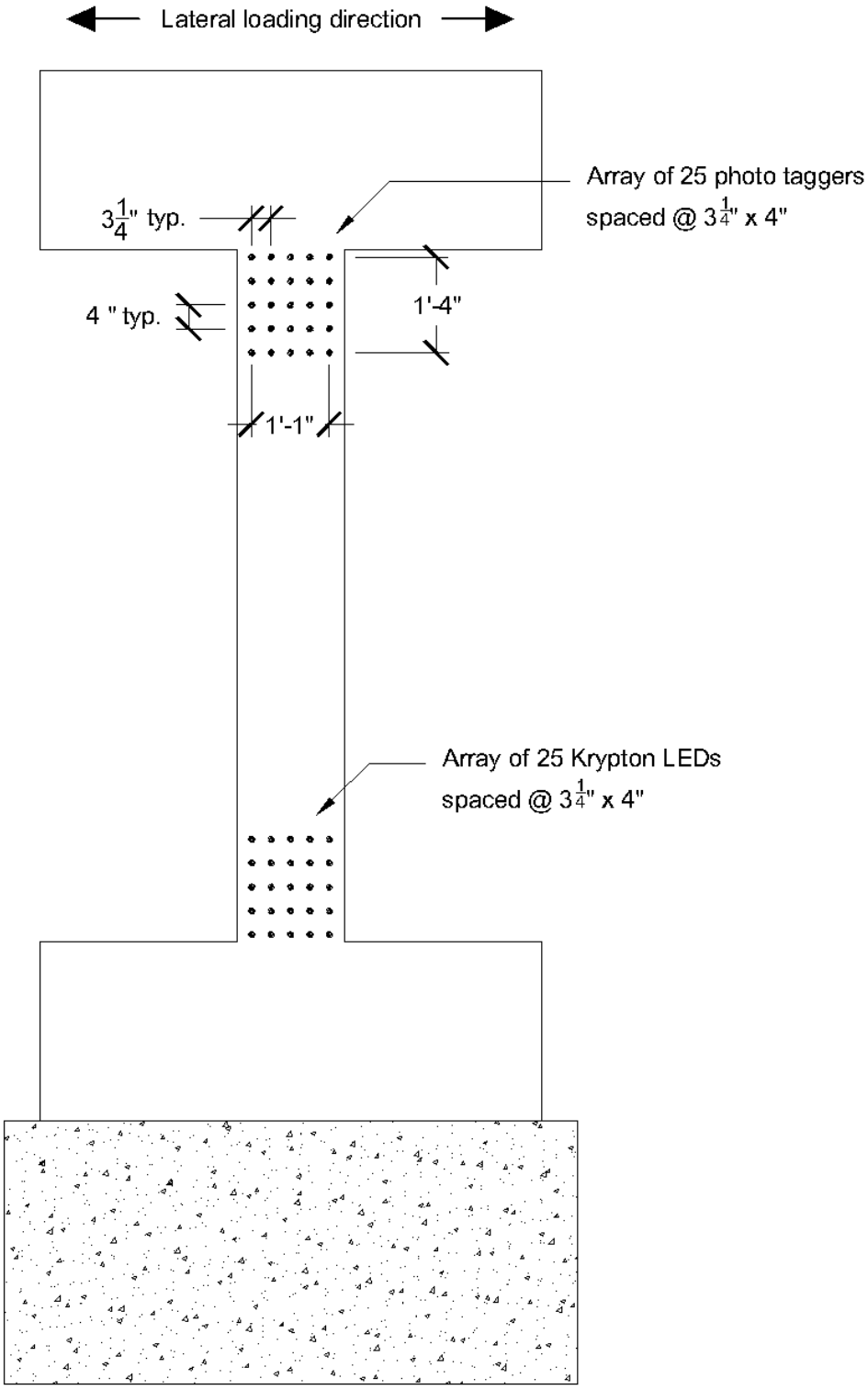

Figure 2.31: Photo tagger and Krypton LED layout

CHAPTER 3: TEST RESULTS

3.1 Introduction

Two full-scale reinforced concrete building columns were tested to failure under constant axial and cyclic lateral loading. Results from each of these tests reported in this Chapter include a description of the progression of damage and a summary of the measured data taken throughout each test. The following designation is used throughout this Chapter; references to a 1.00% drift ratio cycle refer to a load cycle with a maximum lateral displacement corresponding to a drift ratio of 1.00%, and likewise for other drift ratios. Measured data presented in this Chapter includes the lateral load-deflection and moment-curvature relationships for each specimen, as well as the measured deflection components, bar strain, and shear capacity. Results from predictive and behavioral models are also presented and compared with measured and observed data from each test.

3.2 Damage Progression – Specimen 1

Specimen 1 was subjected to a constant axial load of 500 kips, or approximately $0.50 A_g f_c'$ for the target concrete compressive strength of 3,000 psi. The applied lateral displacement protocol is described in Section 2.6 and shown in Figure 2.23.

Before loading began, hairline cracks were observed on the top and bottom beams, as a result of post-tensioning the specimen to the crosshead and the reaction floor. During the initial displacement cycles to a maximum drift ratio of 0.125%,

hairline cracks were observed at the interfaces between the column and the beams. During these displacement cycles, no cracking was observed on any of the column faces.

Beginning at cycles to a drift ratio of 0.25%, horizontal flexural cracks were observed on the east and west faces of the column, perpendicular to the lateral loading direction. At subsequent cycles to a 0.25% drift ratio, the horizontal cracks propagated across the full width of the east and west faces of the column, extending deeper into the column and becoming visible on the north and south faces. These cracks opened and closed during each cycle. At this displacement level, all flexural cracks in the maximum moment regions of the specimen remained essentially horizontal in orientation, as shown in Figure 3.1.

During the first 0.50% drift ratio cycle, the horizontal flexural cracks observed on the north and south column faces began to change in orientation, turning at an angle indicative of shear cracking. Additional shear cracks formed and extended deeper into the column as cycling continued, with cracks from opposite faces of the column meeting in the center of the north and south faces, as displayed in Figure 3.2.

During the cycles to a drift ratio of 0.75%, there was significant growth in the inclined cracks on the north and south faces of the column, with cracks from opposite sides of the column crossing near the center of the north and south faces, as shown in Figure 3.3. Additional horizontal cracks formed on the east and west faces, along with several vertical cracks, indicating splitting of the concrete cover along the

longitudinal reinforcement. No cracking was observed in the middle third of the column at this displacement level.

Minor crushing of concrete began to occur on the flexural compression faces at the positive peak of the first 1.00% drift ratio cycle. During this displacement cycle, the inclined cracks continued to widen and propagate deeper into the north and south faces of the column. Upon reaching the negative peak of the first 1.00% drift ratio cycle, significant spalling of the concrete cover occurred at the bottom southeast corner of the column. While the test was paused at the negative peak for marking cracks, a large inclined crack continued to grow from the bottom of the west face of the column up towards the east column face, resulting in a simultaneous brittle shear and axial failure. Photos of the column following initial axial failure are shown in Figure 3.4. Prior to failure, the mean axial strain in the column was -0.13%. Immediately following axial failure, the control system transitioned the vertical actuators from load-control to displacement-control mode, as they were programmed to retain the vertical position of the column when the axial load capacity dropped by 10% or more. This limit was intended to prevent the column from total collapse and to protect the loading equipment. The column stabilized at an axial load of 185 kips and an axial strain of -0.41%.

At this point in the test, the vertical actuators were transitioned back to load-control mode and the axial load was increased while the lateral displacement was maintained constant, to verify that the column was indeed unable to sustain the initial axial load. The axial load peaked at 245 kips and an axial strain of -0.44% prior to a

second axial failure, after which the control system again transitioned to displacement-control mode. After the second axial failure event, the column stabilized at an axial load of 178 kips and an axial strain of -0.47%.

The axial load on the column was subsequently reduced to 100 kips and the standard lateral displacement protocol was resumed. During the third 1.00% drift ratio cycle, concrete cover on the bottom east face of the column was lost. The third axial failure event occurred while attempting to reach a lateral drift ratio of 1.25%, at a lateral displacement of approximately 1.40 in. and an axial strain of -0.70%. After axial failure, the column stabilized at an axial load of 67 kips and an axial strain of -0.73%. At this point, the vertical deformation was increased monotonically while maintaining the maximum lateral displacement, in order to measure the residual axial capacity of the column. The axial strain-axial force relationship of the specimen is plotted in Figure 3.6. Table 3.1 lists the axial load, lateral load, and axial strain prior to each axial failure event. In both Figure 3.6 and Table 3.1, negative axial force and axial strain correspond to compression and column shortening, respectively.

The condition of the column at the conclusion of testing is shown in Figure 3.5. The main failure plane can be seen as an inclined crack at the base of the column, extending approximately from the location of Hoop 6 (13 in. from the base of the column) on the west face, to the location of Hoop 5 (31 in. from the base of the column) on the east face. Buckling of the longitudinal reinforcement on the east face of the column, between Hoops 5 and 6, can also be observed. In addition, Hoop 6 opened up in the northwest corner, due to improper anchorage at the 90º bend, which

allowed the longitudinal bars on the west side to buckle outward as well. Anchorage failure was not observed in Hoop 5, which was able to restrain longitudinal bars on all sides. This resulted in a mushroom-shaped deformation pattern of the longitudinal bars.

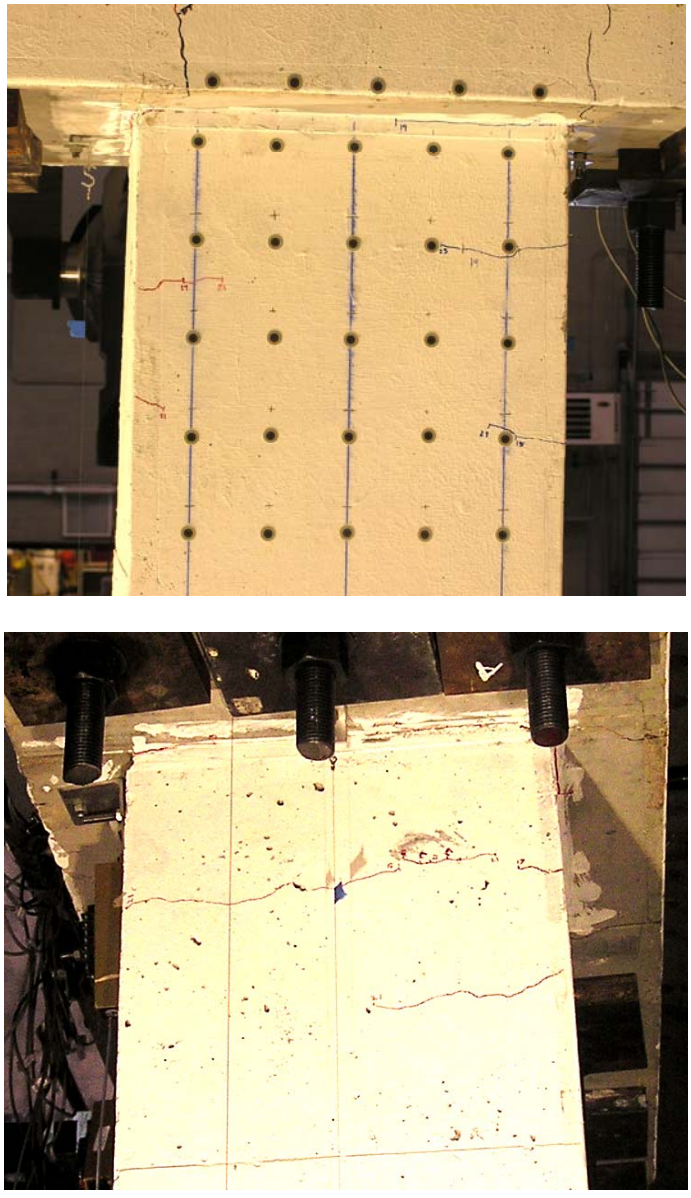

Figure 3.1: Specimen 1 crack pattern at a drift ratio of 0.25%

(a) Top column end, north face (b) Top column end, east face

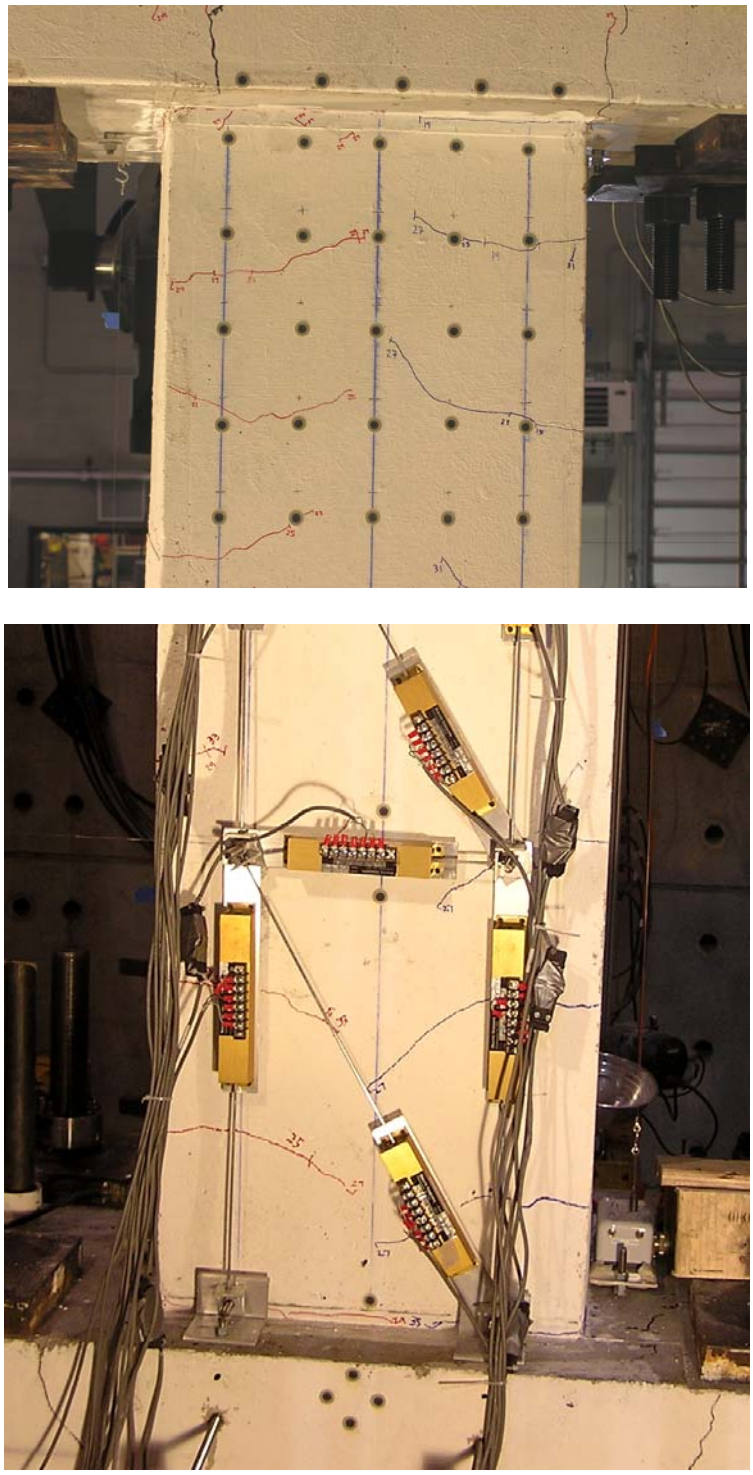

Figure 3.2: Specimen 1 crack pattern at a drift ratio of 0.50%

(a) Top column end, north face, (b) Bottom column end, south face

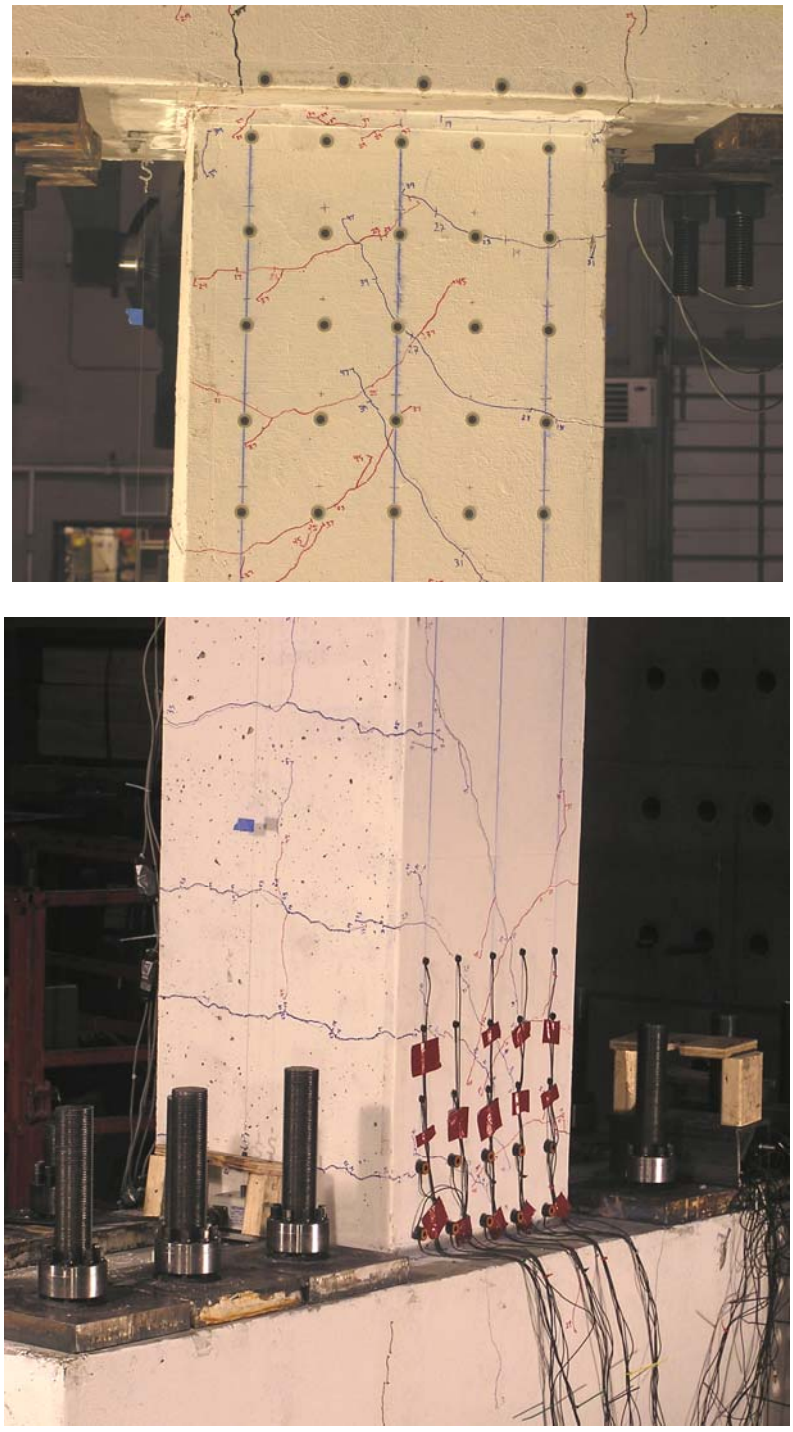

Figure 3.3: Specimen 1 crack pattern at a drift ratio of 0.75%

(a) Top column end, north face, (b) Bottom column end, northeast corner

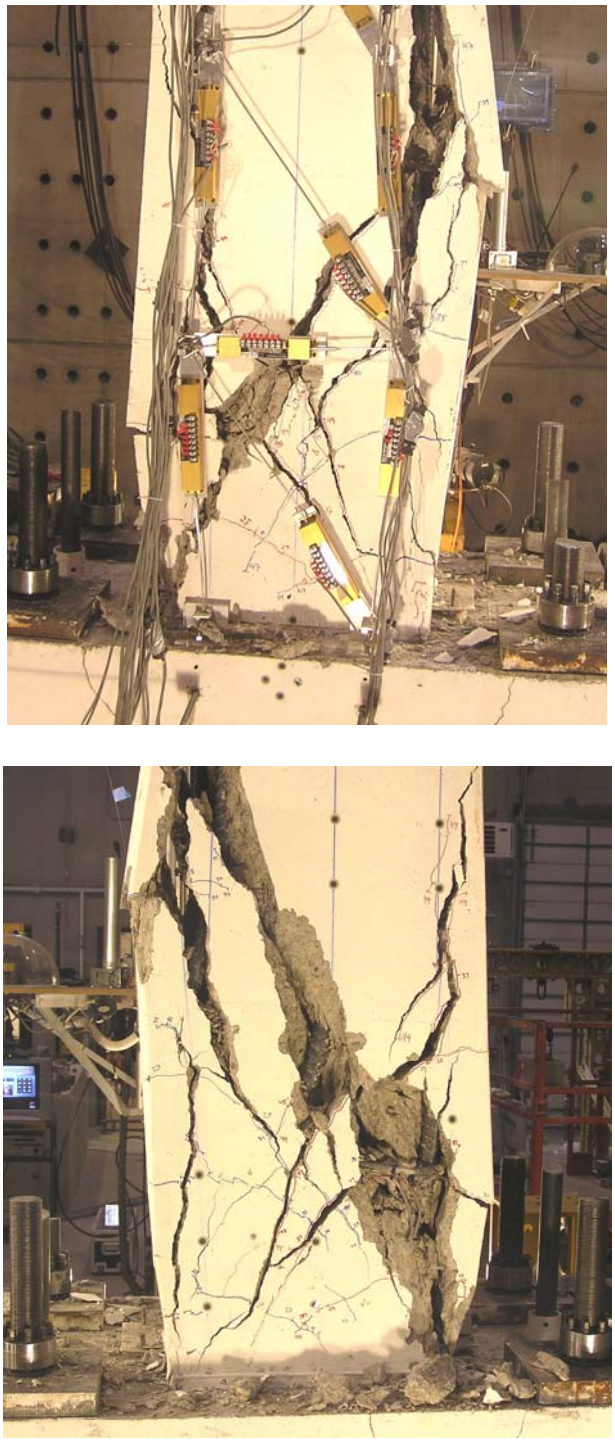

Figure 3.4: Specimen 1 crack pattern at a drift ratio of 1.00% (after axial failure)

(a) Bottom column end, south face, (b) Bottom column end, north face

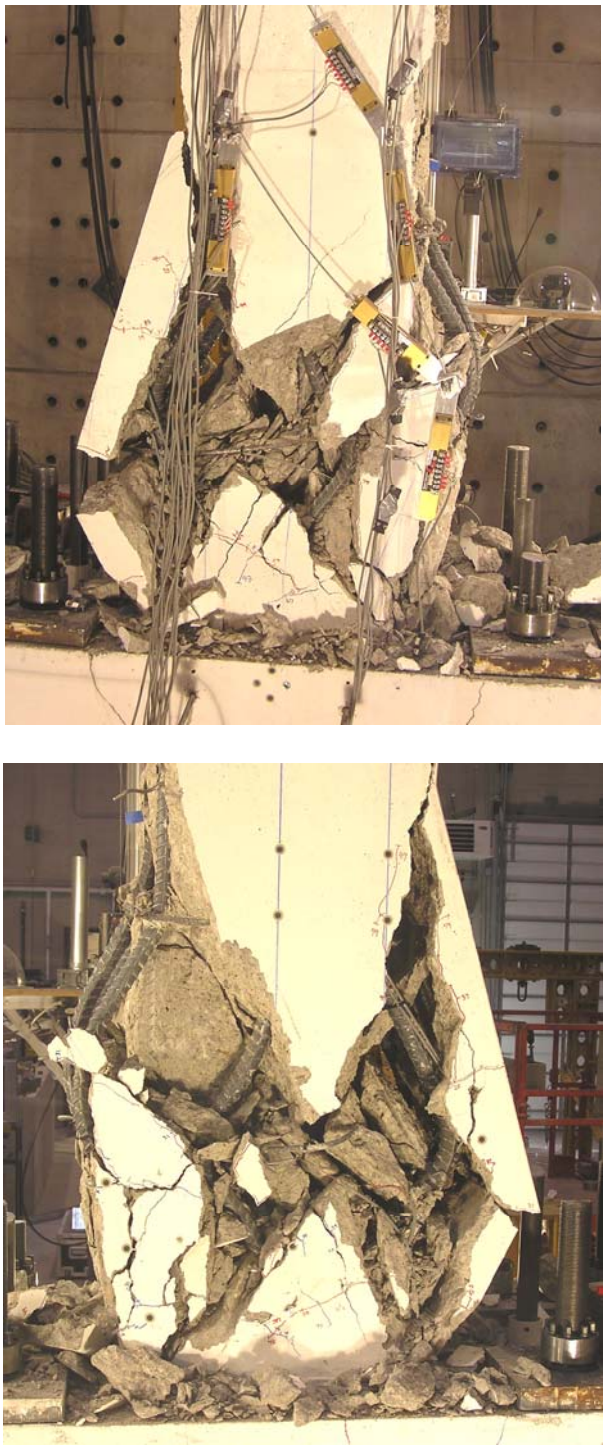

Figure 3.5: Specimen 1 condition at the end of the test

(a) Bottom column end, south face, (b) Bottom column end, north face

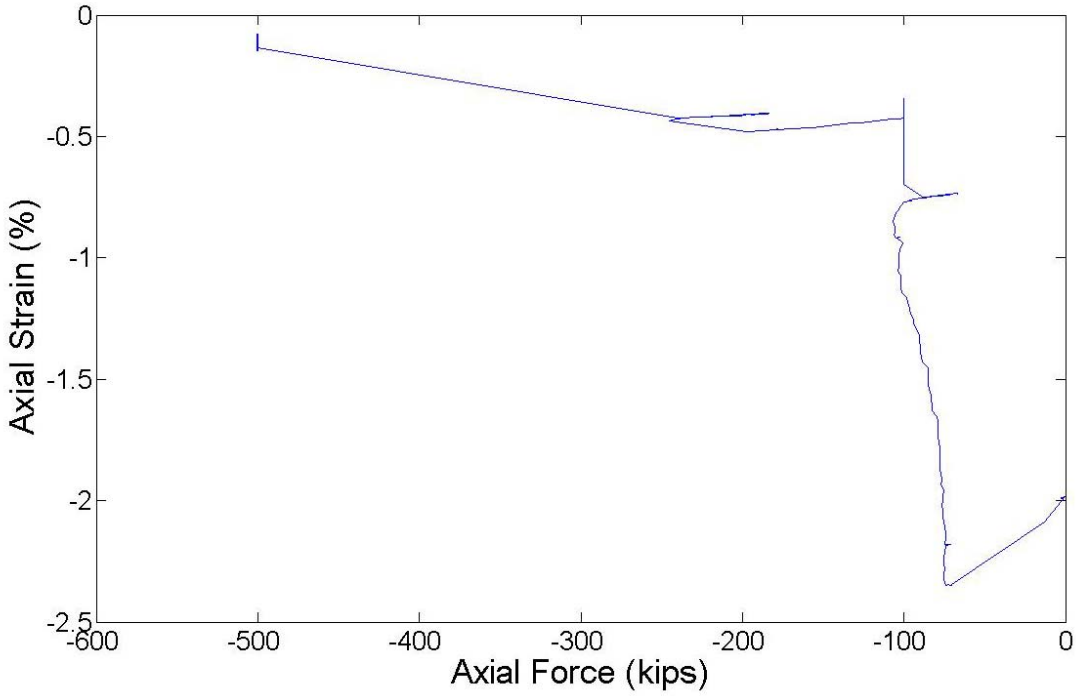

Figure 3.6: Axial strain-axial force response for Specimen 1

Table 3.1: Force and strain at axial failure for Specimen 1

Axial Failure Event	Axial Force	Lateral Force	Mean Axial Strain
1	-500 kips	59.6 kips	-0.13%
2	-245 kips	22.2 kips	-0.44%
3	-100 kips	10.3 kips	-0.70%

3.3 Damage Progression – Specimen 2

Specimen 2 was subjected to a constant axial load of 340 kips, or approximately $0.35 A_g f_c'$ for the target concrete compressive strength of 3,000 psi. The applied lateral displacement protocol was identical to that used for Specimen 1.

Similar to Specimen 1, hairline cracks were observed prior to lateral loading along the top and bottom beams due to post-tensioning the specimen to the crosshead and the reaction floor. During the 0.125% drift ratio cycles, hairline cracks were observed at the interfaces between the column and the beams. At this displacement level, no cracking was observed on any of the column faces.

During cycles to a drift ratio of 0.25%, horizontal flexural cracks were observed on the east and west column faces, perpendicular to the direction of lateral loading. At this displacement level, cracking was confined to the east and west faces of the column.

The horizontal cracks observed on the east and west column faces continued to grow during 0.50% drift ratio cycles, becoming visible on the north and south column faces. These cracks opened and closed during each cycle. Figure 3.7 indicates that at this displacement level, the orientation of all cracks remained essentially horizontal.

During 0.75% drift ratio cycles, the orientation of the cracks on the north and south column faces began to change, growing at angles indicative of shear cracking, as shown in Figure 3.8. These inclined cracks propagated deeper into the specimen as cycling continued, with cracks from opposite sides of the column meeting and

crossing near the center of the north and south faces. Additional horizontal flexural cracks were also observed on the east and west faces of the column.

The inclination of the shear cracks on the north and south faces of the column grew steeper during cycles to a drift ratio of 1.00%, as displayed in Figure 3.9. Maximum observed crack widths were on the order of 0.05 in. Vertical cracks also began to form on the east and west column faces during 1.00% drift ratio cycles, indicating splitting of the concrete cover along the longitudinal reinforcement. No cracks were observed in the middle third of the column at this displacement level.

At the first cycle with a peak drift ratio of 1.25%, spalling of the concrete cover began to occur on the compression faces of the maximum moment regions at the top and bottom of the column. In addition, significant growth in the width and length of the inclined cracks on the north and south column faces was observed. Figure 3.10 shows two major inclined cracks that formed a large X-shaped pattern extending across the center section of the column on the north and south faces. These large shear cracks resulted in a loss in axial capacity upon reaching the positive peak of the first 1.25% drift ratio cycle, at a mean axial strain of -0.035%. At axial failure, the axial strain increased to -0.056% and the vertical actuators transitioned from load to displacement-control mode, maintaining the vertical position constant and preventing the column from collapse. The column stabilized at an axial load of 318 kips and an axial strain of -0.044%.

Following initial axial failure, the axial load on the column was reduced to 300 kips and the standard lateral displacement protocol was resumed. The second

axial failure event occurred at a lateral drift ratio of 2.00%, and an axial strain of -0.20%. The column stabilized at an axial load of 250 kips and an axial strain of -0.26%. Axial loading was then resumed by increasing vertical deformation monotonically while maintaining lateral displacement constant, in order to examine the residual axial capacity of the column. Figure 3.12 plots the axial strain-axial force relationship for Specimen 2 throughout the test. Table 3.2 lists the axial load, lateral load, and axial strain data prior to each axial failure event.

The condition of the column at the completion of the test is shown in Figure 3.11. At the end of testing, Hoop 6 was still intact, while Hoop 5 had opened at the southeast corner, indicating an anchorage failure. The longitudinal bars on the west face of the column deformed between Hoops 5 and 6. On the east side of the column, the far northeast bar bent outward between Hoops 4 and 5, while the other two bars on the east side deformed outward between Hoop 4 and Hoop 6, as Hoop 5 had opened up. This resulted in an S-shaped deformation pattern of the longitudinal bars.

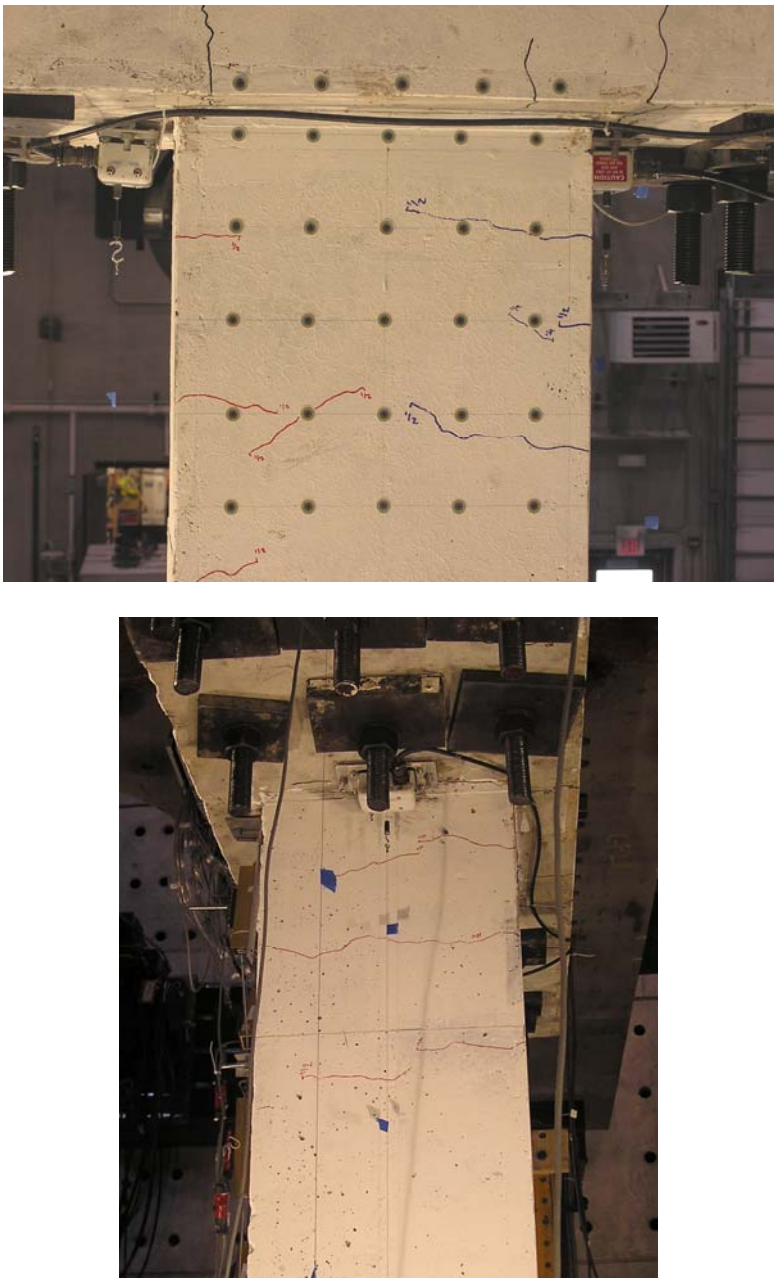

Figure 3.7: Specimen 2 crack pattern at a drift ratio of 0.50%

(a) Top column end, north face (b) Top column end, east face

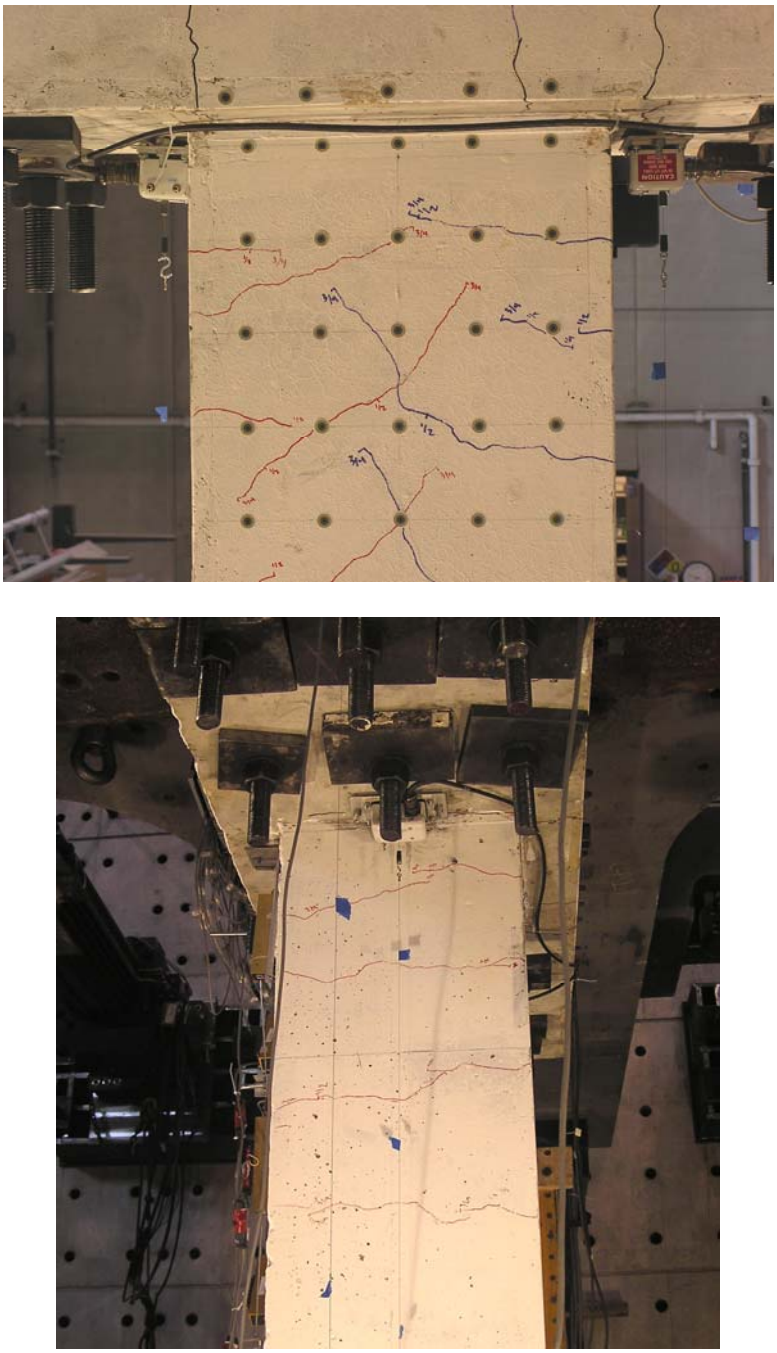

Figure 3.8: Specimen 2 crack pattern at a drift ratio of 0.75%

(a) Top column end, north face (b) Top column end, east face

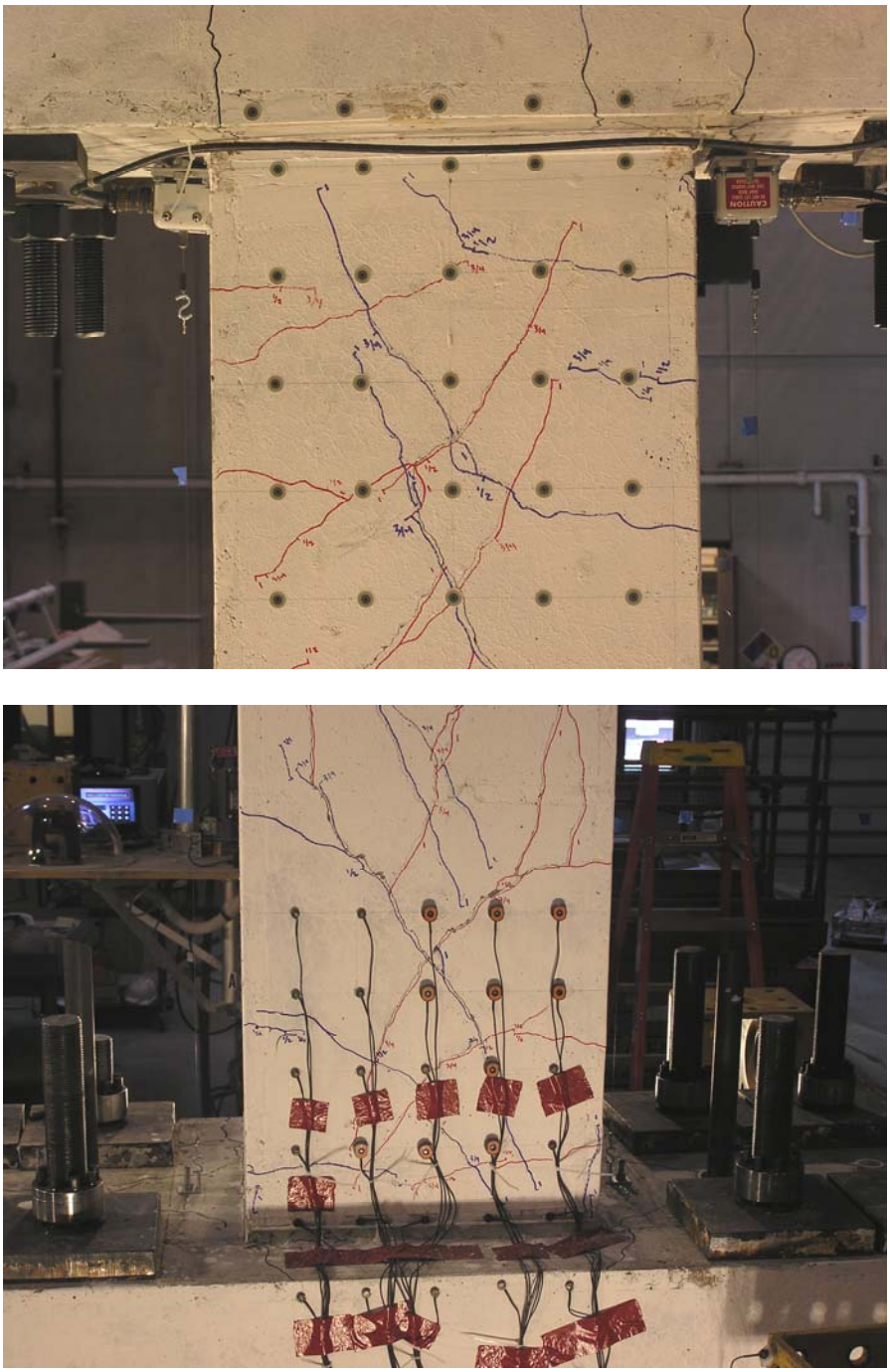

Figure 3.9: Specimen 2 crack pattern at a drift ratio of 1.00%

(a) Top column end, north face (b) Bottom column end, south face

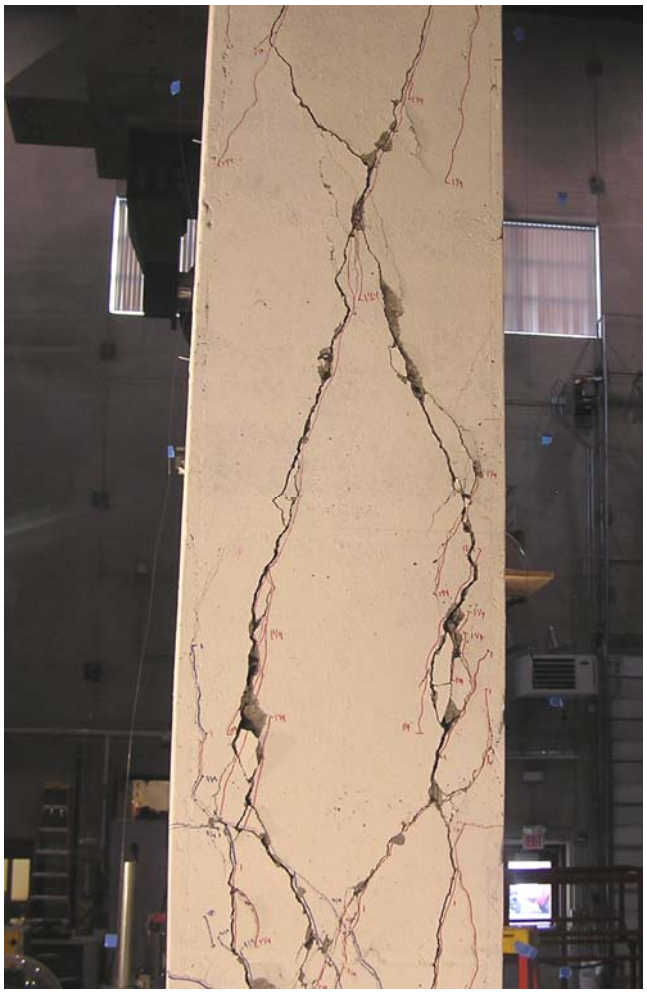

Figure 3.10: Specimen 2 crack pattern at a drift ratio of 1.25% (after axial failure)

(a) Center of column, north face

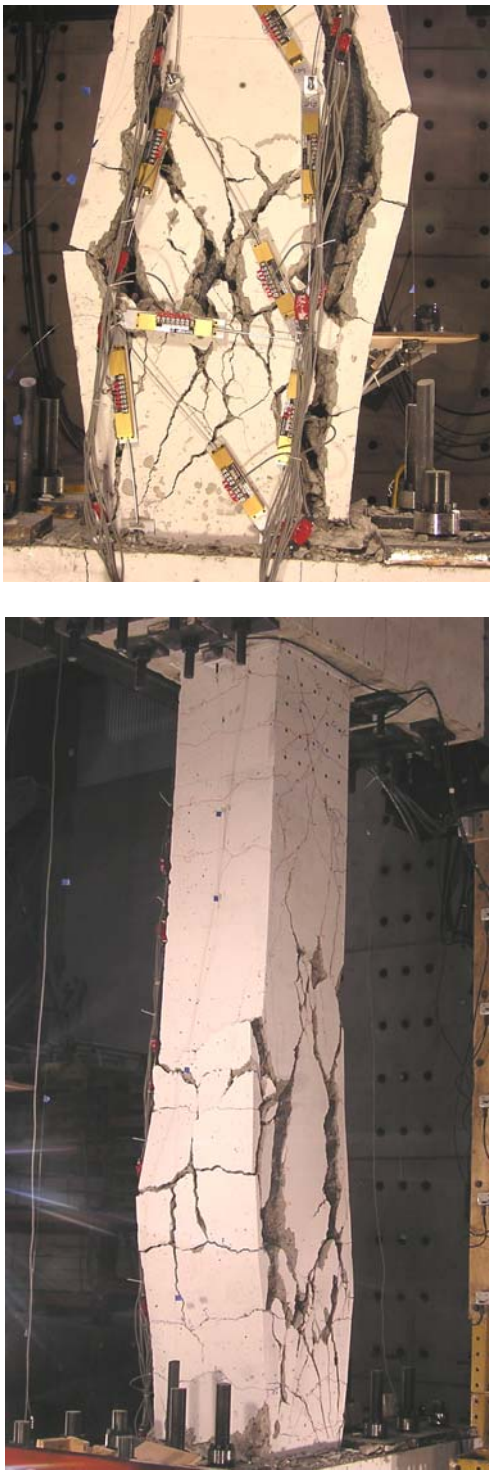

Figure 3.11: Specimen 2 condition at the end of the test

(a) Bottom column end, south face, (b) Full column, northeast corner

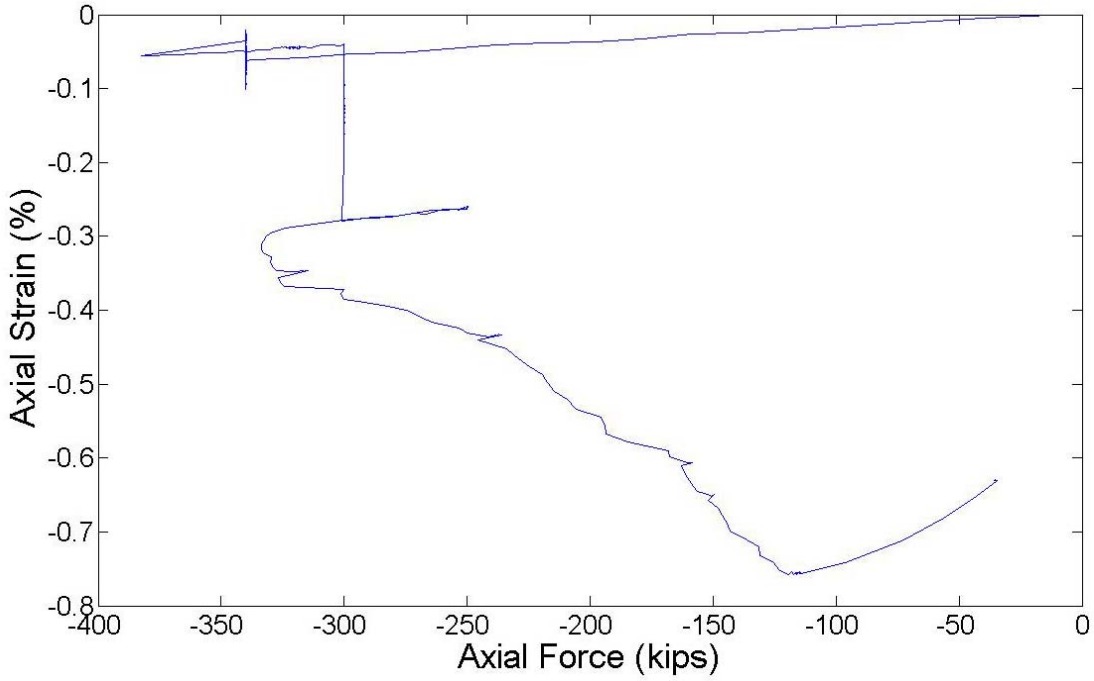

Figure 3.12 Axial strain-axial force response for Specimen 2

Table 3.2: Force and strain at axial failure for Specimen 2

Axial Failure Event	Axial Force	Lateral Force	Mean Axial Strain
1	-340 kips	70.6 kips	-0.035%
2	-300 kips	1.6 kips	-0.20%

3.4 Load-Deflection Response

The lateral load-lateral drift response for each specimen is shown in Figure 3.13. Both graphs show minor reductions in strength due to repeated cycling at each drift level. These hysteretic responses indicate that the behavior of both specimens was very brittle in nature. Specimen 1 maintained axial and lateral load carrying capacity up to a peak lateral load of 92.7 kips, and a lateral drift ratio of 1.00% prior to initial axial failure. After failure, lateral load resistance was reduced to effectively zero. Specimen 2 reached a peak lateral load and drift ratio of 81.5 kips and 1.25%, respectively, prior to initial axial failure, after which lateral load resistance dropped approximately 55% and continued to diminish until the end of the test.

Given the identical characteristics and applied lateral displacement protocol for the two specimens, the difference in specimen response indicates that column performance was significantly influenced by the magnitude of the applied axial load. Specimen 1, which had the higher axial load, failed at a smaller lateral displacement than Specimen 2. This is consistent with the relationship between axial load and lateral displacement at axial failure previously documented in literature. In addition, Specimen 1 experienced axial failure at a higher lateral load. This is also consistent with the documented relationship between axial load and the resulting lateral strength and stiffness.

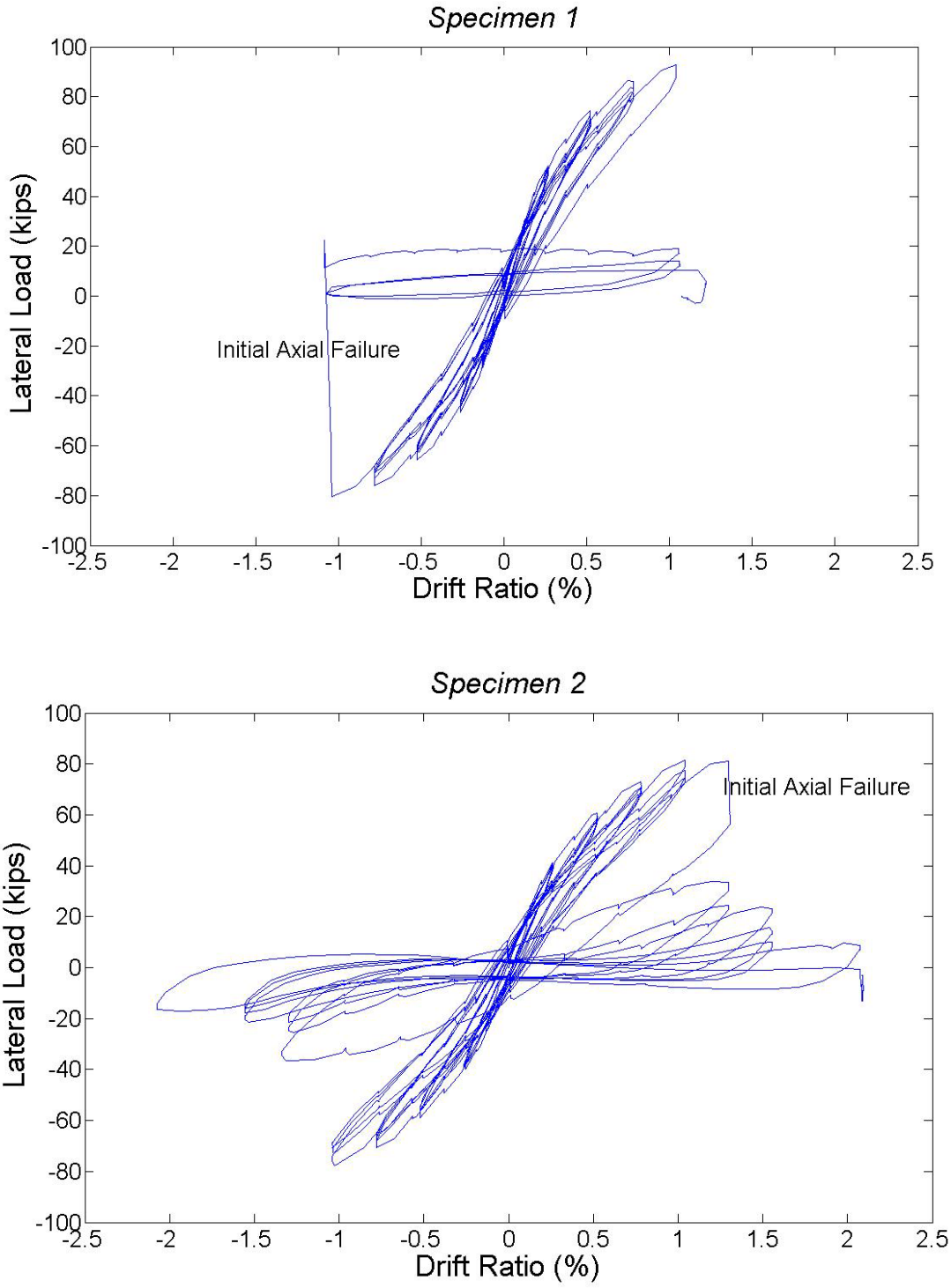

Figure 3.13: Lateral load-lateral drift responses. (a) Specimen 1, (b) Specimen 2

The behavior of the two specimens at and past the point of axial failure was also directly related to the difference in axial load. The failure of Specimen 1 was very brittle, characterized by the sudden widening of an existing shear crack located in the maximum moment region at the bottom of the specimen. Following initial axial failure, the axial load carrying capacity dropped by 63% and nearly all residual lateral load capacity was lost. The applied axial load was subsequently reduced to 100 kips and the lateral displacement protocol was resumed. The specimen was only able to carry the reduced axial load up to the first peak of the next series of displacement cycles, with a maximum lateral drift ratio of 1.25%. In Specimen 2, failure resulted after the formation of two previously unobserved shear cracks across the middle section of the column. As these cracks widened, column hoop 5 lost anchorage, triggering axial failure of the longitudinal reinforcement. The initial failure of Specimen 2 resulted in a reduction of only 6.5% of the axial load carrying capacity and approximately 55% of the lateral load resistance. After initial failure, cycling resumed at a reduced axial load of 300 kips and the specimen was able to sustain the reduced axial load for several additional sets of displacement cycles, up to a maximum lateral drift ratio of 2.00%. The post-failure behavior of the two specimens indicates that a higher axial load results in a more rapid degradation of both axial and lateral load carrying capacity, as well a reduction in the residual drift capacity.

These relationships are further illustrated by examining the relationship between mean axial strain and lateral drift for each of the specimens, as illustrated in

Figure 3.14. Increases in the mean axial strain for Specimens 1 and 2 following initial axial failure were 215% and 26%, respectively. In addition, Figure 3.14 shows that Specimen 2 was able to sustain the reduced axial load for a greater number of cycles, and the increase in axial strain corresponding to each cycle was much smaller than for Specimen 1.

Consideration should be given to the axial re-loading of Specimen 1 after initial axial failure. This process ensured that the specimen was unable to sustain the original axial load before the lateral displacement protocol was resumed under a reduced axial load. This same process was not followed for Specimen 2, and may have influenced the post-failure behavior of the second specimen. Upon resuming the lateral displacement protocol, Specimen 1 had been subjected to two axial failure events, while Specimen 2 had been subjected to only one. The additional damage may have influenced the residual stiffness and load capacity of Specimen 1, although as discussed, the relative behavior of the two specimens is consistent with the expected behavior.

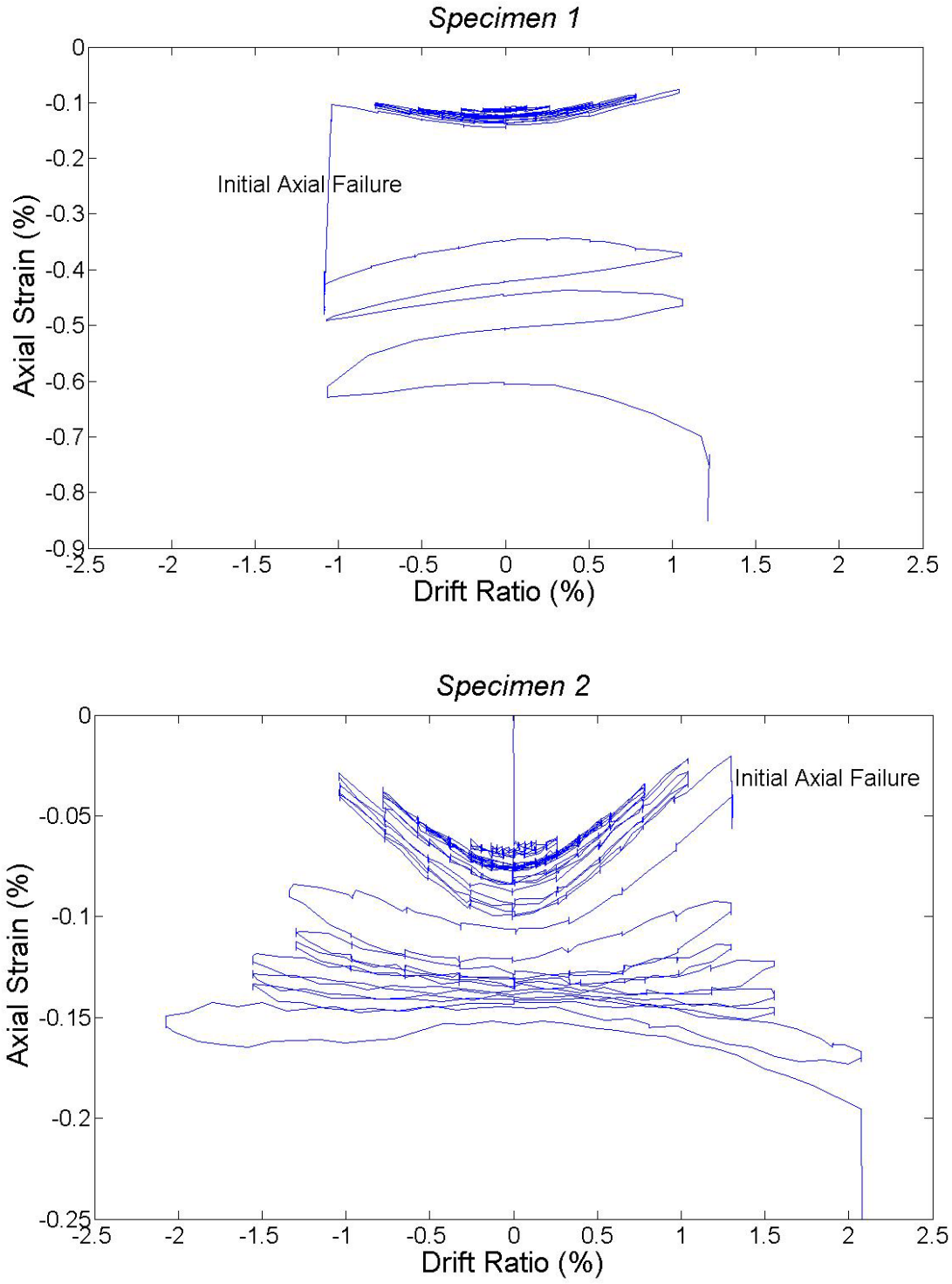

Figure 3.14: Axial strain-lateral drift responses. (a) Specimen 1, (b) Specimen 2

3.5 Moment-Curvature Analysis

The theoretical moment-curvature response of each specimen was calculated under the assumptions that plane sections remain plane, and strain is distributed linearly throughout the column cross-section. The stress in each layer of the cross-section was calculated using the strain at the centroid of the layer. Concrete stress f_c was calculated using the stress-strain relationship developed by Hognestad (1951), given by Eq. (3.1) through (3.3). Concrete was assumed to carry no tensile force.

$$f_c = \begin{cases} f_c'' \left[\dfrac{2\varepsilon_c}{\varepsilon_o} - \left(\dfrac{\varepsilon_c}{\varepsilon_o} \right)^2 \right] & for \quad \varepsilon_c \le \varepsilon_o \\ f_c'' \left[1 - 0.15 \left(\dfrac{\varepsilon_c - \varepsilon_o}{\varepsilon_u - \varepsilon_o} \right) \right] & for \quad \varepsilon_c > \varepsilon_o \end{cases} \tag{3.1}$$

$$f_c'' = 0.85 f_c' \tag{3.2}$$

$$\varepsilon_o = \frac{1.7 f_c'}{E_c} \tag{3.3}$$

Where:

f_c = concrete stress (ksi)

f_c'' = peak concrete stress (ksi)

f_c' = concrete compressive strength (ksi)

ε_c = concrete strain

ε_o = concrete strain at peak stress

ε_u = ultimate concrete strain = 0.0038

E_c = concrete modulus of elasticity (ksi)

Stress in the reinforcing steel f_s was calculated based on an elasto-plastic idealization of the measured stress-strain relationship of the longitudinal reinforcement, as given in Eq. (3.4).

$$f_s = \begin{cases} 29000\varepsilon_s & for \quad \varepsilon_s \le 0.0022 \\ 64 & for \quad \varepsilon_s > 0.0022 \end{cases} \tag{3.4}$$

Where:

f_s = reinforcing steel stress (ksi)

ε_s = reinforcing steel strain

Solutions were obtained by choosing the position of the neutral axis and the extreme concrete compressive strain, and then iterating until equilibrium was achieved for the internal forces. This analysis included the effects of axial load. The concrete compressive strain was incremented and the process was repeated to obtain the full moment-curvature relationship for each specimen. The moment and curvature at yielding of the tensile reinforcement was also calculated based on a cracked section analysis. Figure 3.15 plots the theoretical moment-curvature responses in green, the measured moment-curvature responses up to initial axial failure in blue, and the curvature at yielding of the longitudinal reinforcement in red. The measured responses indicate that both specimens were very close to yield at initial axial failure.

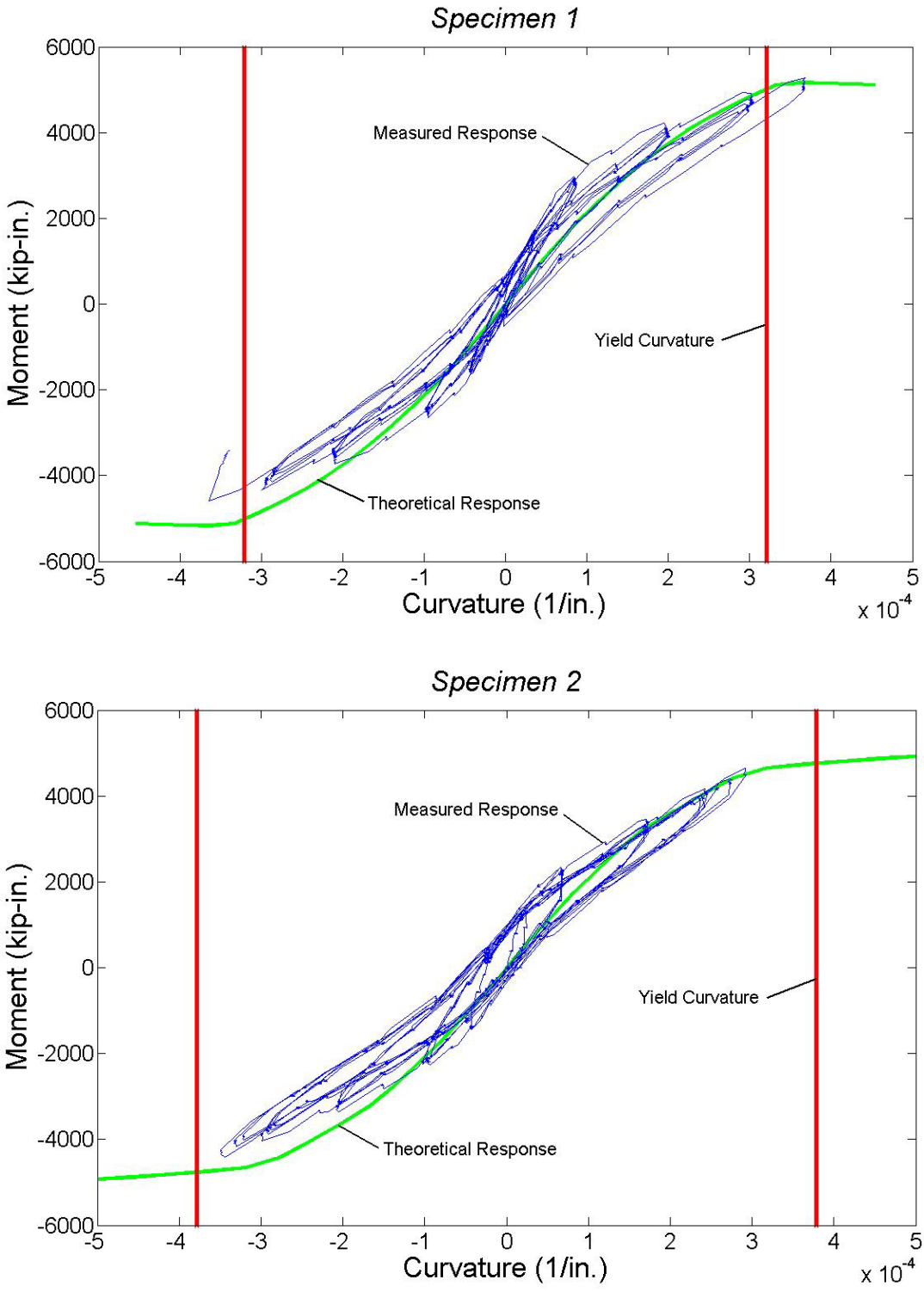

Figure 3.15: Moment-curvature responses. (a) Specimen 1, (b) Specimen 2

Moment and curvature values are reported under the assumption of equivalent section properties at all locations along the column. No modifications or allowances were made for column damage, and thus moment redistribution, due to cyclic loading. This was considered an appropriate assumption, as is evidenced by the close agreement between theoretical and measured responses.

Curvature profiles for the specimens up to initial axial failure are shown in Figure 3.16. The vertical red lines in each graph represent the curvature at yield, while the horizontal black lines represent the mid-height of the column. Both Figures 3.15 and 3.16 indicate that Specimen 1 reached yield curvature during the final cycle prior to initial axial failure. According to the moment-curvature analysis, Specimen 2 did not reach yield prior to axial failure.

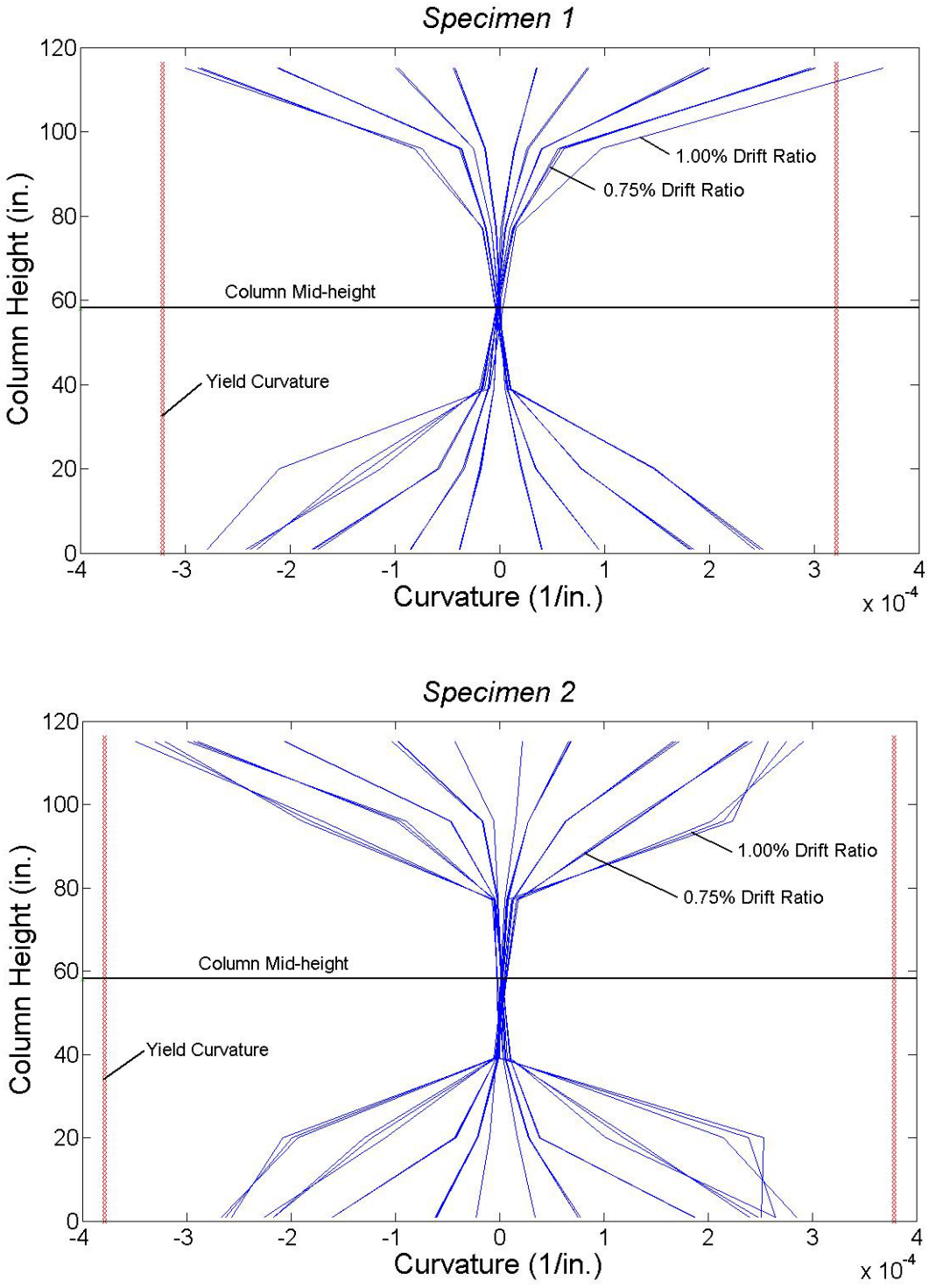

Figure 3.16: Curvature profiles. (a) Specimen 1, (b) Specimen 2

3.6 Deflection Components

Deflection profiles for displacement cycles prior to axial failure, created from the horizontal string potentiometer data are shown in Figure 3.17. Both plots illustrate the anticipated double curvature deflected shape typical of a fixed-fixed column subjected to lateral loading. The interior green vertical lines on the graphs correspond to theoretical values of deflection at the top of the column at first cracking, while the exterior red vertical lines represent the theoretical deflection at the top of the column at first yield of the longitudinal reinforcement. The calculated cracking and yield deflections are 0.07 in. and 1.17 in., respectively, for Specimen 1, and 0.09 in. and 1.29 in. for Specimen 2.

The theoretical cracking and yield deflections were determined by adding components due to flexure, shear, and bar slip. The flexure component was calculated using a moment-curvature analysis along with the moment-area method for calculating deflections. To simplify the analysis, the moment-curvature relationship was assumed to be linear up to the yield point. Thus, the flexure deflection $\Delta_{Flexure}$ was calculated as shown in Eq. (3.5).

$$\Delta_{Flexure} = \frac{\varphi * L^2}{6} \tag{3.5}$$

Where:

φ = maximum curvature in the column (in.$^{-1}$)

L = height of column (in.)

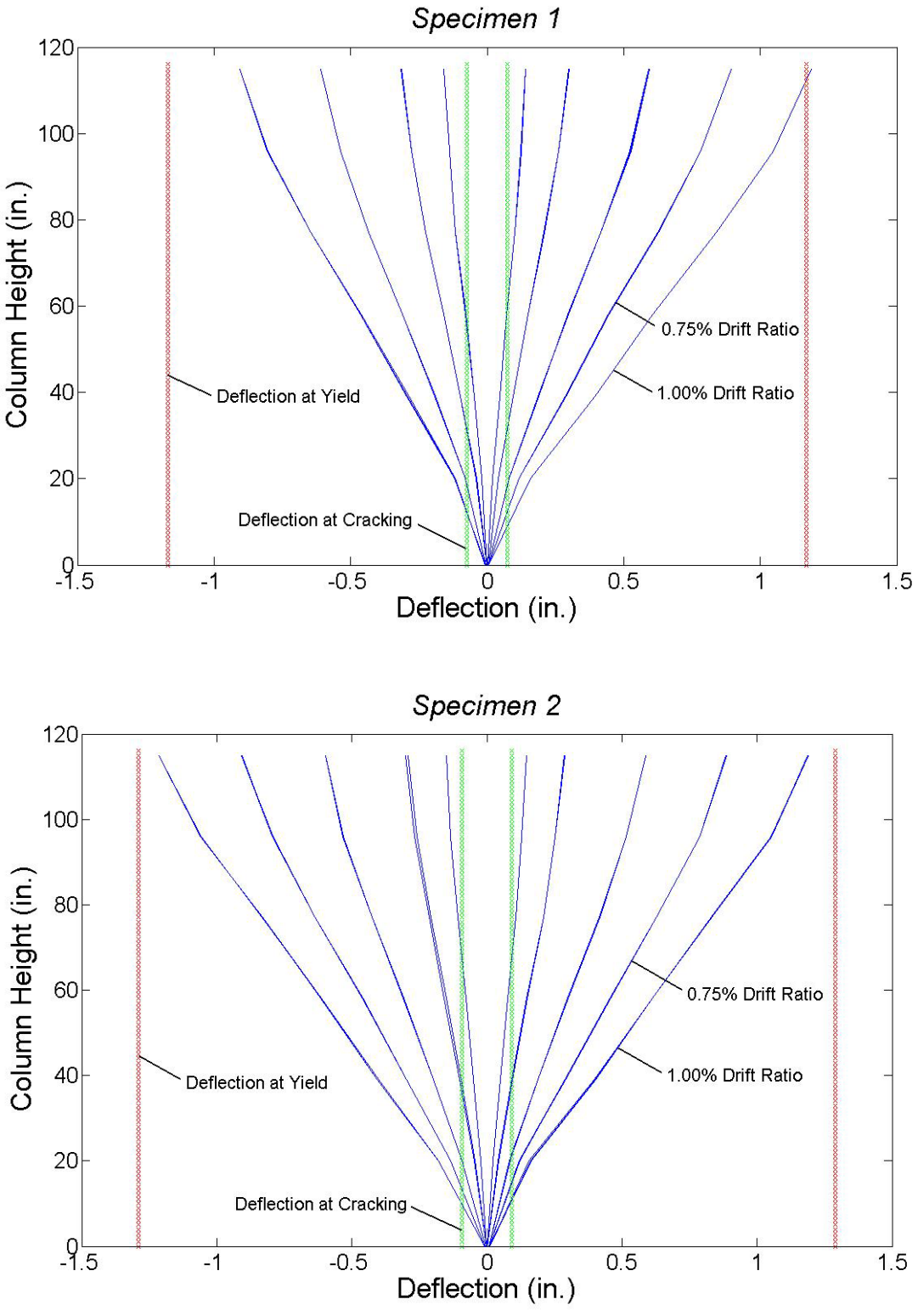

Figure 3.17: Deflection profiles. (a) Specimen 1, (b) Specimen 2

Shear deflection was calculated under the assumption of uniform shear strain along the length of the column and linear-elastic material properties. The shear component of deflection Δ_{Shear} was determined using Eq. (3.6) through (3.8).

$$\Delta_{Shear} = \frac{6}{5}\frac{V}{GA_g}L \tag{3.6}$$

$$V = \frac{2M}{L} \tag{3.7}$$

$$G = \frac{E_c}{2(1+\nu)} \tag{3.8}$$

Where:

V = shear force (kips)

G = concrete shear modulus (ksi)

A_g = cross-sectional area of the column (in^2)

M = moment at column ends (kip-in.)

E_c = concrete modulus of elasticity (ksi)

ν = Poisson's ratio = 0.20

The third component of deflection results from slip due to the extension of the longitudinal reinforcement at the ends of the column, as well as slip from the anchorage of the concrete. The slip deflection Δ_{Slip} was calculated according to Eq. (3.9), in which a uniform bond stress was assumed along the development length of the bar within the beam (Matamoros 1999).

$$\Delta_{Slip} = \frac{L d_b f_s^2}{(d - d') * 48 E_s \sqrt{f_c'}} \tag{3.9}$$

Where:

d_b = diameter of the longitudinal bars (in.)

f_s = reinforcing steel stress (ksi)

d' = depth to the first layer of reinforcement (in.)

d = depth to the third layer of reinforcement (in.)

E_s = reinforcing steel modulus of elasticity (ksi)

f_c' = concrete compressive strength (ksi)

The column experiences additional deflection due to rigid body rotation and horizontal slip at the base. These components were deemed to have a negligible effect on the overall deflection at the top of the column and were therefore not included in the theoretical deflection calculations. Table 3.3 lists the calculated deflection components at the top of the column at yielding of the longitudinal reinforcement for both tests.

Table 3.3: Theoretical deflection components at yield

	Specimen 1	**Specimen 2**
Flexure Deflection	0.72 in.	0.85 in.
Shear Deflection	0.02 in.	0.02 in.
Slip Deflection	0.43 in.	0.42 in.
Total Deflection	1.17 in.	1.29 in.

Comparison of the measured to theoretical deflection at yielding of the reinforcement in Figure 3.17 indicates that both specimens were very close to yielding at initial axial failure. According to the analysis of deflection behavior, Specimen 1 reached yield during the final cycle prior to axial failure, while Specimen 2 appears to have been very close to reaching yield before failure.

In order to more closely examine the relative contributions of the various deflection components throughout the tests, the measured data obtained using the Krypton system was analyzed. Deflection components were determined using the method presented by Matamoros (1999). Figure 3.18 shows the breakdown of the deflection components within the 5 x 5 LED array that was monitored by the Krypton system. The deflection values correspond to a point at the top of the grid, located 17 in. up from the base of the column. Tables 3.4 and 3.5 list the graphically-interpreted deflection components at peak displacement values for Specimens 1 and 2, respectively. The large contribution due to slip and rigid body deflection is a result of the LED array being located at the bottom of the column. In this region of the column, deformations are extremely small and as a result, slip and rigid body deflection account for a greater portion of the total deflection.

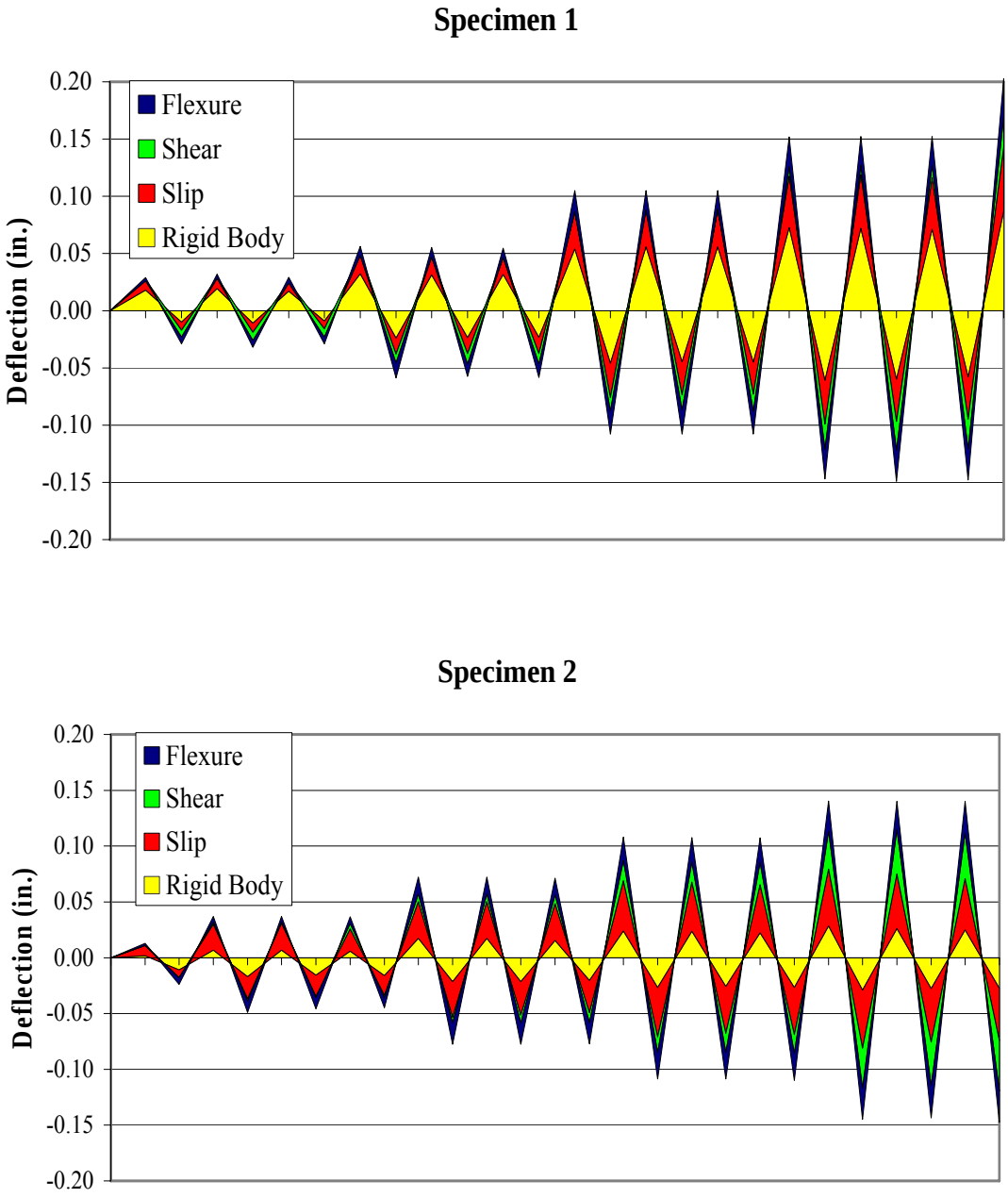

Figure 3.18: Deflection components. (a) Specimen 1, (b) Specimen 2

Table 3.4: Specimen 1 deflection components from Krypton system

Cycle Number	Drift Ratio	Rigid Body Displacement At Base (in.)	Rigid Body Rotation At Base (rad.)	Deflection Components at Top of Grid (in.)				
				Rigid Body	Slip	Shear	Flexure	Total
1	0.125%	0.017	0.00006	0.018	0.009	-0.001	0.003	0.029
2	-0.125%	-0.009	-0.00006	-0.010	-0.007	-0.006	-0.006	-0.029
3	0.125%	0.018	0.00007	0.019	0.010	-0.001	0.004	0.032
4	-0.125%	-0.010	-0.00006	-0.011	-0.008	-0.007	-0.006	-0.032
5	0.125%	0.016	0.00007	0.017	0.008	-0.001	0.005	0.029
6	-0.125%	-0.008	-0.00006	-0.009	-0.007	-0.007	-0.006	-0.029
7	0.25%	0.030	0.00014	0.032	0.017	-0.001	0.008	0.056
8	-0.25%	-0.022	-0.00011	-0.024	-0.014	-0.008	-0.013	-0.059
9	0.25%	0.029	0.00014	0.031	0.016	0.000	0.008	0.055
10	-0.25%	-0.022	-0.00010	-0.024	-0.014	-0.009	-0.011	-0.058
11	0.25%	0.029	0.00016	0.032	0.015	0.000	0.008	0.055
12	-0.25%	-0.022	-0.00009	-0.023	-0.014	-0.009	-0.012	-0.058
13	0.50%	0.051	0.00019	0.054	0.032	0.001	0.018	0.105
14	-0.50%	-0.043	-0.00018	-0.046	-0.030	-0.012	-0.020	-0.108
15	0.50%	0.053	0.00019	0.056	0.033	-0.001	0.017	0.105
16	-0.50%	-0.042	-0.00017	-0.045	-0.029	-0.013	-0.021	-0.108
17	0.50%	0.053	0.00018	0.056	0.032	0.001	0.016	0.105
18	-0.50%	-0.042	-0.00018	-0.045	-0.028	-0.015	-0.020	-0.108
19	0.75%	0.070	0.00017	0.073	0.045	0.008	0.026	0.152
20	-0.75%	-0.057	-0.00025	-0.061	-0.038	-0.022	-0.026	-0.147
21	0.75%	0.070	0.00013	0.072	0.047	0.008	0.025	0.152
22	-0.75%	-0.056	-0.00025	-0.060	-0.037	-0.025	-0.027	-0.149
23	0.75%	0.069	0.00013	0.071	0.045	0.011	0.025	0.152
24	-0.75%	-0.054	-0.00024	-0.058	-0.037	-0.026	-0.027	-0.148
25	1.00%	0.085	0.00013	0.087	0.056	0.027	0.033	0.203

Table 3.5: Specimen 2 deflection components from Krypton system

Cycle Number	Drift Ratio	Rigid Body Displacement At Base (in.)	Rigid Body Rotation At Base (rad.)	Deflection Components at Top of Grid (in.)				
				Rigid Body	Slip	Shear	Flexure	Total
1	0.125%	0.001	0.00005	0.002	0.009	0.000	0.002	0.013
2	-0.125%	-0.010	-0.00005	-0.011	-0.007	0.000	-0.006	-0.024
3	0.25%	0.005	0.00012	0.007	0.023	0.002	0.005	0.037
4	-0.25%	-0.015	-0.00012	-0.017	-0.02	-0.002	-0.010	-0.049
5	0.25%	0.005	0.00012	0.007	0.024	0.001	0.005	0.037
6	-0.25%	-0.014	-0.00011	-0.016	-0.019	-0.001	-0.010	-0.046
7	0.25%	0.004	0.00011	0.006	0.02	0.005	0.006	0.037
8	-0.25%	-0.014	-0.00012	-0.016	-0.018	-0.002	-0.009	-0.045
9	0.50%	0.013	0.00026	0.017	0.033	0.007	0.015	0.072
10	-0.50%	-0.018	-0.00022	-0.022	-0.032	-0.005	-0.019	-0.078
11	0.50%	0.013	0.00026	0.017	0.033	0.007	0.015	0.072
12	-0.50%	-0.018	-0.00022	-0.022	-0.03	-0.007	-0.019	-0.078
13	0.50%	0.011	0.00027	0.015	0.033	0.008	0.015	0.071
14	-0.50%	-0.017	-0.00021	-0.020	-0.029	-0.009	-0.019	-0.077
15	0.75%	0.018	0.00037	0.024	0.045	0.018	0.021	0.108
16	-0.75%	-0.022	-0.00030	-0.027	-0.044	-0.014	-0.024	-0.109
17	0.75%	0.018	0.00036	0.024	0.044	0.018	0.022	0.108
18	-0.75%	-0.021	-0.00030	-0.026	-0.042	-0.017	-0.024	-0.109
19	0.75%	0.017	0.00034	0.022	0.043	0.020	0.022	0.107
20	-0.75%	-0.022	-0.00031	-0.027	-0.042	-0.017	-0.024	-0.110
21	1.00%	0.022	0.00040	0.028	0.051	0.034	0.027	0.140
22	-1.00%	-0.023	-0.00037	-0.029	-0.052	-0.036	-0.028	0.145
23	1.00%	0.020	0.00038	0.026	0.049	0.040	0.025	0.140
24	-1.00%	-0.022	-0.00035	-0.028	-0.048	-0.039	-0.029	0.144
25	1.00%	0.019	0.00037	0.025	0.046	0.041	0.028	0.140
26	-1.00%	-0.022	-0.00034	-0.027	-0.047	-0.045	-0.028	0.147

Figure 3.19 shows only the shear and flexure deflection components from the Krypton data for each test. Both specimens exhibited approximately linear increases in the flexure component with each successive displacement cycle. This behavior matches expectation, given the direct relationship between flexure deflection and curvature, which is assumed to increase linearly up to yield. The flexure component of deflection for both specimens reached a maximum of approximately 0.030 in. prior to axial failure.

The shear deflection for Specimen 1 during early displacement cycles was negligible. As cycling progressed, the shear component had an increasingly significant contribution to the overall deflection, with the total shear deflection being approximately equal to the flexure deflection at axial failure. Specimen 2 also showed a negligible contribution from shear deflection at the beginning of the test. At the negative displacement peak prior to axial failure, the shear deflection had increased to approximately 0.045 in., which is 50% greater than the flexure deflection. The larger shear deflection contribution in Specimen 2 may be attributed to the lower axial load, which allowed for more significant opening of the shear cracks in the LED array region.

The theoretical shear deflection at axial failure calculated using Eq. (3.6) through (3.8) for both specimens was approximately 0.0035 in., compared with measured values of 0.027 in. and 0.045 in. for the two tests, respectively. The large discrepancy between the measured and theoretical values of shear deflection is due to the assumption in the theoretical equations that the shear modulus remains constant.

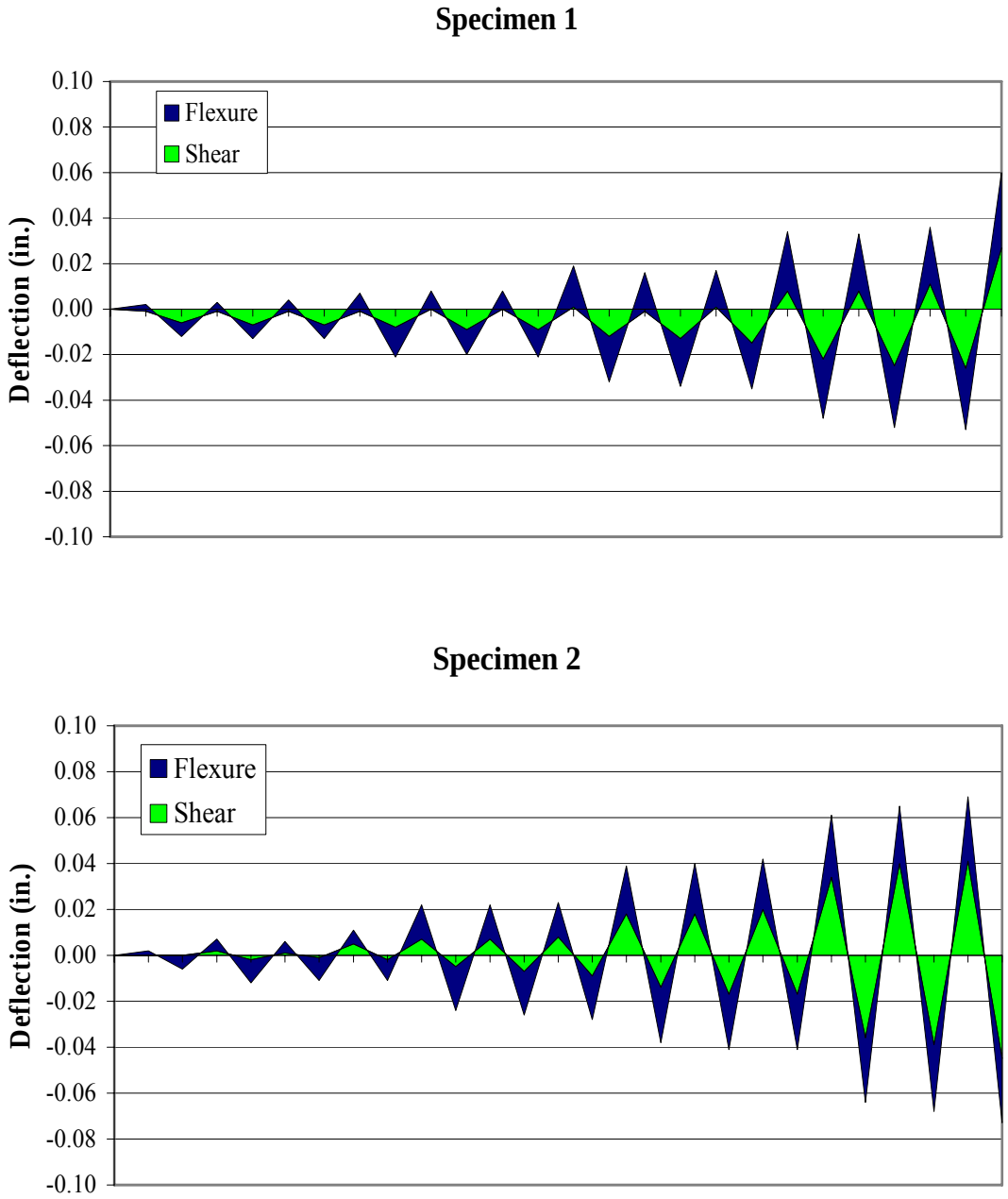

Figure 3.19: Flexure and shear deflection components. (a) Specimen 1, (b) Specimen 2

The theoretical values of the shear modulus calculated using Eq. (3.8) are 1571 ksi and 1504 ksi for Specimens 1 and 2, respectively. Repeated cycling and increased lateral deflection during testing likely cause softening of the column, which results in a decreasing shear modulus as the test progresses. Effective shear modulus values were calculated using the measured lateral load and shear deflection values at peak drift ratios and are presented in Figure 3.20. Using the effective shear moduli in Eq. (3.6) through (3.8), the theoretical shear deflection components at axial failure are 0.032 in. and 0.047 in. for Specimens 1 and 2, respectively. These values are much closer to those measured during testing.

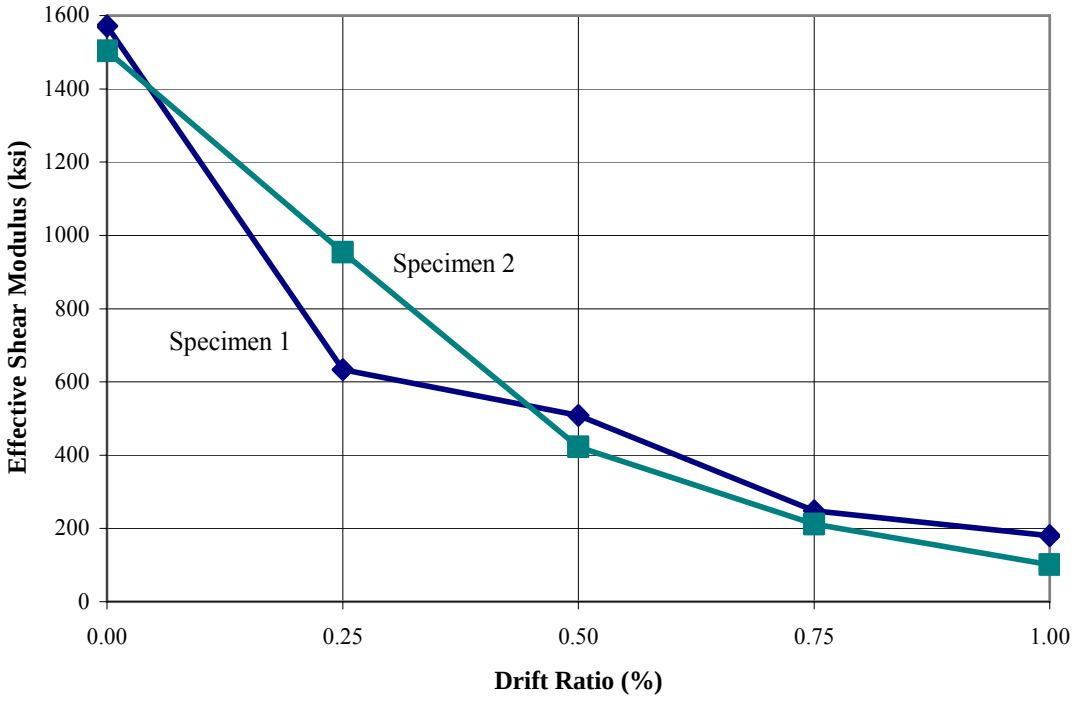

Figure 3.20: Effective shear modulus at increasing drift ratios

3.7 Measured Bar Strain Analysis

Strain gages were attached to the column reinforcing steel to monitor bar strain throughout the tests, in order to determine if and where yielding took place. Figures 2.24 and 2.25 in Section 2.7 give a detailed description of strain gage locations and labeling. For the remainder of this section, all discussion refers to the derived strain gage channels referenced in Section 2.7, which include the strain induced during axial loading, prior to beginning the lateral displacement protocol.

Figures 3.21 and 3.22 show the measured bar strain in the column longitudinal reinforcement at the top and bottom beam-column interfaces prior to initial axial failure for Specimens 1 and 2, respectively. The yield strain for the longitudinal reinforcement was determined to be 2210 micro-strain, based on the measured stress-strain relationship shown in Figure 2.13. Figure 3.21 indicates that the bar locations where gages LF3 and RM8 were attached did not reach yield, while measurements in gages RB3 and LF8 exceeded the yield strain. These data suggest that tensile yielding occurred only during positive displacement cycles. This correlates with the measured lateral force data, which was consistently greater during positive displacement cycles than negative ones. Since the some longitudinal bars reached yield at the beam-column interface while others did not, the measured bar strain data indicate that Specimen 1 was either at, or very close to yielding at the onset of initial axial failure.

Strain gage data at the beam-column interfaces for Specimen 2, shown in Figure 3.22, indicate that yielding did not occur in either gage LB3 or LB8. These

two gages recorded the highest strain values of all the gages located at the beam-column interfaces. Thus, the measured bar strain data indicates that yielding did not occur in Specimen 2 prior to axial failure.

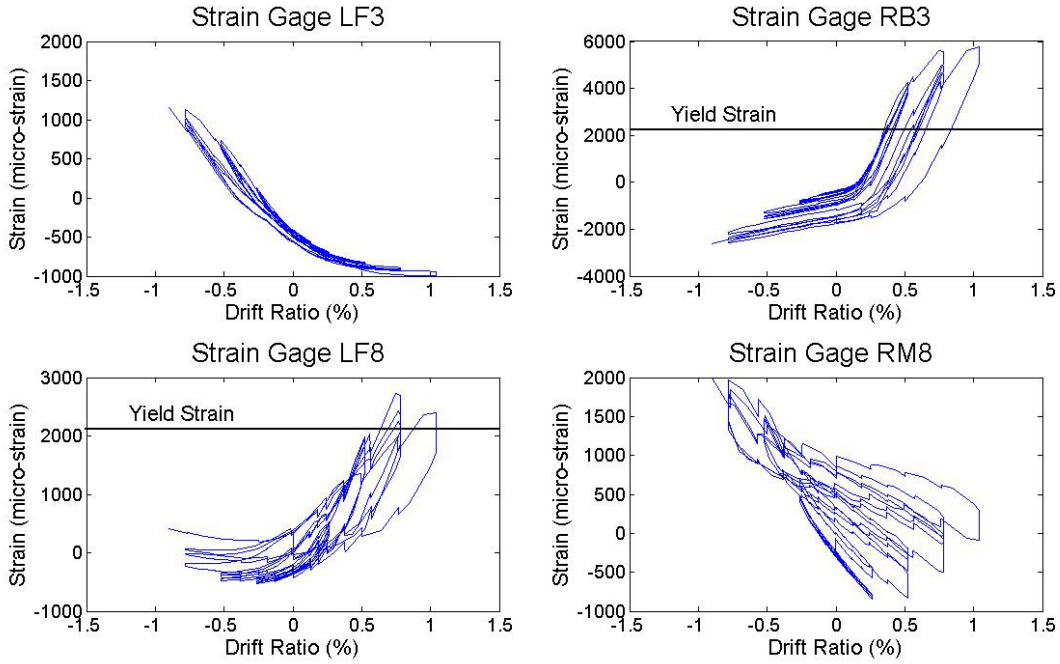

Figure 3.21: Measured bar strain in the longitudinal reinforcement at the beam-column interfaces for Specimen 1

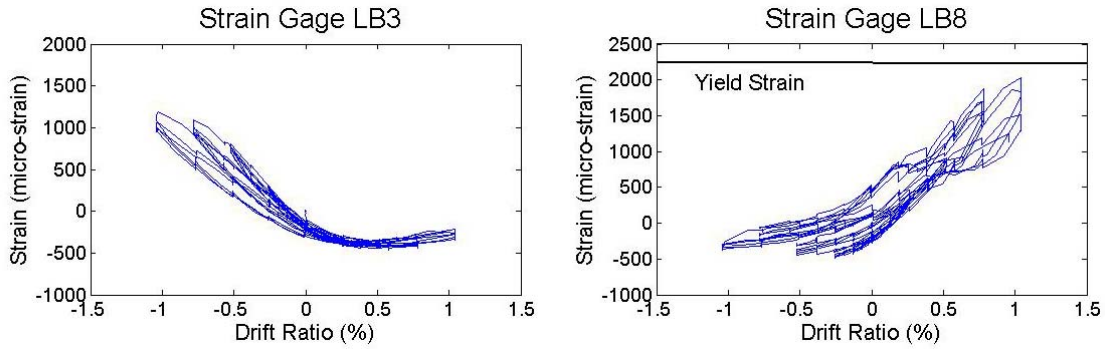

Figure 3.22: Measured bar strain in the longitudinal reinforcement at the beam-column interfaces for Specimen 2

Figures 3.23 and 3.24 plot the measured bar strain for representative strain gages attached to the transverse reinforcement for Specimens 1 and 2, respectively. The yield strain for the transverse reinforcement was determined to be 1860 micro-strain, based on the measured stress-strain relationship for the No. 3 bars, shown in Figure 2.14. Figure 3.23 indicates that measurements in strain gages H6LB, H6RB, and H5RB all exceeded the yield strain. Visual observations during testing correspond well with the measured bar strain data. All three of these gages were located in the bottom region of the column, which experienced the greatest amount of damage and shear cracking. The main shear crack that resulted in axial failure extended from Hoop 6 on the west column face up to Hoop 5 on the east face, stretching almost directly across strain gages H6LB and H5RB. In addition, strain gage H6LB was located closest to the 90º hook in Hoop 6 that opened up, allowing buckling of the longitudinal bars during axial failure.

As indicated in Figure 3.24, measurements in gages H6RB, H6LB, H5RF, and H5RB on Specimen 2 exceeded the yield strain. Similar to Specimen 1, the visual observations made during the test confirmed the measured data from these strain gages. All of these gages were located at the bottom of the column, which experienced the greatest amount of damage. Strain gage H5RF was located closest to the 90º hook in Hoop 5 that had an anchorage failure, allowing lateral deformation of the longitudinal bars and triggering axial failure. Gage H5RB was located in the region closest to the far northeast longitudinal bar that deformed outward during axial failure.

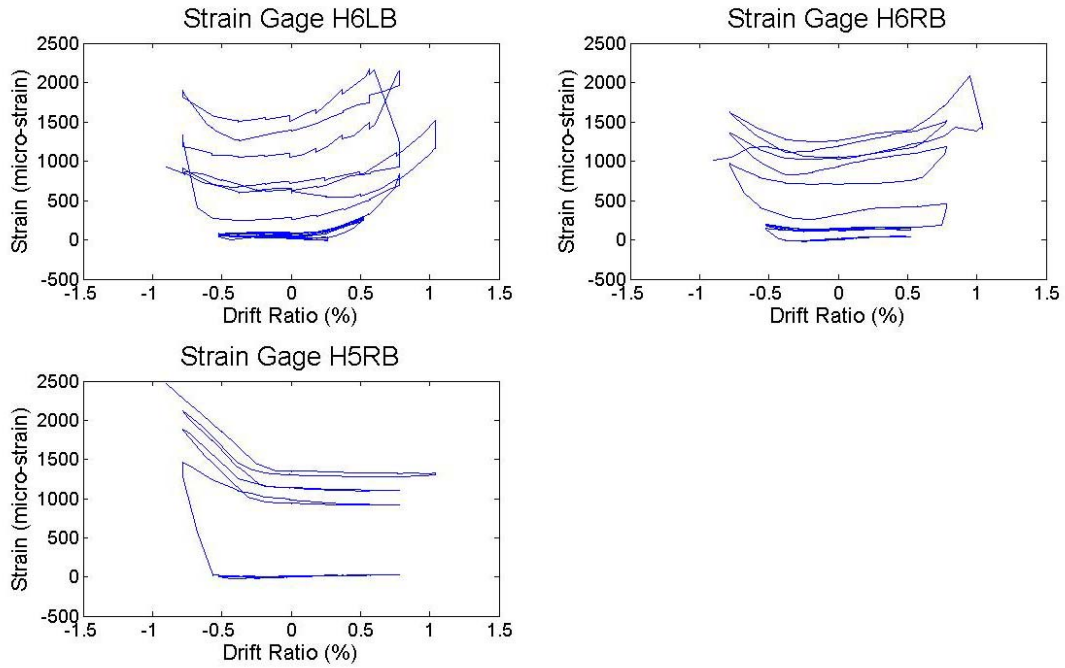

Figure 3.23: Measured bar strain in the transverse hoops for Specimen 1

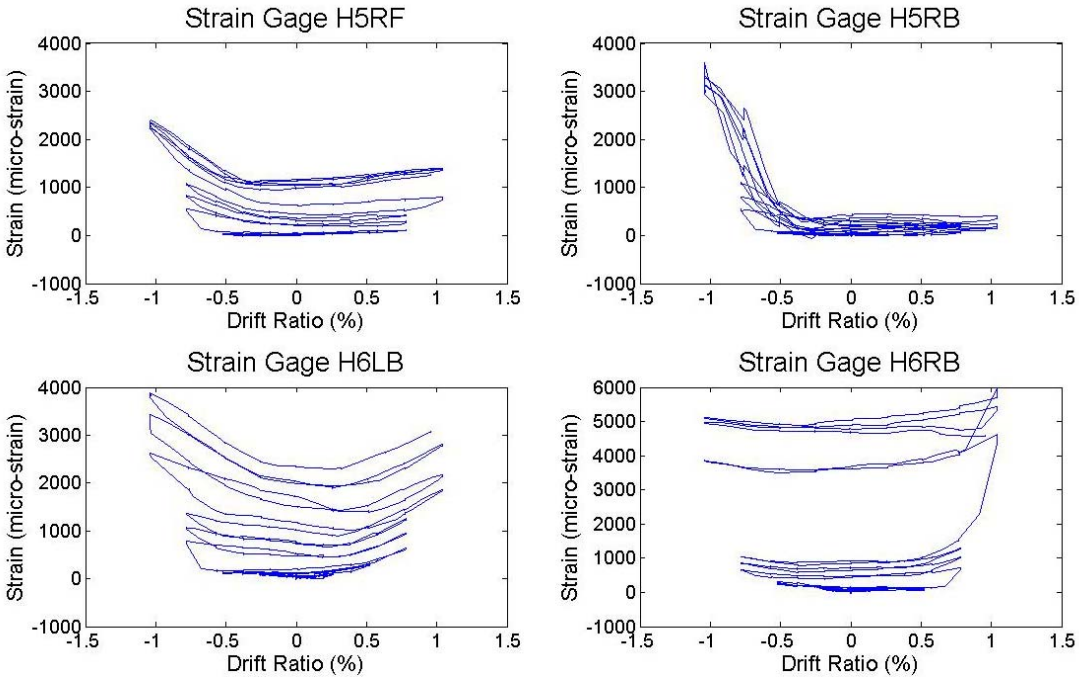

Figure 3.24: Measured bar strain in the transverse hoops for Specimen 2

3.8 Shear Strength

For each specimen, Table 3.6 presents the maximum measured shear during testing V_{test}, the nominal shear strength V_n calculated using Eq. (3.10) through (3.12) (ACI 318-08), and the shear force required to yield the longitudinal reinforcement V_p based on the moment-curvature analysis reported in Section 3.5.

$$V_c = 0.002\left(1+\frac{P}{2000A_g}\right)\sqrt{f_c'}bd \tag{3.10}$$

$$V_s = \frac{A_{st}f_{yt}d}{s} \tag{3.11}$$

$$V_n = V_c + V_s \tag{3.12}$$

Where:

V_c = shear force carried by the concrete (kips)

P = axial load (lb)

A_g = cross-sectional area of the column (in^2)

f_c' = concrete compressive strength (psi)

b = column width (in.)

d = depth to tension reinforcement (in.)

V_s = shear force carried by the transverse steel (kips)

A_{st} = area of the transverse reinforcement (in^2)

f_{yt} = yield stress of the transverse reinforcement (ksi)

s = spacing of the transverse reinforcement (in.)

Ratios of the calculated shear at yield to the nominal shear capacity were 1.10 and 1.18 for Specimens 1 and 2, respectively, indicating that both specimens were expected to fail in shear prior to yielding of the longitudinal reinforcement. Specimen 1 was expected to fail in shear closer to the yield point than Specimen 2. These theoretical expectations are consistent with the measured data presented earlier in this Chapter. The maximum measured shear values for each test were 92.7 kips and 81.5 kips, respectively. These values were both higher than those calculated using Eq. (3.10) through (3.12), with the ratio of V_n to V_{test} for both specimens being approximately 0.85.

Table 3.6: Nominal shear strength

Specimen	Axial Load (kips)	V_{test} (kips)	V_c (kips)	V_s (kips)	V_n (kips)	V_p (kips)	V_p / V_n
1	500	92.7	68.5	10.2	78.7	86.4	1.10
2	340	81.5	59.4	10.2	69.7	82.0	1.18

3.9 Comparison to Elwood-Moehle Axial Failure Model

The measured drift ratios at each axial failure event were compared with values calculated using the failure model developed by Elwood and Moehle (2003). This model is discussed in detail in Section 1.3.2. Table 3.7 lists the calculated lateral drift ratios at axial failure corresponding to each axial failure event during the two tests. The failure model yielded estimates for the drift ratio at the initial and reduced

axial load failures of 0.90% and 3.34%, respectively, for Specimen 1 and 1.27% and 1.42% for Specimen 2. Comparatively, the measured drift ratios at initial and reduced axial load failures for Specimen 1 were 1.00% and 1.21%, respectively, and 1.25% and 2.00% for Specimen 2. The relationship between drift ratio at axial failure and axial load calculated using the Elwood-Moehle model is plotted in Figure 3.25 along with the axial load and measured drift ratios at the initial and reduced axial load failure events for both specimens.

Table 3.7: Drift ratio at axial failure calculated using the Elwood-Moehle model

Specimen	Initial Axial Load (kips)	Drift Ratio (%)	Reduced Axial Load (kips)	Drift Ratio (%)
1	500	0.90	100	3.34
2	340	1.27	300	1.42

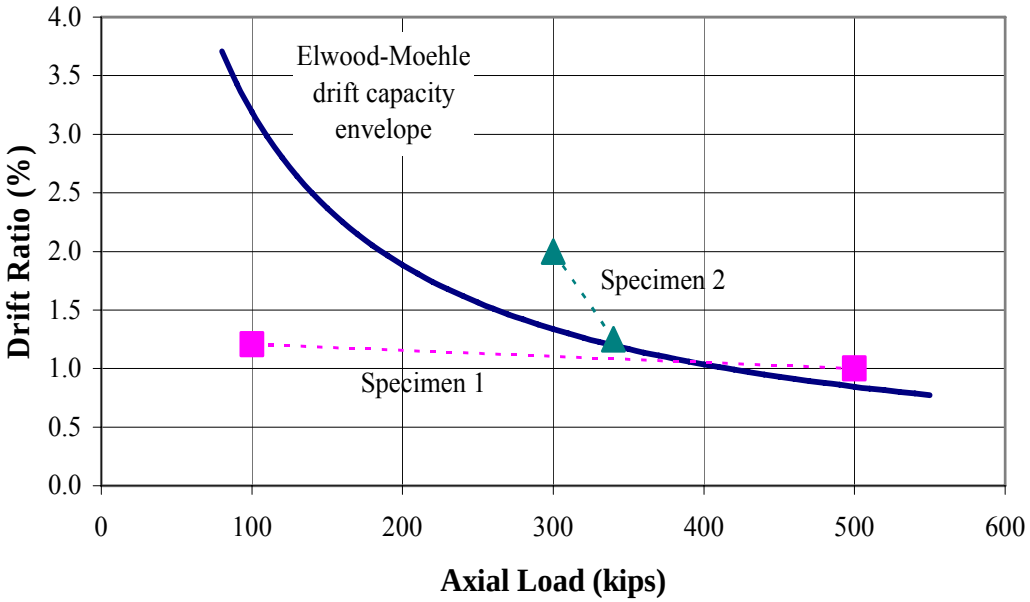

Figure 3.25: Measured and calculated drift ratios at axial failure.

As depicted in Figure 3.25, the drift ratios calculated using the Elwood-Moehle model matched actual drift ratios at axial failure very closely for the first axial failure event for both specimens. The estimates of drift ratio at the reduced axial load failure events were significantly less accurate. While the model underestimated the drift ratio at the reduced axial load failure of Specimen 2, it significantly overestimated the drift capacity at reduced axial load failure of Specimen 1. Some of the inaccuracy in the estimation of drift ratio at reduced axial load failure may be due to the inability of the Elwood-Moehle model to incorporate the effects of damage and resulting losses in stiffness sustained during the initial axial failures for both specimens. The amount of damage caused by the initial axial failure event for Specimen 1 was far greater than that for Specimen 2, which is clearly shown by the post-failure behavior of the two specimens. Additional research is necessary to determine the residual axial load-drift capacity relationship beyond initial axial failure.

3.10 Axial Capacity of Longitudinal Reinforcement

Reinforced concrete columns are assumed to distribute axial load throughout their cross-section, with a portion of the load being carried by the longitudinal steel P_s, and the remaining load carried by the concrete P_c. Based on observations from tests performed by Lynn (2001) and Sezen (2000), the ability of columns to sustain axial load after shear failure appears to be closely related to the portion of the load carried by the longitudinal reinforcement. When P_s reaches a critical value the

reinforcement will fail, resulting in axial failure of the column. The maximum axial capacity of the reinforcement may be limited by either the plastic or buckling capacity of the bars, depending on the magnitude of the applied load and the buckling characteristics of the longitudinal reinforcement.

Observations from tests performed by Lynn (2001) and Sezen (2000) indicate that columns with an applied axial load greater than the gross axial capacity of the bars $A_s f_y$ exhibit a mushroom-shaped deformation pattern, indicating a failure controlled by the buckling capacity of the longitudinal reinforcement $P_{s\text{-}buckle}$. The observed behavior differed in columns with an applied axial load less than $A_s f_y$, which tended to show an S-shaped deformation pattern in the longitudinal reinforcement. These findings suggest that the plastic capacity of the bars under combined bending and axial load $P_{s\text{-}plastic}$ controlled the behavior of the column.

The deformed shape of the longitudinal reinforcement for Specimen 1 suggests that a buckling failure occurred, as can be observed in Figure 3.5. The deformed shape for Specimen 2, shown in Figure 3.11, indicates that the column axial capacity was limited by the plastic capacity of the reinforcing bars $P_{s\text{-}plastic}$. These visual failure classifications match the observations from the Lynn and Sezen tests relating the failure mode to the axial load level. The 500-kip axial load applied to Specimen 1 was very close to the gross axial capacity of the longitudinal bars $A_s f_y$, at which buckling is expected to control axial capacity. The 340-kip axial load applied to Specimen 2 was significantly lower than $A_s f_y$, and was thus expected to fail due to the plastic capacity of the longitudinal bars $P_{s\text{-}plastic}$.

Elwood (2003) proposed Eq. (3.13) and (3.14) to determine the maximum axial capacity of the longitudinal reinforcement $P_{s\text{-}max}$.

$$P_{s-\max} = A_s f_y \left(\frac{d_b / L}{0.75\pi \frac{\Delta}{L} + \frac{d_b}{L}} \right) \qquad \text{if } P < A_s f_y \qquad (3.13)$$

$$P_{s-\max} = A_s f_y \left(\frac{d_b / L}{0.75\pi \frac{\Delta}{L} + \frac{d_b}{L}} \right) < \frac{\pi^2 E_t I_{bar} n_{bars}}{\left(L_{eff}\right)^2} \qquad \text{if } P \geq A_s f_y \qquad (3.14)$$

Where:

$A_s f_y$ = gross axial capacity of the longitudinal bars (kips)

d_b = diameter of the longitudinal bars (in.)

L = height of column (in.)

Δ = column displacement at axial failure (in.)

E_t = reinforcing steel tangent modulus (ksi)

I_{bar} = moment of inertia of a longitudinal bar (in^4)

n_{bars} = number of longitudinal bars

L_{eff} = effective buckling length of the longitudinal bars (in.)

P = total axial load (kips)

$P_{s\text{-}max}$ = maximum axial capacity of the longitudinal bars (kips)

Calculation of the limiting buckling load $P_{s\text{-}buckle}$ in Eq. (3.14) requires the determination of both the effective buckling length L_{eff}, and the tangent modulus E_t. Based on observations from previous tests, Elwood suggested that the effective buckling length be assumed to be approximately 0.80*s*, which is between a fixed-fixed and a pinned-pinned condition at the column hoops. The tangent modulus can be graphically estimated from tensile coupon tests of the reinforcing bars. Elwood suggested adopting a value for the tangent modulus of 7% of the elastic modulus, which he considered representative of the properties of reinforcing bars.

In this study, ASTM A706 reinforcing steel was used, which had a post-yield modulus of effectively zero up to a strain of 1.0%, as shown in Figure 2.13. As a result, the tangent modulus could not accurately be calculated from the measured stress-strain curve for the reinforcement. Since direct calculation of the tangent modulus was not possible, bounding estimates of E_t were established based on two behavioral extremes, given the observed buckling failure behavior of Specimen 1. The lower-bound value was determined using a transformed-section analysis and a concentrically applied axial load of 500 kips. This yielded a load of 81 kips carried by the longitudinal reinforcement, or 16% of the total axial load. Using this as the minimum possible buckling load in the upper limit of Eq. (3.14) and solving for the tangent modulus, yields a value that is 9% of the elastic modulus. The upper-bound tangent modulus was calculated by assuming that the maximum value for the upper limit of Eq. (3.14) was the plastic capacity of the reinforcing bars, given that buckling was the observed failure mode. Solving for the plastic capacity yielded a maximum

load of 150 kips, or 30% of the total axial load carried by the longitudinal reinforcement. Solving for the tangent modulus in Eq. (3.14) gave a value that is 17% of the elastic modulus. Specimen 2 was assumed to have failed as a result of the plastic capacity of the longitudinal reinforcement and thus $P_{s\text{-}max}$ was calculated using Eq. (3.13). This yielded a load of 127 kips in the longitudinal reinforcement at axial failure, or 37% of the total axial load. Table 3.8 summarizes the axial capacity data for the longitudinal bars based on Eq. (3.13) and (3.14).

Table 3.8: Axial capacity of the longitudinal bars for Specimens 1 and 2

Specimen	**Plastic Axial Capacity, $P_{s\text{-}plastic}$**	**Buckling Capacity, $P_{s\text{-}buckle}$**		
		Elwood $E_t = 0.07\ E_s$	**Lower-Bound $E_t = 0.09\ E_s$**	**Upper-Bound $E_t = 0.17\ E_s$**
1	150 kips	61 kips	81 kips	150 kips
2	127 kips	61 kips	81 kips	150 kips

Combining the Specimen 1 and 2 results with those from tests performed by Lynn (2001) and Sezen (2000) provides a database with which to evaluate axial failure behavior. The axial capacity data for all 14 columns tested is listed in Table 3.9. Only one column of those tested by Lynn and Sezen, Specimen 2CMH18 (Lynn), was controlled by the buckling capacity. Similar to Specimen 1 tested in the current study, the failure of 2CMH18 was characterized by sudden, simultaneous loss of both axial and lateral load carrying capacity. Specimen 2CHD12 (Sezen) also experienced simultaneous axial and lateral load failure, but buckling was not established as the controlling failure mode. As such, the simultaneous axial and

lateral failure behavior for these three specimens cannot conclusively be attributed to the controlling failure mode of the longitudinal reinforcement without additional experimental evidence.

Inspection of the relationship between the applied axial load and the gross axial capacity of the longitudinal reinforcement for the specimens exhibiting simultaneous failure behavior reveals that each of these specimens had an axial load very close to or greater than the gross axial capacity of the bars $A_s f_y$. All remaining specimens in the database were subjected to axial loads much less than $A_s f_y$. Figure 3.26 presents the ratios of axial load P to gross axial capacity $A_s f_y$, and plastic capacity $P_{s\text{-}plastic}$ to buckling capacity $P_{s\text{-}buckle}$ for all columns listed in Table 3.9. Further study into the relationship between P and $A_s f_y$ is warranted to establish the validity of these observations.

Table 3.9: Axial capacity of the longitudinal bars for tests by Matchulat, Lynn, and Sezen

Specimen	Axial Load, P (kips)	Gross Axial Capacity, $A_s f_y$ (kips)	Plastic Capacity, $P_{s\text{-}plastic}$ (kips)	Elwood Buckling Capacity, $P_{s\text{-}buckle}$ (kips)
Matchulat (2008)				
1[a,b]	500	512	150	61
2	340	512	127	61
Lynn (2001)				
3CLH18	120	488	59	99
2CLH18	120	303	33	38
3SLH18	120	488	59	99
2SLH18	120	303	27	38
2CMH18[a,b]	340	303	79	38
3CMH18	340	488	88	99
3CMD12	340	488	88	222
3SMD12	340	488	88	222
Sezen (2000)				
2CLD12	150	512	41	137
2CHD12[b]	600	512	92	137
2CVD12	Variable	512	61	137
2CLD12M	150	512	41	137

a. Controlled by buckling capacity
b. Simultaneous axial and lateral load failure

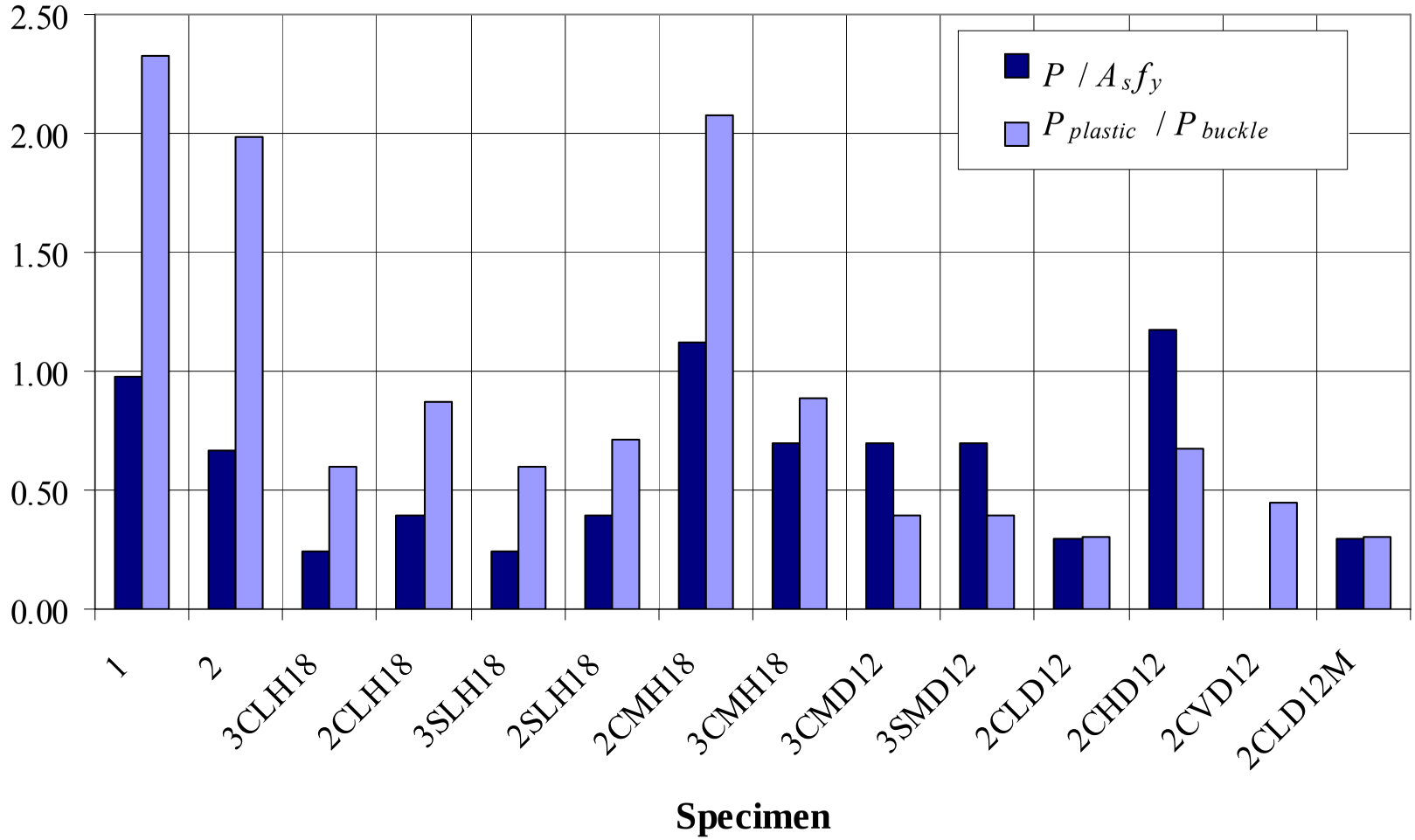

Figure 3.26: Ratios of axial load to gross axial capacity and plastic capacity to buckling capacity

CHAPTER 4: SUMMARY AND CONCLUSIONS

4.1 Summary

The objective of this study was to investigate the effect of axial load on the behavior of two full-scale reinforced concrete columns subjected to cyclic lateral loading. The two specimens had nominally identical material properties and reinforcement details. Transverse reinforcement was widely spaced to simulate the detailing found in columns most vulnerable to collapse. The specimens were fabricated in the Structural Testing Laboratory at the University of Kansas and tested at the NEES-MAST facility at the University of Minnesota. Construction materials for the specimens included No. 3 ASTM A615 and No. 9 ASTM A706 reinforcing steel, and normal-weight aggregate concrete with a target compressive strength of 3000 psi. The primary test variable was the magnitude of the applied axial load, which was maintained constant at 500 kips for the first specimen, and 340 kips for the second specimen.

The behavior of the specimens was monitored using an array of load, displacement, and strain transducers. A detailed description of both the damage progression in the specimens and their modes of failure is presented in Chapter 3. Specimen 1, which was subjected to the higher axial load, experienced simultaneous shear and axial failure at the negative peak of the first lateral displacement cycle to a drift ratio of 1.00%. Specimen 2 experienced failure at the positive peak of the first lateral displacement cycle to a drift ratio of 1.25%. Theoretical moment-curvature responses, deflection components, shear strength, drift capacity, and axial capacity of

the longitudinal reinforcement were calculated and compared with measured values. These data indicate that shear failure occurred very near yielding of the longitudinal reinforcement for both specimens. Loss in axial load carrying capacity in both specimens was precipitated by shear failure. The behavior of the two specimens after the first axial failure event was markedly different, with the specimen subjected to the higher axial load sustaining significantly greater damage.

A substantial reduction in lateral stiffness was observed after shear failure. Although there was a sizeable amount of damage associated with each axial failure event, the columns still maintained some residual axial capacity. The remaining axial capacity after each failure event appeared to be significantly affected by the axial load on the column, with the specimen subjected to the lower axial load having smaller reductions in axial capacity after each failure event.

4.2 Conclusions

Test results indicate that column performance both before and following initial axial failure was significantly impacted by the magnitude of the applied axial load. The following conclusions are based on observations from the two column tests:

1. The failure behavior of both specimens was very brittle in nature. Higher axial load, however, resulted in a significantly more brittle shear failure.

2. As expected from theory and previous research, axial load was directly proportional to the lateral strength and stiffness of the columns, and inversely proportional to drift capacity at axial failure.
3. Axial load carrying capacity of the first specimen was reduced by 63% following initial axial failure, while the second specimen only experienced a 6.5% reduction in axial capacity. Thus, a higher applied axial load corresponded to a more rapid degradation of axial strength.
4. Lateral load resistance of the first specimen was reduced to effectively zero following initial axial failure, while the second specimen only experienced a 55% reduction in lateral resistance. Thus, a higher applied axial load corresponded to a more rapid degradation of lateral strength.
5. The second specimen was able to carry the reduced axial load for a greater number of cycles beyond initial axial failure than the first specimen. Thus, a higher axial load resulted in a lower residual drift capacity beyond initial axial failure.
6. Neither specimen experienced significant yielding in flexure prior to axial failure. The first specimen, however, appeared to have been very close to or right at the yield point when axial failure occurred. This observation was confirmed by the calculated and measured moment-curvature responses, as well as deflection, bar strain, and shear strength data recorded during the tests.

7. The measured drift values at initial axial failure for both specimens correlated well with calculated values using the Elwood-Moehle axial failure model. The calculated drift ratios at axial failure for the reduced axial load values did not match those observed during the tests.
8. Both visual observations and measured load data indicate that the first specimen experienced axial failure as a result of longitudinal bar buckling. The second specimen, however, experienced axial failure due to the plastic capacity of the longitudinal bars under combined bending and axial load. These results are consistent with the longitudinal reinforcement axial capacities calculated using the bar buckling model presented by Elwood. Specimen behavior seems to indicate that simultaneous shear and axial failure, with a drastic reduction in axial capacity and lateral stiffness, are to be expected when the applied axial load is approximately equal to, or exceeds the gross axial capacity of the longitudinal reinforcement $A_s f_y$.

REFERENCES

ACI Committee 318. (2008). *Building Code Requirements for Structural Concrete and Commentary*. American Concrete Institute, Farmington Hills, MI, 467 pp.

ASTM C 39/C 39M – 05. (2005). "Standard Test Method for Compressive Strength of Cylindrical Concrete Specimens". ASTM International, West Conshohocken, PA, 7 pp.

ASTM C 78 – 08. (2008). "Standard Test Method for Flexural Strength of Concrete (Using Simple Beam with Third-Point Loading)". ASTM International, West Conshohocken, PA, 4 pp.

ASTM C 469 – 02. (2002). "Standard Test Method for Static Modulus of Elasticity and Poisson's Ratio of Concrete in Compression". ASTM International, West Conshohocken, PA, 5 pp.

Elwood, Kenneth J. and Jack P. Meohle. (2003). "Shake Table Tests and Analytical Studies on the Gravity Load Collapse of Reinforced Concrete Frames". *PEER Report 2003/01*, Pacific Earthquake Engineering Research Center, University of California, Berkeley, 346 pp.

Elwood, Kenneth J. and Jack P. Moehle. (2005). "Axial Capacity Model for Shear-Damaged Columns". *ACI Structural Journal*. Vol. 102, No. 4, July-Aug., pp. 578-587.

Elwood, Kenneth J. and Jack P. Moehle. (2004). "Evaluation of Existing Reinforced Concrete Columns". *13th World Conference on Earthquake Engineering*. Vancouver, BC, Canada, August 1-6, No. 579.

Elwood, Kenneth J., et al. (2007). "Update to ASCE/SEI 41 Concrete Provisions". *Earthquake Spectra*. Vol. 23, No. 3, Aug., pp. 493-523.

Hognestad, E. (1951). "A Study of Combined Bending and Axial Load in Reinforced Concrete Members". *Bulletin 399*. University of Illinois Engineering Experiment Station, Urbana, IL, 128 pp.

Lynn, Abraham C. (2001). "Seismic Evaluation of Existing Reinforced Concrete Building Columns". *PhD Dissertation*, University of California, Berkeley.

Lynn, Abraham C. et al. (1996). "Seismic Evaluation of Existing Reinforced Concrete Building Columns". *Earthquake Spectra*. Vol. 12, No. 4, Nov., pp. 715-739.

Matamoros, Adolfo B., Lisa Matchulat, and Charles Woods. (2008). "Axial Load Failure of Shear Critical Columns Subjected to High Levels of Axial Load". *14th World Conference on Earthquake Engineering*. Beijing, China, October 12-17, 8 pp.

Matamoros, Adolfo B. (2006). "Degrading Slope for Post-Peak Response of RC Columns Subjected to Load Reversals". Proceedings, *The Second NEES/E-Defense Workshop on Collapse Simulation of Reinforced Concrete Building Structures*, October 31-November 1, E-Defense, Kobe, Japan, pp. 267-280.

Matamoros, Adolfo B. (1999). "Study of Drift Limits for High-Strength Concrete Columns". *PhD Dissertation*, University of Illinois at Urbana-Champaign.

Nakamura, Takaya and Manabu Yoshimura. (2002). "Gravity Load Collapse of Reinforced Concrete Columns with Brittle Failure Modes". *Journal of Asian Architecture and Building Engineering*. Vol. 1, No. 1, March, pp. 21-27.

Saatcioglu, Murat and Guney Ozcebe. (1989). "Response of Reinforced Concrete Columns to Simulated Seismic Loading". *ACI Structural Journal*. Vol. 86, No. 1, Jan.-Feb., pp. 3-12.

Sezen, Halil. (2000). "Seismic Behavior and Modeling of Reinforced Concrete Building Columns". *PhD Dissertation*, University of California, Berkeley.

Sezen, Halil and Jack P. Moehle. (2006). "Seismic Tests of Concrete Columns with Light Transverse Reinforcement". *ACI Structural Journal*. Vol. 103, No. 6, Nov.-Dec., pp. 842-849.

University of Minnesota. (2008). Multi-axial Subassembly Testing Laboratory. http://nees.umn.edu.